



Universiteit
Leiden
The Netherlands

Role of near-surface environment in tuning electrochemical CO₂ reduction reaction and H₂ evolution reaction

Goyal, A.G.

Citation

Goyal, A. G. (2022, March 31). *Role of near-surface environment in tuning electrochemical CO₂ reduction reaction and H₂ evolution reaction*. Retrieved from <https://hdl.handle.net/1887/3281163>

Version: Publisher's Version

License: [Licence agreement concerning inclusion of doctoral thesis in the Institutional Repository of the University of Leiden](#)

Downloaded from: <https://hdl.handle.net/1887/3281163>

Note: To cite this publication please use the final published version (if applicable).

Role of Near-Surface Environment in Tuning Electrochemical CO₂ Reduction Reaction and H₂ Evolution Reaction

Proefschrift

ter verkrijging van
de graad van doctor aan de Universiteit Leiden,
op gezag van rector magnificus prof.dr.ir. H. bijl,
volgens besluit van het college voor promoties
te verdedigen op donderdag 31 maart 2022
klokke 15:00 uur

door

Akansha Goyal
geboren te Delhi, India
in 1994

Promotor:

Prof. Dr. Marc T. M. Koper

Co-promotor:

Associate Prof. Dr. Wilson A. Smith (Technische Universiteit Delft// University of Colorado, Boulder// NREL)

Promotiecommissie:

Prof. Dr. Huub de Groot

Dr. Rik Mom

Prof. Dr. Katharina Krischer (Technische Universität München)

Associate Prof. Dr. Yogesh Surendranath (Massachusetts Institute of Technology)

This Ph.D. thesis received financial support from Advanced Research Center for Chemical Building Blocks (ARC CBBC) consortium, co-financed by the Netherlands Organization for Scientific Research (NWO) and Shell Global Solutions International B.V.

ISBN 978-94-6423-638-5

But still try, for who knows what is possible.....

Michael Faraday

Table of Contents

CHAPTER 1	7
Introduction	
CHAPTER 2	35
Competition between CO ₂ reduction and hydrogen evolution on a gold electrode under well-defined mass transport conditions	
CHAPTER 3	55
The interrelated effect of cations and electrolyte pH on the hydrogen evolution reaction on gold electrodes in alkaline media	
CHAPTER 4	81
Understanding the role of mass transport in tuning the hydrogen evolution kinetics on gold in alkaline media	
CHAPTER 5	99
Effect of pore diameter and length on electrochemical CO ₂ reduction reaction at nanoporous gold catalysts	
APPENDIX A	119
Supporting Information to Chapter 2	
APPENDIX B	125
Supporting Information to Chapter 3	
APPENDIX C	135
Supporting Information to Chapter 4	
APPENDIX D	143
Supporting Information to Chapter 5	
SUMMARY	152
SAMENVATTING	154
LIST OF PUBLICATIONS	156
ACKNOWLEDGEMENTS	157
CURRICULUM VITAE	159



Chapter 1

Introduction



1.1. General Introduction

As the transition to renewable energy becomes inevitable, solving its intermittency problem is crucial if we wish to achieve carbon neutrality. Considering the timeframe specified by most international climate agreements (including Kyoto Protocol and Paris climate agreement), this issue is especially pressing.¹⁻² This means that we need robust technologies that can store excess renewable electricity, thereby allowing us to deploy it on demand in energy lean periods.³ For instance, electric energy can be stored in a battery⁴ or it can be used to drive non-spontaneous chemical reactions that generate energy rich molecules such as fuels and energy carriers.⁵⁻⁹ The latter process is similar to rolling a stone uphill and increasing its potential energy. This potential energy can then be converted into kinetic energy at a later point by simply letting the stone fall. Analogously, energy can be stored via the electrochemical reduction/hydrogenation of molecules and extracted via their oxidation (either by direct combustion or electrochemically) when required. In principle, the rate and efficiency of such an electrochemical conversion depends on the kinetic barrier of the reaction, which can be surmounted by employing appropriate electrocatalysts.

Broadly, electrocatalysts can be divided into two sub-categories, homogeneous and heterogeneous. As the name suggests, homogeneous electrocatalysts facilitate redox mediation in the solution phase by first undergoing an electron transfer reaction (at the electrode) followed by the relevant redox reaction with the substrate molecule in the solution phase. In general, these catalysts are designed to mimic naturally occurring redox enzymes (such as hydrogenases and nitrogenases) as these biological catalysts are able to achieve very high conversion rates, near the thermodynamic equilibrium potential of their respective reactions.¹⁰⁻¹¹ Hence, similar to the enzymes, most synthetic homogeneous catalysts also feature metal centers (such as Fe and Ni).¹²⁻¹³ The latter are chemically tuned via suitable ligand design to achieve an optimal redox potential for the electron transfer reaction and the accompanying molecular rearrangement. However, the activity and the overall stability of these catalysts remains an issue, even in the cases where the structure of the synthetic analogues is nearly identical to that of the active sites of the enzyme.⁷⁻⁸

On the other hand, heterogeneous electrocatalysis concerns itself with electrochemical reactions happening at the electrochemical interface via the direct movement of electrons/charge through different phases.¹⁴ That is, the charge carrier is transferred between the solid electrode and the (liquid) electrolyte that contains the substrate molecules. Here, unlike homogeneous electrocatalysis, the electrode surface facilitates the molecular rearrangement that accompanies the charge transfer. Hence, the electrode surface is not just an inert supplier of electrons but participates actively in the reaction. Most well-known applications of electrocatalysis such as fuel cells, chlor-alkali electrolyzers and water electrolysis are all forms of heterogeneous electrocatalysis, where multi-step electron transfer reactions take place at an electrode surface. The rate of such reactions is

determined by the electrochemical potential gradient at the interface which is dependent on both the nature of the catalyst material and the identity of the electrolyte.¹⁴ Hence, the key to the optimization of any heterogeneous electrocatalytic process lies in understanding and tuning the electrode-electrolyte interface.^{5, 14-15}

Heterogeneous electrocatalysis will be the main topic of our discussion. With this chapter we will first introduce some concepts related to heterogeneous electrocatalysis, henceforth referred to as electrocatalysis. Afterwards we will present a more specific discussion on the role of the electrode-electrolyte interface in tuning two important electrocatalytic reactions, namely, CO₂ reduction reaction (CO₂RR) and hydrogen evolution reaction (HER). These reactions will form the crux of the rest of the thesis.

1.2. Outer-sphere vs inner-sphere electron transfer

Electron transfer reactions at the electrode surface can be further classified as either outer-sphere or inner-sphere events. In outer-sphere reactions, the electron transfer between the electrode surface and the reactant molecule occurs via tunneling through a solvent layer. It is assumed that in these electron transfer events the geometry of the reactant molecules remains unperturbed. The change of the charge of the reactant causes a reorganization of its solvation shell only.¹⁶ Marcus theory describes quite well the kinetics of an outer-sphere electron transfer reaction at a molecular level and according to this theory the rate of the reaction increases approximately exponentially with the increasing thermodynamic driving force (applied overpotential; $\eta = E - E_o$) for the reaction.¹⁷⁻¹⁸ The theory predicts that the maximum rate for the reaction will be obtained when the thermodynamic driving force approaches the reorganization energy of the solvation shell.¹⁷⁻¹⁸ Since, an outer sphere reaction assumes that there is no direct chemical interaction between the electrode and the electroactive species, the rate constant for such a reaction is expected to be independent of the electrode material. The theory for outer-sphere electron transfer reactions is well developed and can be derived in a more general way without consideration for any specific adsorption effects.

On the other hand, in an inner-sphere reaction, the electron transfer is accompanied by changes in the geometry of the reactant/intermediate molecules via direct chemical interaction between the electroactive species and the electrode surface.¹⁶ Hence, in an inner sphere electron transfer reaction, the rate constants are sensitive to both the identity as well as the surface structure of the catalysts.¹⁹⁻²⁰ And even though the molecular considerations made in the Marcus theory are only applicable to an outer-sphere electron transfer, it is often applied to model inner-sphere electron transfer events, as the molecular factors that control the kinetics of the latter events remain poorly understood.²¹

Another important phenomenological model that describes the kinetics of the electron transfer at a macroscopic level is the Butler-Volmer expression.^{16, 22-23} This empirical expression explains the observed exponential dependence of the reaction rate on the applied overpotential by assuming that the activation energy of the reaction is linearly dependent on

the applied overpotential ($\Delta G^\ddagger = \Delta G_0^\ddagger - \alpha F\eta$). For a single electron transfer, the final Butler-Volmer expression gives the overall current density (j) for an electron transfer reaction in terms of the contributions from the forward and the backward reaction (eqn.1):

$$j = j_o \left(e^{\left(\frac{\alpha F\eta}{RT}\right)} - e^{\left(\frac{-(1-\alpha)F\eta}{RT}\right)} \right) \quad (1)$$

where F , R , T represent the Faraday's constant, the ideal gas constant and the temperature, respectively. j_o is the standard exchange current density, which represents the intrinsic activation barrier for a given reaction, such that a larger j_o means that the charge transfer step has a smaller activation barrier. α is an empirical proportionality constant (called the transfer coefficient), which varies between 0 and 1 and in doing so, gives the symmetry of the energy barrier for the reaction in the forward and backward direction. In principle, in going from an outer sphere to an inner sphere electron transfer reaction the energy barrier becomes more asymmetric, thus resulting in the deviation from the assumed value of 0.5 for α .^{16, 24-25} Moreover, for $|\eta| \gg RT/F$ the Butler-Volmer expression reduces to the well-known Tafel equation: $\eta = a + b \cdot \log j$ where $b = 2.303RT/\alpha F$ gives the Tafel slope.^{16, 26} This way of plotting the current-overpotential relationship is called Tafel analysis and it is often used to determine the operative mechanism for a multi-electron transfer reaction. In principle, the Butler-Volmer expression can be used to fit both outer and inner sphere electron transfer reactions, where in the former case j_o will vary only with the concentration of the species in the bulk while in the latter case it should also depend on the catalyst material (among other things). However, similar to the Marcus theory, this model suffers from certain limitations which also stem from the lack of consideration for the near-surface environment at the electrode-electrolyte interface. One such limitation arises due to changes in the near-surface concentration of the electroactive species with respect to the bulk.^{16, 27} These concentration gradients can result in unreliable Tafel analysis as the applied overpotential is no longer a true measure of the activation energy of the reaction and it has additional contributions from mass transport effects. Moreover, electrostatic and chemical interactions at the electrode-electrolyte interface are also neglected within the Butler-Volmer model, both of which require further corrections.²⁸⁻²⁹ Hence, in order to completely describe the kinetics of electrocatalytic reactions, or more specifically inner-sphere electrocatalytic reactions, it is important to look more closely at the electrode-electrolyte interface.

1.3. Electrostatic and chemical effects of adsorption in electrocatalysis

The idea that the electric double layer structure affects the kinetics of electrocatalytic reactions was put forward already in the early 1930s by Frumkin.^{16, 28} In his work, Frumkin argued that in the absence of any specific ion adsorption, the reaction plane of a heterogeneous reaction will be the outer-Helmholtz plane of the electric double layer. Hence, the effective

electrode potential that will affect the kinetics of an electrocatalytic reaction is not the electrochemical potential E at the electrode surface but instead $E - \varphi_{O.H.P.}$, i.e. the potential in the outer-Helmholtz plane. Additionally, he also argued that while considering the rate of a reaction the concentration of the electroactive species in the outer-Helmholtz plane has to be considered, instead of its bulk concentration. However, the former responds to the changing potential gradient within the double layer. Accounting for these double layer effects is the so called Frumkin correction, that addresses some of the experimental anomalies that are not accounted for by the previously described models. For instance, the dependence of the heterogeneous rate constant on the identity and the concentration of the supporting electrolyte. However, in most cases, this is still not sufficient.³⁰ That is, for most electrocatalytic reactions the chemical effects of adsorption at the interface also need to be considered in addition to the electrostatic effects.²⁹⁻³⁰ Only then the true role of the electrode-electrolyte interface in tuning the kinetics of a reaction can be captured.

Specific adsorption at the interface has profound impact on the kinetics of an electrode reaction.^{29, 31} One of the effects is the change in the position of the reaction plane itself which changes from the outer-Helmholtz plane (O.H.P.) to the inner-Helmholtz plane (I.H.P.) in the event of specific ion adsorption of the electroactive species. Consequently, the effective potential that drives a reaction also changes from $E - \varphi_{O.H.P.}$ to $E - \varphi_{I.H.P.}$. Moreover, when an electroinactive species (i.e. supporting electrolyte) adsorbs at the interface instead of the reactive species, the potential gradient within the double layer is still impacted, even though the reaction plane itself does not shift. In this event the required Frumkin correction for the system changes. However, even more important than these electrostatic effects are the surface coverage effects at the electrode surface associated with surface-adsorbate interactions. These effects alter both the rate and the mechanism of an electrode reaction and establish a direct correlation between electrocatalysis and heterogeneous catalysis.³²

Adsorption in electrocatalysis proceeds via the discharge of an ionic species at the electrode surface to form a neutral species, which is bound to the surface via a direct chemical bond. This neutral species has a certain coverage (θ) at the electrode surface and its adsorption behaviour can generally be modelled by using modified versions of the well-known adsorption isotherms that are generally employed in heterogeneous catalysis (such as Langmuir, Frumkin and Temkin isotherms).¹⁶ These modifications essentially account for the fact that in electrocatalysis the surface coverage θ of an adsorbed species also depends on the applied electrode potential. Hence, in electrochemistry, an adsorption isotherm gives the relationship between the coverage of the adsorbed species, the activity of the species in the bulk of the electrolyte and the electrode potential, at a constant temperature. For a general electrochemical reaction involving adsorption: $X_{sol}^+ + e^- + M \overset{K}{\leftrightarrow} X - M$, if we assume a Langmuir type adsorption (no lateral interactions and no surface heterogeneity), we can write (eqn. 2):

$$\frac{\theta}{1-\theta} = \frac{\Gamma_X}{\Gamma_{max}-\Gamma_X} = K_{ads} [X_{sol}^+] e^{\left(\frac{-\Delta G_{ads}^o(E_o)}{RT}\right)} e^{\left(\frac{-F(E-E_o)}{RT}\right)} \approx K'_{ads} [X_{sol}^+] e^{\left(\frac{-F(E-E_o)}{RT}\right)} \quad (2)$$

where Γ_X is the surface concentration of species X (in mol cm⁻²), Γ_{max} is the maximum (saturation) surface concentration, K_{ads} is the equilibrium constant of adsorption, $[X_{sol}^+]$ is the bulk concentration of X and $\Delta G_{ads}^o(E_o)$ is the standard Gibbs energy of adsorption at a fixed potential E_o (generally $E_o = 0$ against an arbitrary reference electrode) and K'_{ads} is the apparent equilibrium constant of adsorption $\left(K'_{ads} = K_{ads} e^{\left(\frac{-\Delta G_{ads}^o(E_o)}{RT}\right)}\right)$.

The $\Delta G_{ads}^o(E_o)$ term in eqn. 2 expresses the ability of a given catalyst material to adsorb species X and it is generally used to compare the activity of different materials for a given reaction involving the same reaction intermediate.³³⁻³⁴ This follows directly from Brønsted-Evans-Polyani relationship which states that the kinetics of a reaction involving adsorption/desorption i.e. its activation energy (ΔG^\ddagger) is linearly related to the thermodynamics of adsorption/desorption at the catalyst surface i.e. the standard Gibbs free energy of adsorption (ΔG_{ads}^o).³⁵⁻³⁶ Hence, an increase in the adsorption energy results in a proportional decrease in the activation energy of the reaction. This in-turn implies that at a fixed overpotential, the rate constant of an electron transfer reaction involving adsorption will increase with increasing adsorption energy:

$$k_o \propto j_o \propto e^{\left(\frac{-\beta \Delta G_{ads}^o(E_o)}{RT}\right)} \quad (3)$$

In electrocatalysis, this is often represented by $\ln j_o$ vs ΔG_{ads}^o or $\ln j_o$ vs $\ln K'_{ads}$ plots where $\ln j_o$ represents the activation barrier for the reaction.^{33-34, 37-39} These plots generally take a curved shape otherwise known as the volcano relationship which signifies that there is an optimal adsorption energy for a reaction intermediate that results in optimal activity for that reaction. If the adsorption energy increases beyond this optimal value, it results in the over-stabilization of the adsorbed intermediate at the catalyst surface, thereby resulting in a situation in which the desorption step of the reaction becomes rate limiting. This observation harkens back to the well-known Sabatier principle of heterogeneous catalysis which states that optimal catalytic activity is achieved when the catalyst-reactant interaction is neither too weak nor too strong.⁴⁰ Essentially, this means that with increasing adsorption energy, as the activation barrier for the reaction decreases, there is a simultaneous increase in the surface coverage of the reactive intermediate at the electrode surface. This leads to the "blocking" of the active sites at the catalyst surface, thereby resulting in a volcano relationship between the activity and the adsorption energy. This can be modelled in the kinetic eqns. for the adsorption step by accounting for the

slower rate of adsorption at X covered sites of the catalyst surface (θ) compared to the pristine sites ($1 - \theta$).

We note here that another important implication of the surface-adsorbate interactions described above is the effective potential dependence of the heterogeneous rate constant itself.^{29, 41} It was first elucidated by Parsons by introducing an activity coefficient term for the surface bound transition state of the reaction (inspired by Eyring).²⁹ Parsons showed that this activity coefficient is related to the potential dependent surface coverage θ term. This in-turn results in a potential dependence of the heterogeneous rate constant and in doing so, shows a better agreement with the experimental data than the Frumkin modified Butler-Volmer expression.³⁰

The fundamental insights on how the surface-adsorbate interactions shape the electrode-electrolyte interface, as discussed above, have not only shaped the laws and theories of electrocatalysis but they have also assisted in understanding the kinetic behaviour of different electrochemical reactions, both actively and retroactively. Moreover, these insights have also led to the recognition of an important activity descriptor, namely, adsorption free energy of reaction intermediates, that has long acted as the central parameter for discerning and tailoring electrocatalytic behaviour. It has helped in understanding the observed catalytic trends (Volcano plots) for important electrochemical reactions such as HER and at the same time it has also assisted in the rational synthesis of new catalytic materials.^{37, 39, 42-43}

However, even though these insights have been crucial to the theoretical and practical knowledge of electrode reactions, gaps remain in our molecular level understanding of the near-surface reaction environment.⁴⁴⁻⁴⁷ This is also reflected by the fact that often times additional descriptors/parameters are required to fully capture the reaction kinetics across different electrode-electrolyte combinations, especially for more complex reactions. In the next sections we will discuss some of these descriptors/parameters, specifically for the case of CO₂RR and HER, and show that the kinetics of electrocatalytic reactions can be altered by a myriad of additional effects that go beyond the realm of adsorption.

1.4. Electrochemical CO₂ reduction reaction: an overview

Electrochemical reduction of CO₂ into value added products, such as CO, formate, methane, ethylene and alcohols, provides a unique opportunity to close the anthropogenic CO₂ cycle while solving the intermittency issue of renewable electricity.^{8, 48} This is because electrochemical reduction of CO₂ offers the possibility of storing renewable electricity as infrastructure friendly carbon-based fuels, that are easy to store and transport. One of the most straightforward strategies to do this is to carry out electrochemical CO₂ reduction reaction (CO₂RR) in the aqueous media, as water can act as a continuous source of protons for the reaction. However, at present, many challenges remain that need to be resolved in order to make this process economically viable. Most of these challenges arise due to issues related with low energy efficiency and poor product selectivity of CO₂RR, both of which are partially related to the fact that a complex reaction network has

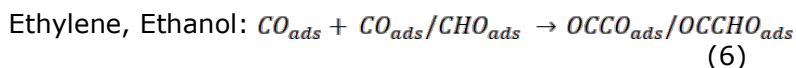
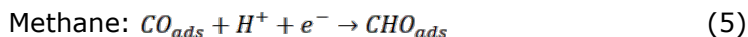
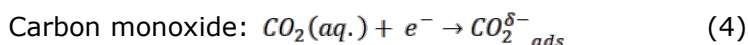
to be navigated in order to achieve a desired CO₂RR product, especially in the aqueous media. This reaction inherently has a bad selectivity as it often leads to concurrent C1, C2 and in some cases even C3 products, due to the comparable equilibrium potentials of the different reaction pathways.⁴⁹⁻⁵⁰ Moreover, the low energy efficiency of this process also stems from the fact that in aqueous electrolytes CO₂RR is inevitably accompanied by a concomitant hydrogen evolution reaction (HER) which is kinetically more facile than the multi-electron reduction of CO₂.⁵¹⁻⁵² HER can also be detrimental towards certain CO₂RR products as it can influence the electrolyte composition at the electrode-electrolyte interface. More specifically, by tuning the proton availability that affects the reaction pathways of CO₂RR.⁵² Hence, significant efforts have been put towards understanding the reaction mechanism of CO₂RR on the surface of different catalysts, so that key reaction intermediates for the different reaction products can be identified, and novel catalysts with optimal binding energies can be synthesized. In this respect, Hori and coworkers did some of the most seminal work in the late 1980s.⁵³⁻⁵⁷ They identified different classes of metallic catalysts for obtaining different CO₂RR products, based on how the electronic properties of the metals influence the species binding energies. This prompted a lot of follow-up research,^{50, 58-60} both practical and theoretical, towards the development of optimized catalytic materials by following the broad template outlined by Hori and coworkers. However, CO₂RR activities thus obtained have not shown much improvement. One reason for this is the existence of linear scaling relationships for the binding energy of different reaction intermediates associated with different CO₂RR reaction pathways.^{52, 61} Consequently, any changes in the electronic properties of the catalysts lead to simultaneous modification of the binding energies for different possible reaction pathways. Thus, making it difficult to obtain optimal selectivity towards one desired product. Moreover, while a lot of focus has been put on the optimization of CO₂RR on a given catalyst surface, studies on understanding and selectively suppressing the competing HER reaction under the conditions of CO₂RR have been very limited.⁶²⁻⁶⁵ This has contributed to the low energy efficiency and Faradaic selectivity for CO₂RR on the surface of most new catalysts that have been synthesized by solely taking the adsorption energies of CO₂RR intermediates into account.

Recently, it has been recognized that in addition to the catalyst material, the electrolytes employed for CO₂RR also have a profound impact on the activity/selectivity of this reaction.⁶⁴⁻⁶⁹ This is because the electrolyte identity can tune the near-surface reaction environment both by altering the structure/composition of the electric double layer and by impacting the local dynamic equilibria of CO₂ (aq.) and other reacting species (HCO₃⁻, H₃O⁺ and H₂O) in the electrolyte. Thus, going beyond the adsorption-based activity descriptors and understanding the role of electrolyte properties (such as cation identity, anion identity, local electrolyte pH and solvent identity) in tuning CO₂RR can be a viable strategy for boosting the energy efficiency as well as the product selectivity of this reaction.⁷⁰ In the next section, we will

discuss the possibilities offered by one such electrolyte parameter, namely, electrolyte pH, in tuning the CO₂RR activity.

1.4.1. pH effect on CO₂RR

It is well known that electrolyte pH has a profound impact on the kinetics of different CO₂RR pathways.^{64, 68-69, 71-72} Depending on the rate determining step (RDS) for a certain CO₂RR product i.e. whether it involves a proton coupled electron transfer (PCET) or simply an electron transfer (ET), it can either be (bulk) pH dependent or independent. Thus, if we consider the most widely accepted RDS for different CO₂RR products:



The reaction in eqn. 5 is an example of a reaction that is dependent on the bulk pH, whereas the reactions in eqns. 4 and 6 are independent of electrolyte pH. That is, the Butler-Volmer eqn. for these reactions will either include the term for bulk proton concentration or not. This can be exploited to tune the selectivity towards certain products by changing the bulk pH or the buffer strength of the electrolyte. In fact, Mul and coworkers reported that by optimizing the electrolyte pH they could achieve ethylene formation with high selectivity (up to 44%) and suppress methane formation (around 2%) on rough Cu electrodes.⁷³ Moreover, this strategy has also been employed with gas diffusion electrode set-ups to carry out CO₂RR in alkaline electrolyzers, where very high selectivity for ethylene (up to 69%) could be obtained.⁷⁴⁻⁷⁷

However, beyond these bulk pH effects, the local changes in the electrolyte pH can also affect CO₂RR selectivity by tuning the concentration of different reactive species near the electrode-electrolyte interface.^{67-68, 78} During CO₂RR in the aqueous media, the local pH becomes more alkaline than the bulk due to the constant generation of OH⁻ ions near the surface during CO₂RR (for example: $CO_2 + 2e^- + H_2O \rightarrow CO + 2OH^-$) and the competing HER ($H_2O + 2e^- \rightarrow H_2 + 2OH^-$) reaction. These changes in the local pH can directly impact the kinetics of the reactions that are implicitly dependent on the electrolyte pH (as described above). In addition to these effects, local pH changes can also impact the reaction kinetics by influencing the local concentration gradients for the different reactive species at the electrode surface. It follows that any changes in the local electrolyte pH trigger corresponding changes in the homogeneous equilibria between CO₂ (aq.), HCO₃⁻ and CO₃²⁻ species that are present in the electrolyte:





which results in certain concentration gradients for these species that can have a huge impact on the partial current densities of different CO₂RR products as well as H₂ formation, the side product due to HER. In principle, the homogeneous consumption of CO₂ (eqn. 7), as triggered by the increasing local pH at the surface can result in the suppression of CO₂RR due to increasing mass transport limitations for the reaction. Hence, changes in the buffering capacity of the electrolyte via bicarbonate concentration changes, CO₂ partial pressure changes as well as by the introduction of other buffering ions, can all contribute to the enhancement/suppression of CO₂RR by changing the local CO₂ (aq.) concentration.^{63, 79} Moreover, mass transport conditions can also be tuned either by changing convection control or by tuning the morphology of the catalysts than can either introduce or alleviate concentration gradients at the electrode surface.⁸⁰⁻⁸²

Notably, these changes in the local concentration gradients can also impact the kinetics of competing HER reaction, either due to the changes in concentration of the proton donor species at the electrode surface (such as HCO₃⁻) or due to explicit pH effects on the kinetics of HER (discussed in detail in the following sections). Needless to say, these changes in the HER activity can in-turn influence the Faradaic selectivity of CO₂RR.

However, even though the role of local pH changes in tuning the competition between HER and CO₂RR is being increasingly recognized, the studies that have been conducted to investigate these effects have been inconclusive thus far. One of the strategies that has been employed to investigate the role of local pH effects in tuning CO₂RR is the use of nanoporous catalysts. Introducing nanoporous structuring at the catalyst surface results in the generation of additional diffusional gradients and these gradients can be tuned by controlling pore diameter and pore length. In Table 1 we show a comparison of some of these studies on monometallic nanoporous catalysts, specifically for the case of CO₂RR towards CO formation. We see that even under relatively similar experimental conditions drastically different Faradaic selectivities for CO formation are achieved.⁸¹⁻⁸⁹ Hence, it appears that in order to understand the role of local pH gradients in tuning CO₂RR selectivity, first there is a need to study these effects under well-defined conditions where the local concentration gradients can be tuned systematically. Additionally, care has to be taken in comparing catalytic activities for similar catalysts when different electrolyte parameters are used, as changes in the electrolyte identity are directly reflected in the bulk as well as the local pH at the interface.^{73, 90} Hence, similar catalyst morphologies studied under different electrolyte conditions can also result in varying CO₂RR selectivities.

All the studies shown in Table 1 were performed by conducting long-term bulk electrolysis measurements coupled with a gas chromatography (GC) set-up. In such measurements, depending on the sampling time, cell geometry and electrolyte flow conditions, variable concentration gradients can be generated even with similar catalyst morphologies, thus resulting in

varying Faradaic selectivities. It is therefore important to study these effects with online techniques so that the interplay between the heterogeneous consumption of reactants/ production of hydroxyl ions and the corresponding changes in the homogeneous equilibria can be tracked in real time without any convolutions due to time-based concentration polarization effects.

Table 1 An overview of CO Faradaic efficiency during CO₂RR that have been reported in the literature on different monometallic porous catalysts (prepared with different techniques). Some of the important reaction parameters, such as pore diameter, bicarbonate concentration and the applied potential where the Faradaic efficiency is measured are also listed.

Group/Year	Catalyst-Substrate	Pore diameter	Electrolyte (M)	Potential (V vs RHE)	Faradaic efficiency (%) for CO
Lu et al. 2014 ⁸³	Ag (free standing)	Few hundred nm	0.5 M KHCO ₃	< - 0.5	92
Sen et al. 2014 ⁸⁵	Cu-Cu polished	15-72 μm	0.1 M KHCO ₃	- 0.4	27
Surendranath et al. 2015 ⁸²	Au-Au coated glass slide	200 nm	0.1 M KHCO ₃	- 0.4	75
Surendranath et al. 2016 ⁸¹	Ag-Au coated glass slide	200 nm	0.1 M KHCO ₃	- 0.6	80
Zhang et al. 2016 ⁸⁴	Ag-Ag foil	30-50 nm	0.5 M KHCO ₃	- 0.4	82
Wang et al. 2017 ⁸⁹	Cu-Cu foil	120- 300 nm	0.1 M KHCO ₃	- 0.8	55
Cheng et al. 2017 ⁸⁸	Au-Ag foil	Few hundred nm to few μm	0.1 M KHCO ₃	- 0.39	90.5
Chen et al. 2018 ⁸⁶	Au-Cu wire	250-500 nm	0.1 M NaHCO ₃	- 0.6	95.9
Luo et al. 2019 ⁸⁷	Zn-Cu mesh	30-80 μm	0.1 M KHCO ₃	- 0.95	95

In order to unambiguously elucidate the role of local pH effects in tuning CO₂RR it is important to separately study the role of mass transport conditions, electrolyte effects and catalyst morphology effects, so that general guiding principles can be derived for the selective optimization of CO₂RR.

Moreover, it is also important to understand the activity trends for HER under CO₂RR reaction conditions. So that this parasitic side reaction can be selectively suppressed and higher CO₂RR efficiencies can be obtained. In

the current literature, while a lot is understood about HER in acidic media, there are many ambiguities regarding the activity trends for HER under CO₂RR relevant near-neutral/alkaline reaction conditions. Hence, understanding HER trends is not only important due to its relevance for hydrogen generation/storage but also for other renewable technologies (such as CO₂RR), where it can act as a parasitic side reaction. And given that near-surface environment also plays an important role in tuning HER, in the next sections we will shift the focus to this reaction.

1.5. Electrochemical hydrogen evolution reaction: an overview

Hydrogen evolution reaction (HER) is perhaps the most well studied reaction in electrocatalysis. In fact, water splitting reaction to form hydrogen and oxygen is the earliest known experiment involving the chemical conversion of electricity.³² Many of the theories in electrocatalysis, some of which have been touched upon in the previous sections, were either developed to explain the empirically observed trends for HER or HER was used as a test reaction to develop more advanced theories of electrocatalysis. Additionally, this two-electron transfer reaction is also an important piece in the energy transition puzzle,⁹ as green hydrogen generated by water electrolysis is vital for achieving a carbon-neutral energy system and establishing the so-called hydrogen economy – a vision Bockris put forward already in the early 1970s.⁹¹

In this respect, most of the early studies on HER focused on understanding the mechanism and the activity trends for this reaction in acidic media.^{37-39, 92-94} This resulted in the identification of Pt as the best catalyst and of the adsorption free energy of hydrogen as the key descriptor for HER activity. Ultimately, this led to the commercialization of proton exchange membrane (PEM) electrolyzers, which employ Pt based catalysts for the cathodic half reaction (i.e. HER) of water splitting.

However, the activity trends for HER in alkaline media differ significantly from the trends obtained in the acidic media and catalysts such as Ir and Ni show superior activity under alkaline conditions, even though they bind hydrogen less optimally than Pt.⁹⁵⁻⁹⁷ In practice, this is what makes alkaline water electrolyzers more cost effective than PEM electrolyzers as they can be operated with cheaper Ni-based catalysts. However, the energy efficiency of alkaline electrolyzers remains inferior to PEM electrolyzers, since the HER activity always decreases in going from acidic environment to alkaline environment, regardless of the catalyst employed.⁹⁸ This has led to significant research efforts in the recent years, towards understanding the activity descriptors that govern the HER kinetics in alkaline media, with the goal of optimizing this reaction under alkaline conditions.

In-fact it is widely recognized now that the hydrogen binding energy (HBE) at the catalyst surface is an incomplete descriptor for HER, especially under alkaline conditions. HBE cannot explain many of the experimentally observed trends for HER, including the (non-Nernstian) pH dependence of the reaction^{44, 99-100} as well as the activity trends on different catalytic materials under alkaline conditions.^{47, 101-102} This in-turn points to a fundamental change of the nature of HER when going from acidic media to

alkaline media. This is also shown in Table 2, where we see that in acidic media, a hydronium ion (H_3O^+) undergoes discharge and forms an adsorbed hydrogen atom at the electrode surface. Instead, a neutral water molecule has to dissociate at the electrode surface in alkaline media. This essentially results in an additional barrier for the reaction in alkaline media, which is reflected by the fact that under alkaline conditions the first ET (Volmer step; see Table 2) is invariably the rate RDS, regardless of the employed catalyst. Consequently, the reaction rate of HER in alkaline media is influenced by additional parameters that can tune the interaction of the reactants (H_2O_{ads}) and the products (OH_{ads} , OH^-) of the RDS at the metal-electrolyte interface.

Table 2 Mechanism of HER under acidic conditions and under alkaline conditions where the rate determining step can either be Step I (Volmer step) or Step II (Heyrovsky/Tafel step).¹⁰³

HER Reaction	Step I	Step II
Acidic media: $2H_3O^+ + 2e^- \rightarrow H_2 + 2H_2O$	Volmer step: $H_3O^+ + e^- \rightarrow H_{ads} + H_2O$	Heyrovsky step: $H_{ads} + H_3O^+ + e^- \rightarrow H_2 + H_2O$ Or Tafel step: $H_{ads} + H_{ads} \rightarrow H_2$
Alkaline media: $2H_2O + 2e^- \rightarrow H_2 + 2OH^-$	Volmer step: $H_2O + e^- \rightarrow H_{ads} + OH^-$	Heyrovsky step: $H_{ads} + H_2O + e^- \rightarrow H_2 + OH^-$ Or Tafel step: $H_{ads} + H_{ads} \rightarrow H_2$

In the recent years, various important interfacial parameters have been identified that have been shown to influence the rate of HER in alkaline media, such as, the cation identity in the electrolyte, oxophilicity of the reactive sites and the interfacial electric field at the surface.^{47, 101, 104-106} Among these, interfacial electric field is an especially important parameter as it can affect both the structure and the composition of the electric double layer and hence, influence the near-surface reaction environment for HER in multiple ways. In the next section, we will discuss some of these ways in which the electric field effects impact the HER kinetics in alkaline media.

1.5.1. Electric field effect on HER

At an electrode-electrolyte interface, the interfacial electric field is determined by the applied potential and the potential of zero charge of the electrode material i.e. $\Delta E = E - E_{pzc}$.¹⁶ The potential of zero charge (pzc) represents the potential at which there is net zero surface charge density at the electrode surface ($E_{pzc} = E_{\sigma=0}$).¹⁰⁷ Hence, at potentials more negative than the pzc , the net interfacial electric field at the surface is negative and cations are expected to have preferential electrostatic interactions at the interface. On the other hand, at potentials more positive than the pzc , the net electric field is positive and the anions preferentially interact at the surface. We note that in reality, on most electrode surfaces, the net surface charge density is not zero at the pzc as there is always some degree of specific adsorption irrespective of the employed supporting electrolyte.¹⁰⁸⁻¹¹⁰ This results in a net charge at the surface even at the pzc , due to the

chemical bonds formed between the specifically adsorbed ions and the electrode surface. Hence, a distinction has to be made between the potential of zero free charge (*pzfc*) which represents the *pzc* in the absence of any specific adsorption and the potential of zero total charge (*pztc*) which represents the potential where the net charge at the surface is zero both due to electrostatic interactions and chemical interactions.¹⁰⁷ And, while the *pzfc* is only dependent on the electrode material (more specifically, the work function ϕ of the electrode), the *pztc* is dependent on both the electrode material and the electrolyte identity.¹¹¹ Consequently, at the same applied potential, varying interfacial electric field strength can be obtained depending on the nature of the electrode-electrolyte interfaces, which is in turn determined by the catalyst identity/structure as well as the composition of the bulk electrolyte.¹¹²⁻¹¹⁴

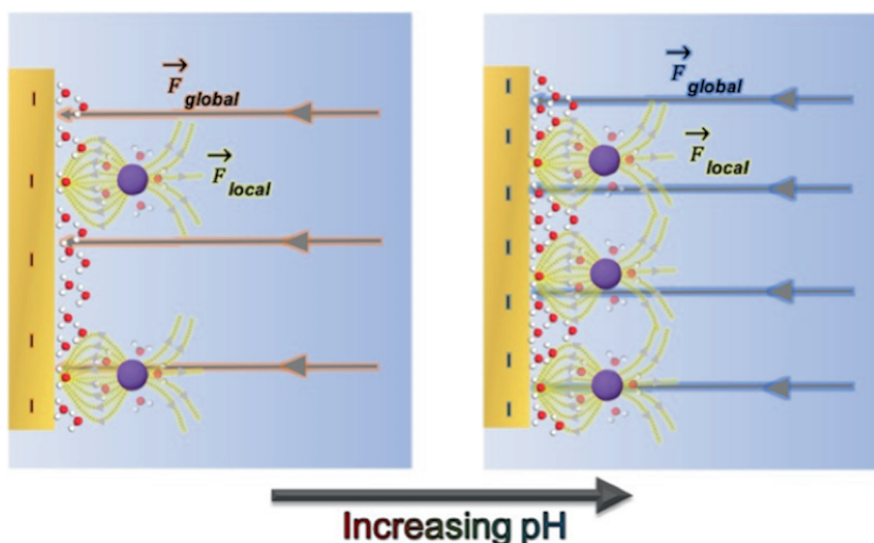


Figure 1 A schematic representation of the pH dependent global interfacial electric field at the electrode surface which affects the solvent (water) structure at the interface as well as the local composition of the double layer, such that an increasing global electric field strength results in a higher reorganization energy for the interfacial water network and a higher near surface cation concentration. Additionally, the cations near the interface also exert a local electric field aligned with the dipole of the reacting water molecule at the electrode surface.

This interfacial electric field can influence the rate of an electrocatalytic reaction in a number of ways. For instance, by influencing the solvent dynamics at the interface, by tuning the polarizability of the reaction intermediates and/or by tuning the composition of the electric double layer, which can in-turn influence the chemical/electrostatic interactions of the adsorbed intermediates in the reaction plane.¹⁵ In a recent study, our group showed that for Pt(111), the changes in the solvent dynamics with changing interfacial electric field tune the rate of HER in alkaline media.¹⁰⁴ We proposed that the interfacial water network has the highest mobility when the interfacial electric field is the weakest and this mobile water network can facilitate the transport of ions such as H_3O^+ , OH^- within the double layer,

thus facilitating HER. On the other hand, as the interfacial electric field becomes stronger (more negative), the water network at the surface becomes more rigid, thus, hindering the transport of ions near the interface. Moreover, based on the previous works by Feliu and coworkers, the interfacial electric field on Pt(111) is expected to become more negative (vs reversible hydrogen electrode) with increasing electrolyte pH.¹¹⁵ Hence, the loss in the HER activity on Pt(111) with increasing electrolyte pH can be reconciled with the changes in the interfacial water structure with changing interfacial electric field.

Additionally, the interfacial electric field is also directly intertwined with another important parameter for HER kinetics, namely the extent of cation adsorption at the electrode surface and/or the cation concentration in the O.H.P.^{15, 116-117} It has been shown previously that the HER activity in alkaline media is very sensitive to the identity of the alkali metal cations in the electrolyte.^{47, 106} Markovic and co-workers have shown that on Pt based catalysts, the HER activity increases in the order $\text{Cs}^+ < \text{K}^+ < \text{Na}^+ < \text{Li}^+$ which they correlate to the stronger interaction of the Li^+ ions with the dissociating water molecule in the rate determining Volmer step (see Table 2).^{101-102, 118} However, the surface coverage of the alkali metal cations at a given surface is in-turn dependent on the interfacial electric field strength. This is because a stronger interfacial electric field can stabilize the surface dipole generated by a specifically adsorbed cation, thus resulting in a larger cation coverage at the surface and/or a higher near-surface cation concentration in the O.H.P. Hence, in addition to the solvent dynamic effects, the interfacial electric field can also influence the HER kinetics by tuning the near-surface cation concentration at the interface. Moreover, it should be noted that in the above discussions, the interfacial electric field has been considered to be uniform everywhere within the reaction plane (parallel to the electrode surface). However, due to the presence of ions in the electric double layer, there will be an additional "local" electric field associated to these ions (as shown in Fig. 1).¹¹⁹ These local changes in the interfacial electric field can also influence the HER reaction rate as the electrostatic interactions between the adsorbed reaction intermediates and the cations can also tune the reaction energetics at the interface.

However, even though the effect of the interfacial electric field on the near-surface cation concentration has been studied to some degree in the literature, its role in tuning the HER activity remains elusive. Given that, these cation-associated field effects have been shown to influence the activity of other electrocatalytic reactions such as CO_2RR ,¹¹⁹⁻¹²⁰ it can be expected that these effects can also have a profound impact on the rate of HER.

1.6. Scope of the thesis

The scope of this thesis lies in understanding the role of near-surface environment in tuning electrocatalytic reactions by the means of interactions that go beyond the traditional adsorption-based activity descriptors. In the preceding sections we have outlined some of the shortcomings of such adsorption-based descriptors and the classical

theories that are generally used to simulate the kinetics of electrocatalytic reactions. Especially, when considering the activity trends for CO₂RR and HER, under practical reaction conditions. In the following chapters, we will present in-depth studies on some of these additional reaction parameters that can tune CO₂RR and HER and elucidate some of the molecular complexities that underlie these reactions.

In chapter 2, we will first discuss the development of an online rotating ring disk electrode (RRDE) set-up that allowed us to bypass the issues that were discussed in section 1.4.1.⁸⁰ Briefly, the RRDE technique allows for hydrodynamic convection control at the electrode surface which in-turn results in well-defined near-surface concentration gradients. Hence, by using the RRDE technique, the role of concentration (pH gradients) in controlling the CO₂RR activity can be studied under well-defined conditions. Moreover, the RRDE technique also gives the possibility to separate the contributions due to mass transport effects and intrinsic kinetics of the reaction, thus improving upon one of the limitations of the Butler-Volmer model (as discussed in section 1.2 and 1.3). Moreover, we restricted this study to the polycrystalline Au surface in order to simplify the system. That is, we avoid additional convolutions due to the internal competition between different CO₂RR pathways, as CO₂RR on Au electrodes yields only CO as the main product for this reaction. Thus, we focused our study on the role of local pH gradients in tuning the competition between CO₂RR and HER. Interestingly, we found that CO₂RR shows only a slight improvement with increasing mass transport (decreasing local pH), while the changes in the local pH at the Au surface mainly affected the kinetics of the competing HER. Essentially, we observe a significant improvement in HER activity with increasing local pH at the surface. To emphasize: an increase in the local pH with increasing mass transport rate leads to the suppression of CO₂RR Faradaic selectivity, even though the kinetics of CO formation is not significantly impacted by the changing local concentration gradients.

In chapter 3, we elucidate the pH dependence of the HER kinetics on Au electrodes further.¹²¹ In doing so, we shed light on the role of the pH dependent interfacial electric field in tuning HER activity. We show that with increasing strength of the interfacial electric field, the near-surface cation concentration also increases. This increase in the near-surface cation concentration in-turn results in the enhancement of HER, as cations near the surface can decrease the activation barrier for the reaction. This is because the cations can favorably interact with the transition state of the rate determining Volmer step ($*\text{H}^{\ominus}\text{--OH}^{\ominus}\text{--cat}^{\oplus}$). Interestingly, this cation assisted enhancement of HER kinetics saturates and even becomes inhibitive as the local cation concentration increases beyond a threshold concentration. This shows that while an initial increase in the cation concentration decreases the activation barrier for the reaction, at some point the metal-cation interactions start to inhibit the HER reaction, either due to double layer crowding or due to blocking effects. These results clearly show that the electrolyte pH and the near surface cation concentration are two interrelated parameters, that have a similar effect on the HER kinetics. Moreover, we confirm that the interfacial electric field is indeed an important

parameter in tuning the HER kinetics in alkaline media and it not only alters the structure (solvent dynamics) of the double layer but also the composition of the near-surface reaction environment. Hence, its role in tuning the near-surface reaction environment is even more convoluted than was previously hypothesized in the literature (as discussed in section 1.5.1). In chapter 4, we reconcile the results presented in Chapter 2 and Chapter 3 by further elucidating the role of local pH gradients in tuning the HER kinetics on Au electrodes. We point out that while the changes in the interfacial electric field with the changing bulk pH can tune the near-surface cation concentration (chapter 3), the local pH effects on HER kinetics, as observed in chapter 2 are different than these bulk pH effects. Instead, we demonstrate that the changes in the local pH with changing rotation (mass transport) rate tune the local cation concentration due to the need to satisfy local electro-(neutrality) conditions. Hence, even though the changes in the bulk pH and the local pH seem to influence the HER kinetics on Au electrodes in a similar fashion, there is a distinction in the underlying cause for these effects. The former effect is due to the changes in the local cation concentration with changing interfacial electric field, while the latter results from the need to satisfy local electro-(neutrality) which results in increasing local cation concentration with increasing local hydroxyl concentration.

Lastly, in chapter 5, we extend the understanding gained from the previous chapters to further elucidate the role of near-surface reaction environment in tuning CO₂RR and HER on nanoporous Au catalysts. We present a systematic study on the role pore parameters (pore diameter and pore length) in tuning the Faradaic selectivity for CO₂RR by employing differential electrochemical mass spectrometry (DEMS). The latter is a powerful online and *in situ* technique that allowed us to quantify the formed amounts of H₂ and CO and bypass the limitations that have resulted in convoluted trends in the previously reported literature on nanoporous catalysts (as discussed in section 1.4.1). We find that similar to the flat polycrystalline Au electrodes, the changes in the local pH gradients with changing pore parameters mainly affect the rate of the HER reaction. However, the changing pore parameters also tune the CO₂RR activity due to the changes in the number of active sites at the catalyst surface and due to the presence of additional Ohmic drop effects within the porous channels.

In summary, we show in this thesis that the near-surface reaction environment is a dynamic entity that can be tuned by varying the electrolyte parameters. Here, we discuss the role of the electrolyte pH, the cation identity and cation concentration. Furthermore, we demonstrate that mass transport conditions (via convection control or catalyst morphology) is an important tuning handle for controlling the near-surface reaction environment. With this thesis we reveal that the kinetics of different electrocatalytic reactions can be tuned by defining the near-surface environment through various means. In doing so, we venture beyond classical theories of electrocatalysis, that fail to consider the intertwined effects of bulk/local electrolyte composition and local electric field on inner sphere reactions.

References

1. Gür, T. M., Review of electrical energy storage technologies, materials and systems: challenges and prospects for large-scale grid storage. *Energy & Environmental Science* **2018**, *11* (10), 2696-2767.
2. Götz, M.; Lefebvre, J.; Mörs, F.; McDaniel Koch, A.; Graf, F.; Bajohr, S.; Reimert, R.; Kolb, T., Renewable Power-to-Gas: A technological and economic review. *Renewable Energy* **2016**, *85*, 1371-1390.
3. Akinyele, D. O.; Rayudu, R. K., Review of energy storage technologies for sustainable power networks. *Sustainable Energy Technologies and Assessments* **2014**, *8*, 74-91.
4. Schipper, F.; Erickson, E. M.; Erk, C.; Shin, J.-Y.; Chesneau, F. F.; Aurbach, D., Review—Recent Advances and Remaining Challenges for Lithium Ion Battery Cathodes. *Journal of The Electrochemical Society* **2016**, *164* (1), A6220-A6228.
5. Stamenkovic, V. R.; Strmcnik, D.; Lopes, P. P.; Markovic, N. M., Energy and fuels from electrochemical interfaces. *Nature Materials* **2017**, *16* (1), 57-69.
6. Akhade, S. A.; Singh, N.; Gutiérrez, O. Y.; Lopez-Ruiz, J.; Wang, H.; Holladay, J. D.; Liu, Y.; Karkamkar, A.; Weber, R. S.; Padmaperuma, A. B.; Lee, M.-S.; Whyatt, G. A.; Elliott, M.; Holladay, J. E.; Male, J. L.; Lercher, J. A.; Rousseau, R.; Glezakou, V.-A., Electrocatalytic Hydrogenation of Biomass-Derived Organics: A Review. *Chemical Reviews* **2020**, *120* (20), 11370-11419.
7. Qing, G.; Ghazfar, R.; Jackowski, S. T.; Habibzadeh, F.; Ashtiani, M. M.; Chen, C.-P.; Smith, M. R.; Hamann, T. W., Recent Advances and Challenges of Electrocatalytic N₂ Reduction to Ammonia. *Chemical Reviews* **2020**, *120* (12), 5437-5516.
8. Zhang, S.; Fan, Q.; Xia, R.; Meyer, T. J., CO₂ Reduction: From Homogeneous to Heterogeneous Electrocatalysis. *Accounts of Chemical Research* **2020**, *53* (1), 255-264.
9. Hydrogen to the rescue. *Nature Materials* **2018**, *17* (7), 565-565.
10. Schilter, D., Homogeneous catalysis: Synthetic models close in on enzymes. *Nature Reviews Chemistry* **2018**, *2* (1), 0147.
11. Brazzolotto, D.; Gennari, M.; Queyriaux, N.; Simmons, T. R.; Pécaut, J.; Demeshko, S.; Meyer, F.; Orio, M.; Artero, V.; Duboc, C., Nickel-centred proton reduction catalysis in a model of [NiFe] hydrogenase. *Nat Chem* **2016**, *8* (11), 1054-1060.
12. Tasker, S. Z.; Standley, E. A.; Jamison, T. F., Recent advances in homogeneous nickel catalysis. *Nature* **2014**, *509* (7500), 299-309.
13. Junge, K.; Schröder, K.; Beller, M., Homogeneous catalysis using iron complexes: recent developments in selective reductions. *Chemical Communications* **2011**, *47* (17), 4849-4859.
14. Boettcher, S. W.; Oener, S. Z.; Lonergan, M. C.; Surendranath, Y.; Ardo, S.; Brozek, C.; Kempler, P. A., Potentially Confusing: Potentials in Electrochemistry. *ACS Energy Letters* **2021**, *6* (1), 261-266.
15. Waagele, M. M.; Gunathunge, C. M.; Li, J.; Li, X., How cations affect the electric double layer and the rates and selectivity of electrocatalytic processes. *The Journal of Chemical Physics* **2019**, *151* (16), 160902.
16. Bard, A. J.; Faulkner, L. R., *Electrochemical methods : fundamentals and applications* Wiley: New York, **1980**.
17. Marcus, R. A., On the Theory of Oxidation-Reduction Reactions Involving Electron Transfer. I. *The Journal of Chemical Physics* **1956**, *24* (5), 966-978.
18. Marcus, R. A., Chemical and Electrochemical Electron-Transfer Theory. *Annual Review of Physical Chemistry* **1964**, *15* (1), 155-196.

19. Sawyer, D. T.; Chiericato, G.; Angelis, C. T.; Nanni, E. J.; Tsuchiya, T., Effects of media and electrode materials on the electrochemical reduction of dioxygen. *Analytical Chemistry* **1982**, *54* (11), 1720-1724.
20. Adžić, R. R.; Tripković, A. V.; O'Grady, W. E., Structural effects in electrocatalysis. *Nature* **1982**, *296* (5853), 137-138.
21. Boettcher, S. W.; Surendranath, Y., Heterogeneous electrocatalysis goes chemical. *Nature Catalysis* **2021**, *4* (1), 4-5.
22. Butler, J. A. V., Studies in heterogeneous equilibria. Part II.—The kinetic interpretation of the nernst theory of electromotive force. *Transactions of the Faraday Society* **1924**, *19* (March), 729-733.
23. Erdey-Grúz, T.; Volmer, M., Zur Theorie der Wasserstoff Überspannung. *Zeitschrift für Physikalische Chemie* **1930**, *150A* (1), 203-213.
24. Mayer, J. M.; Rhile, I. J., Thermodynamics and kinetics of proton-coupled electron transfer: stepwise vs. concerted pathways. *Biochimica et Biophysica Acta (BBA) - Bioenergetics* **2004**, *1655*, 51-58.
25. Guidelli, R.; Compton, R. G.; Feliu, J. M.; Gileadi, E.; Lipkowski, J.; Schmickler, W.; Trasatti, S., Defining the transfer coefficient in electrochemistry: An assessment (IUPAC Technical Report). *Pure and Applied Chemistry* **2014**, *86* (2), 245-258.
26. Tafel, J., Über die Polarisation bei kathodischer Wasserstoffentwicklung. *Zeitschrift für Physikalische Chemie* **1905**, *50U* (1), 641-712.
27. Khadke, P.; Tichter, T.; Boettcher, T.; Muench, F.; Ensinger, W.; Roth, C., A simple and effective method for the accurate extraction of kinetic parameters using differential Tafel plots. *Scientific reports* **2021**, *11* (1), 8974-8974.
28. Frumkin, A.; Gorodetzka, A., Kapillarelektische Erscheinungen an Amalgamen: I. Thalliumamalgame. *Zeitschrift für Physikalische Chemie* **1928**, *136U* (1), 451-472.
29. Parsons, R., The effect of specific adsorption on the rate of an electrode process. *Journal of Electroanalytical Chemistry and Interfacial Electrochemistry* **1969**, *21* (1), 35-43.
30. Timmer, B.; Sluyters-Rehbach, M.; Sluyters, J. H., Electrode kinetics and double layer structure. *Surface Science* **1969**, *18* (1), 44-61.
31. Habib, M. A.; Bockris, J. O. M., Specific Adsorption of Ions. Springer US: 1980; pp 135-219.
32. Duca, M.; Koper, M. T. M., Fundamental Aspects of Electrocatalysis 1). In *Surface and Interface Science*, **2020**; pp 773-890.
33. Parsons, R., The rate of electrolytic hydrogen evolution and the heat of adsorption of hydrogen. *Transactions of the Faraday Society* **1958**, *54* (0), 1053-1063.
34. Gerischer, H., Mechanismus der Elektrolytischen Wasserstoffabscheidung und Adsorptionsenergie von Atomarem Wasserstoff. *Bulletin des Sociétés Chimiques Belges* **1958**, *67* (7-8), 506-527.
35. Bronsted, J. N., Acid and Basic Catalysis. *Chemical Reviews* **1928**, *5* (3), 231-338.
36. Evans, M. G.; Polanyi, M., Inertia and driving force of chemical reactions. *Transactions of the Faraday Society* **1938**, *34* (0), 11-24.
37. Trasatti, S., Work function, electronegativity, and electrochemical behaviour of metals: III. Electrolytic hydrogen evolution in acid solutions. *Journal of Electroanalytical Chemistry and Interfacial Electrochemistry* **1972**, *39* (1), 163-184.

38. Trasatti, S., *Development of the Work Function Approach to the Underpotential Deposition of Metals. Application to the Hydrogen Evolution Reaction**. 1975; Vol. 98, p 75-94.
39. Nørskov, J. K.; Bligaard, T.; Logadottir, A.; Kitchin, J. R.; Chen, J. G.; Pandelov, S.; Stimming, U., Trends in the Exchange Current for Hydrogen Evolution. *Journal of The Electrochemical Society* **2005**, *152* (3), J23.
40. Sabatier, P., *La Catalyse en chimie organique, par Paul Sabatier*. C. Béranger: Paris; Liège, 1913.
41. Oldham, K. B., The potential-dependence of electrochemical rate constants. *Journal of Electroanalytical Chemistry and Interfacial Electrochemistry* **1968**, *16* (2), 125-130.
42. Zeradjanin, A. R.; Vimalanandan, A.; Polymeros, G.; Topalov, A. A.; Mayrhofer, K. J. J.; Rohwerder, M., Balanced work function as a driver for facile hydrogen evolution reaction – comprehension and experimental assessment of interfacial catalytic descriptor. *Physical Chemistry Chemical Physics* **2017**, *19* (26), 17019-17027.
43. Greeley, J.; Nørskov, J. K.; Kibler, L. A.; El-Aziz, A. M.; Kolb, D. M., Hydrogen Evolution Over Bimetallic Systems: Understanding the Trends. *ChemPhysChem* **2006**, *7* (5), 1032-1035.
44. Rebollar, L.; Intikhab, S.; Oliveira, N. J.; Yan, Y.; Xu, B.; McCrum, I. T.; Snyder, J. D.; Tang, M. H., "Beyond Adsorption" Descriptors in Hydrogen Electrocatalysis. *ACS Catalysis* **2020**, *10* (24), 14747-14762.
45. Ojha, K.; Arulmozhi, N.; Aranzales, D.; Koper, M. T. M., Double Layer at the Pt(111)-Aqueous Electrolyte Interface: Potential of Zero Charge and Anomalous Gouy-Chapman Screening. *Angewandte Chemie International Edition* **2020**, *59* (2), 711-715.
46. Koper, M. T. M., A basic solution. *Nature Chemistry* **2013**, *5*, 255.
47. Strmcnik, D.; Kodama, K.; van der Vliet, D.; Greeley, J.; Stamenkovic, V. R.; Marković, N. M., The role of non-covalent interactions in electrocatalytic fuel-cell reactions on platinum. *Nature Chemistry* **2009**, *1*, 466.
48. Mikkelsen, M.; Jørgensen, M.; Krebs, F. C., The teraton challenge. A review of fixation and transformation of carbon dioxide. *Energy & Environmental Science* **2010**, *3* (1), 43-81.
49. Nitopi, S.; Bertheussen, E.; Scott, S. B.; Liu, X.; Engstfeld, A. K.; Horch, S.; Seger, B.; Stephens, I. E. L.; Chan, K.; Hahn, C.; Nørskov, J. K.; Jaramillo, T. F.; Chorkendorff, I., Progress and Perspectives of Electrochemical CO₂ Reduction on Copper in Aqueous Electrolyte. *Chemical Reviews* **2019**, *119* (12), 7610-7672.
50. Hahn, C.; Hatsukade, T.; Kim, Y.-G.; Vailionis, A.; Baricuatro, J. H.; Higgins, D. C.; Nitopi, S. A.; Soriaga, M. P.; Jaramillo, T. F., Engineering Cu surfaces for the electrocatalytic conversion of CO₂: Controlling selectivity toward oxygenates and hydrocarbons. *Proceedings of the National Academy of Sciences* **2017**, *114* (23), 5918-5923.
51. Birdja, Y. Y.; Pérez-Gallent, E.; Figueiredo, M. C.; Göttle, A. J.; Calle-Vallejo, F.; Koper, M. T. M., Advances and challenges in understanding the electrocatalytic conversion of carbon dioxide to fuels. *Nature Energy* **2019**, *4* (9), 732-745.
52. Kortlever, R.; Shen, J.; Schouten, K. J. P.; Calle-Vallejo, F.; Koper, M. T. M., Catalysts and Reaction Pathways for the Electrochemical Reduction of Carbon Dioxide. *The Journal of Physical Chemistry Letters* **2015**, *6* (20), 4073-4082.
53. Hori, Y.; Kikuchi, K.; Suzuki, S., Production of CO and CH₄ in electrochemical reduction of CO₂ at metal electrodes in aqueous hydrogencarbonate solution. *Chemistry Letters* **1985**, *14*, 1695-1698.

54. Hori, Y.; Murata, A.; Takahashi, R., Formation of hydrocarbons in the electrochemical reduction of carbon dioxide at a copper electrode in aqueous solution. *Journal of the Chemical Society, Faraday Transactions 1: Physical Chemistry in Condensed Phases* **1989**, *85* (8), 2309-2326.
55. Hoshi, N.; Kato, M.; Hori, Y., Electrochemical reduction of CO₂ on single crystal electrodes of silver Ag(111), Ag(100) and Ag(110). *Journal of Electroanalytical Chemistry* **1997**, *440* (1), 283-286.
56. Hori, Y.; Murata, A.; Kikuchi, K.; Suzuki, S., Electrochemical reduction of carbon dioxides to carbon monoxide at a gold electrode in aqueous potassium hydrogen carbonate. *Journal of the Chemical Society, Chemical Communications* **1987**, (10), 728-729.
57. Hori, Y.; Takahashi, I.; Koga, O.; Hoshi, N., Electrochemical reduction of carbon dioxide at various series of copper single crystal electrodes. *Journal of Molecular Catalysis A: Chemical* **2003**, *199* (1), 39-47.
58. Clark, E. L.; Ringe, S.; Tang, M.; Walton, A.; Hahn, C.; Jaramillo, T. F.; Chan, K.; Bell, A. T., Influence of Atomic Surface Structure on the Activity of Ag for the Electrochemical Reduction of CO₂ to CO. *ACS Catalysis* **2019**, *9* (5), 4006-4014.
59. Cave, E. R.; Montoya, J. H.; Kuhl, K. P.; Abram, D. N.; Hatsukade, T.; Shi, C.; Hahn, C.; Norskov, J. K.; Jaramillo, T. F., Electrochemical CO₂ reduction on Au surfaces: mechanistic aspects regarding the formation of major and minor products. *Physical Chemistry Chemical Physics* **2017**, *19* (24), 15856-15863.
60. Seh, Z. W.; Kibsgaard, J.; Dickens, C. F.; Chorkendorff, I.; Nørskov, J. K.; Jaramillo, T. F., Combining theory and experiment in electrocatalysis: Insights into materials design. *Science* **2017**, *355* (6321).
61. Pérez-Ramírez, J.; López, N., Strategies to break linear scaling relationships. *Nature Catalysis* **2019**, *2*.
62. Cave, E. R.; Shi, C.; Kuhl, K. P.; Hatsukade, T.; Abram, D. N.; Hahn, C.; Chan, K.; Jaramillo, T. F., Trends in the Catalytic Activity of Hydrogen Evolution during CO₂ Electroreduction on Transition Metals. *ACS Catalysis* **2018**, Medium: ED; Size: p. 3035-3040.
63. Bondue, C. J.; Graf, M.; Goyal, A.; Koper, M. T. M., Suppression of Hydrogen Evolution in Acidic Electrolytes by Electrochemical CO₂ Reduction. *Journal of the American Chemical Society* **2021**, *143* (1), 279-285.
64. Wuttig, A.; Yaguchi, M.; Motobayashi, K.; Osawa, M.; Surendranath, Y., Inhibited proton transfer enhances Au-catalyzed CO₂-to-fuels selectivity. *Proceedings of the National Academy of Sciences* **2016**, *113* (32), E4585-E4593.
65. Wuttig, A.; Yoon, Y.; Ryu, J.; Surendranath, Y., Bicarbonate Is Not a General Acid in Au-Catalyzed CO₂ Electroreduction. *Journal of the American Chemical Society* **2017**, *139* (47), 17109-17113.
66. Dunwell, M.; Lu, Q.; Heyes, J. M.; Rosen, J.; Chen, J. G.; Yan, Y.; Jiao, F.; Xu, B., The Central Role of Bicarbonate in the Electrochemical Reduction of Carbon Dioxide on Gold. *Journal of the American Chemical Society* **2017**, *139* (10), 3774-3783.
67. Dunwell, M.; Yang, X.; Setzler, B. P.; Anibal, J.; Yan, Y.; Xu, B., Examination of Near-Electrode Concentration Gradients and Kinetic Impacts on the Electrochemical Reduction of CO₂ using Surface-Enhanced Infrared Spectroscopy. *ACS Catalysis* **2018**, 3999-4008.
68. Clark, E. L.; Bell, A. T., Direct Observation of the Local Reaction Environment during the Electrochemical Reduction of CO₂. *Journal of the American Chemical Society* **2018**, *140* (22), 7012-7020.

69. Resasco, J.; Lum, Y.; Clark, E.; Zeledon, J. Z.; Bell, A. T., Effects of Anion Identity and Concentration on Electrochemical Reduction of CO₂. *ChemElectroChem* **2018**, *5* (7), 1064-1072.
70. Moura de Salles Pupo, M.; Kortlever, R., Electrolyte Effects on the Electrochemical Reduction of CO₂. *ChemPhysChem* **2019**, *20* (22), 2926-2935.
71. Schouten, K. J. P.; Qin, Z.; Pérez Gallent, E.; Koper, M. T. M., Two Pathways for the Formation of Ethylene in CO Reduction on Single-Crystal Copper Electrodes. *Journal of the American Chemical Society* **2012**, *134* (24), 9864-9867.
72. Schouten, K. J. P.; Kwon, Y.; van der Ham, C. J. M.; Qin, Z.; Koper, M. T. M., A new mechanism for the selectivity to C₁ and C₂ species in the electrochemical reduction of carbon dioxide on copper electrodes. *Chemical Science* **2011**, *2* (10), 1902-1909.
73. Kas, R.; Kortlever, R.; Yilmaz, H.; Koper, M. T. M.; Mul, G., Manipulating the Hydrocarbon Selectivity of Copper Nanoparticles in CO₂ Electroreduction by Process Conditions. *ChemElectroChem* **2015**, *2* (3), 354-358.
74. Cook, R. L.; MacDuff, R. C.; Sammells, A. F., High Rate Gas Phase CO₂ Reduction to Ethylene and Methane Using Gas Diffusion Electrodes. *Journal of The Electrochemical Society* **1990**, *137* (2), 607-608.
75. Dinh, C.-T.; Burdyny, T.; Kibria, M. G.; Seifitokaldani, A.; Gabardo, C. M.; Arquer, F. P. G. d.; Kiani, A.; Edwards, J. P.; Luna, P. D.; Bushuyev, O. S.; Zou, C.; Quintero-Bermudez, R.; Pang, Y.; Sinton, D.; Sargent, E. H., CO₂ electroreduction to ethylene via hydroxide-mediated copper catalysis at an abrupt interface. *Science* **2018**, *360* (6390), 783-787.
76. Gabardo, C. M.; Seifitokaldani, A.; Edwards, J. P.; Dinh, C.-T.; Burdyny, T.; Kibria, M. G.; O'Brien, C. P.; Sargent, E. H.; Sinton, D., Combined high alkalinity and pressurization enable efficient CO₂ electroreduction to CO. *Energy & Environmental Science* **2018**, *11* (9), 2531-2539.
77. Ma, S.; Sadakiyo, M.; Luo, R.; Heima, M.; Yamauchi, M.; Kenis, P. J. A., One-step electrosynthesis of ethylene and ethanol from CO₂ in an alkaline electrolyzer. *Journal of Power Sources* **2016**, *301*, 219-228.
78. Ooka, H.; Figueiredo, M. C.; Koper, M. T. M., Competition between Hydrogen Evolution and Carbon Dioxide Reduction on Copper Electrodes in Mildly Acidic Media. *Langmuir* **2017**, *33* (37), 9307-9313.
79. Marcandalli, G.; Goyal, A.; Koper, M. T. M., Electrolyte Effects on the Faradaic Efficiency of CO₂ Reduction to CO on a Gold Electrode. *ACS Catalysis* **2021**, *11* (9), 4936-4945.
80. Goyal, A.; Marcandalli, G.; Mints, V. A.; Koper, M. T. M., Competition between CO₂ Reduction and Hydrogen Evolution on a Gold Electrode under Well-Defined Mass Transport Conditions. *Journal of the American Chemical Society* **2020**, *142* (9), 4154-4161.
81. Yoon, Y.; Hall, A. S.; Surendranath, Y., Tuning of Silver Catalyst Mesostructure Promotes Selective Carbon Dioxide Conversion into Fuels. *Angewandte Chemie International Edition* **2016**, *55* (49), 15282-15286.
82. Hall, A. S.; Yoon, Y.; Wuttig, A.; Surendranath, Y., Mesostructure-Induced Selectivity in CO₂ Reduction Catalysis. *Journal of the American Chemical Society* **2015**, *137* (47), 14834-14837.
83. Lu, Q.; Rosen, J.; Zhou, Y.; Hutchings, G. S.; Kimmel, Y. C.; Chen, J. G.; Jiao, F., A selective and efficient electrocatalyst for carbon dioxide reduction. **2014**, *5*, 3242.
84. Zhang, L.; Wang, Z. Y.; Mehio, N. D.; Jin, X. B.; Dai, S., Thickness- and Particle-Size-Dependent Electrochemical Reduction of Carbon Dioxide on Thin-Layer Porous Silver Electrodes. *ChemSusChem* **2016**, *9* (5), 428-432.

85. Sen, S.; Liu, D.; Palmore, G. T. R., Electrochemical Reduction of CO₂ at Copper Nanofoams. *ACS Catalysis* **2014**, *4* (9), 3091-3095.
86. Hossain, M. N.; Liu, Z.-G.; Wen, J.; Chen, A., Enhanced catalytic activity of nanoporous Au for the efficient electrochemical reduction of carbon dioxide. *Applied Catalysis B: Environmental* **2018**, *236*, 483-489.
87. Luo, W.; Zhang, J.; Li, M.; Züttel, A., Boosting CO Production in Electrocatalytic CO₂ Reduction on Highly Porous Zn Catalysts. *ACS Catalysis* **2019**, *9* (5), 3783-3791.
88. Chen, C.; Zhang, B.; Zhong, J.; Cheng, Z., Selective electrochemical CO₂ reduction over highly porous gold films. *Journal of Materials Chemistry A* **2017**, *5* (41), 21955-21964.
89. Peng, Y.; Wu, T.; Sun, L.; Nsanzimana, J. M. V.; Fisher, A. C.; Wang, X., Selective Electrochemical Reduction of CO₂ to Ethylene on Nanopores-Modified Copper Electrodes in Aqueous Solution. *ACS Applied Materials & Interfaces* **2017**, *9* (38), 32782-32789.
90. Gupta, N.; Gattrell, M.; MacDougall, B., Calculation for the cathode surface concentrations in the electrochemical reduction of CO₂ in KHCO₃ solutions. *Journal of Applied Electrochemistry* **2006**, *36* (2), 161-172.
91. Bockris, J. O. M., A Hydrogen Economy. *Science* **1972**, *176* (4041), 1323-1323.
92. Pentland, N.; Bockris, J. O. M.; Sheldon, E., Hydrogen Evolution Reaction on Copper, Gold, Molybdenum, Palladium, Rhodium, and Iron: Mechanism and Measurement Technique under High Purity Conditions. *Journal of The Electrochemical Society* **1957**, *104* (3), 182-194.
93. Bockris, J. O. M.; Pentland, N., The mechanism of hydrogen evolution at copper cathodes in aqueous solutions. *Transactions of the Faraday Society* **1952**, *48* (0), 833-839.
94. Hamelin, A.; Weaver, M. J., Dependence of the kinetics of proton reduction at gold electrodes on the surface crystallographic orientation. *Journal of Electroanalytical Chemistry and Interfacial Electrochemistry* **1987**, *223* (1), 171-184.
95. Strmcnik, D.; Lopes, P. P.; Genorio, B.; Stamenkovic, V. R.; Markovic, N. M., Design principles for hydrogen evolution reaction catalyst materials. *Nano Energy* **2016**, *29*, 29-36.
96. Zheng, Y.; Jiao, Y.; Vasileff, A.; Qiao, S.-Z., The Hydrogen Evolution Reaction in Alkaline Solution: From Theory, Single Crystal Models, to Practical Electrocatalysts. *Angewandte Chemie International Edition* **2018**, *57* (26), 7568-7579.
97. Anantharaj, S.; Noda, S.; Jothi, V. R.; Yi, S.; Driess, M.; Menezes, P. W., Strategies and Perspectives to Catch the Missing Pieces in Energy-Efficient Hydrogen Evolution Reaction in Alkaline Media. *Angewandte Chemie International Edition* **2021**, *60* (35), 18981-19006.
98. Firouzjaie, H. A.; Mustain, W. E., Catalytic Advantages, Challenges, and Priorities in Alkaline Membrane Fuel Cells. *ACS Catalysis* **2020**, *10* (1), 225-234.
99. Ledezma-Yanez, I.; Wallace, W. D. Z.; Sebastián-Pascual, P.; Climent, V.; Feliu, J. M.; Koper, M. T. M., Interfacial water reorganization as a pH-dependent descriptor of the hydrogen evolution rate on platinum electrodes. *Nature Energy* **2017**, *2* (4), 17031.
100. Intikhab, S.; Snyder, J. D.; Tang, M. H., Adsorbed Hydroxide Does Not Participate in the Volmer Step of Alkaline Hydrogen Electrocatalysis. *ACS Catalysis* **2017**, *7* (12), 8314-8319.

101. Subbaraman, R.; Tripkovic, D.; Chang, K.-C.; Strmcnik, D.; Paulikas, A. P.; Hirunsit, P.; Chan, M.; Greeley, J.; Stamenkovic, V.; Markovic, N. M., Trends in activity for the water electrolyser reactions on 3d M(Ni,Co,Fe,Mn) hydr(oxy)oxide catalysts. *Nature Materials* **2012**, *11*, 550.
102. Staszak-Jirkovský, J.; Malliakas, Christos D.; Lopes, Pietro P.; Danilovic, N.; Kota, Subrahmanyam S.; Chang, K.-C.; Genorio, B.; Strmcnik, D.; Stamenkovic, Vojislav R.; Kanatzidis, M. G.; Markovic, N. M., Design of active and stable Co–Mo–Sx chalcogels as pH-universal catalysts for the hydrogen evolution reaction. *Nature Materials* **2015**, *15*, 197.
103. Shinagawa, T.; Garcia-Esparza, A. T.; Takanahe, K., Insight on Tafel slopes from a microkinetic analysis of aqueous electrocatalysis for energy conversion. *Scientific Reports* **2015**, *5*, 13801.
104. Ledezma-Yanez, I.; Wallace, W. D. Z.; Sebastián-Pascual, P.; Climent, V.; Feliu, J. M.; Koper, M. T. M., Interfacial water reorganization as a pH-dependent descriptor of the hydrogen evolution rate on platinum electrodes. *Nature Energy* **2017**, *2*, 17031.
105. McCrum, I. T.; Koper, M. T. M., The role of adsorbed hydroxide in hydrogen evolution reaction kinetics on modified platinum. *Nature Energy* **2020**, *5* (11), 891-899.
106. Xue, S.; Garlyyev, B.; Watzele, S.; Liang, Y.; Fichtner, J.; Pohl, M. D.; Bandarenka, A. S., Influence of Alkali Metal Cations on the Hydrogen Evolution Reaction Activity of Pt, Ir, Au, and Ag Electrodes in Alkaline Electrolytes. *ChemElectroChem* **2018**, *5* (17), 2326-2329.
107. Trasatti, S.; Lust, E., The Potential of Zero Charge. **2002**.
108. Gileadi, E.; Argade, S. D.; Bockris, J. O. M., The Potential of Zero Charge of Platinum and Its pH Dependence. *The Journal of Physical Chemistry* **1966**, *70* (6), 2044-2046.
109. Shatla, A.; Landstorfer, M.; Baltruschat, H., On the differential capacity and pzc of Au(111) in some aprotic solvents. *ChemElectroChem* **2021**, *8*.
110. Valette, G., Double layer on silver single crystal electrodes in contact with electrolytes having anions which are slightly specifically adsorbed: Part II. The (100) face. *Journal of Electroanalytical Chemistry and Interfacial Electrochemistry* **1982**, *138* (1), 37-54.
111. Trasatti, S., Work function, electronegativity, and electrochemical behaviour of metals: II. Potentials of zero charge and "electrochemical" work functions. *Journal of Electroanalytical Chemistry and Interfacial Electrochemistry* **1971**, *33* (2), 351-378.
112. Garcia-Araez, N.; Climent, V.; Feliu, J., Potential-Dependent Water Orientation on Pt(111), Pt(100), and Pt(110), As Inferred from Laser-Pulsed Experiments. Electrostatic and Chemical Effects. *The Journal of Physical Chemistry C* **2009**, *113* (21), 9290-9304.
113. Ganassin, A.; Sebastián, P.; Climent, V.; Schuhmann, W.; Bandarenka, A. S.; Feliu, J., On the pH Dependence of the Potential of Maximum Entropy of Ir(111) Electrodes. *Scientific Reports* **2017**, *7* (1), 1246.
114. Martínez-Hincapié, R.; Sebastián-Pascual, P.; Climent, V.; Feliu, J. M., Exploring the interfacial neutral pH region of Pt(111) electrodes. *Electrochemistry Communications* **2015**, *58*, 62-64.
115. Sebastian, P.; Martínez-Hincapie, R.; Climent, V.; Feliu, J. M., Study of the Pt (111) vertical bar electrolyte interface in the region close to neutral pH solutions by the laser induced temperature jump technique. *Electrochimica Acta* **2017**, *228*, 667-676.

116. Chen, X.; McCrum, I. T.; Schwarz, K. A.; Janik, M. J.; Koper, M. T. M., Co-adsorption of Cations as the Cause of the Apparent pH Dependence of Hydrogen Adsorption on a Stepped Platinum Single-Crystal Electrode. *Angewandte Chemie International Edition* **2017**, *56* (47), 15025-15029.
117. McCrum, I. T.; Janik, M. J., pH and Alkali Cation Effects on the Pt Cyclic Voltammogram Explained Using Density Functional Theory. *The Journal of Physical Chemistry C* **2016**, *120* (1), 457-471.
118. Strmcnik, D.; Uchimura, M.; Wang, C.; Subbaraman, R.; Danilovic, N.; van der Vliet, D.; Paulikas, A. P.; Stamenkovic, V. R.; Markovic, N. M., Improving the hydrogen oxidation reaction rate by promotion of hydroxyl adsorption. *Nature Chemistry* **2013**, *5*, 300.
119. Resasco, J.; Chen, L. D.; Clark, E.; Tsai, C.; Hahn, C.; Jaramillo, T. F.; Chan, K.; Bell, A. T., Promoter Effects of Alkali Metal Cations on the Electrochemical Reduction of Carbon Dioxide. *Journal of the American Chemical Society* **2017**, *139* (32), 11277-11287.
120. Ringe, S.; Clark, E. L.; Resasco, J.; Walton, A.; Seger, B.; Bell, A. T.; Chan, K., Understanding cation effects in electrochemical CO₂ reduction. *Energy & Environmental Science* **2019**, *12* (10), 3001-3014.
121. Goyal, A.; Koper, M. T. M., The Interrelated Effect of Cations and Electrolyte pH on the Hydrogen Evolution Reaction on Gold Electrodes in Alkaline Media. *Angewandte Chemie International Edition* **2021**, *60* (24), 13452-13462.



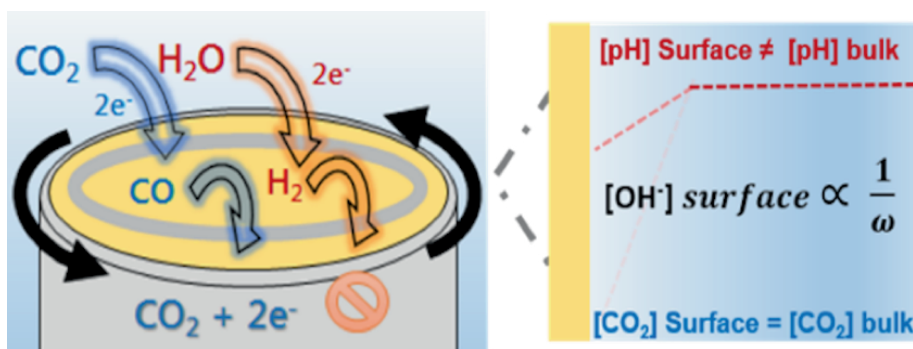
Chapter 2

Competition between CO_2 reduction and hydrogen evolution on a gold electrode under well-defined mass transport conditions



Abstract

Gold is one of the most selective catalysts for the electrochemical reduction of CO₂ (CO₂RR) to CO. However, the concomitant hydrogen evolution reaction (HER) remains unavoidable under aqueous conditions. In this work, a rotating ring disk electrode (RRDE) set-up has been developed to study quantitatively the role of mass transport in the competition between these two reactions on the Au surface in 0.1 M bicarbonate electrolyte. Interestingly, while the Faradaic selectivity for CO formation was found to increase with enhanced mass transport (from 67% to 83%), this effect is not due to an enhancement of CO₂RR rate. Remarkably, the inhibition of the competing HER from water reduction with increasing disk rotation rate is responsible for the enhanced CO₂RR selectivity. This can be explained by the observation that on the Au electrode, water reduction improves with more alkaline pH. As a result, the decrease in the local alkalinity near the electrode surface with enhanced mass transport, suppresses HER due to the water reduction. Our study shows that controlling the local pH by mass transport conditions can tune the HER rate, in-turn regulating the CO₂RR and HER competition in the general operating potential window for CO₂RR (-0.4 V to -1V vs RHE).



This chapter is based on the article:

Goyal, A.; Marcandalli, G.; Mints, V. A.; Koper, M. T. M., Competition between CO₂ Reduction and Hydrogen Evolution on a Gold Electrode under Well-Defined Mass Transport Conditions. *Journal of the American Chemical Society* **2020**, *142* (9), 4154-416

2.1. Introduction

The electrochemical reduction of carbon dioxide has the potential of storing excess renewable electricity in carbon-based (liquid) fuels and chemicals. At present, however, the economic feasibility of electrochemical CO₂ reduction reaction (CO₂RR) remains an issue, primarily due to its low energy efficiency at high current densities.¹⁻³ One key factor for this efficiency loss is the competition from the hydrogen evolution reaction (HER), which is virtually unavoidable in the aqueous (bicarbonate) electrolytes in which this reaction is generally carried out.⁴⁻⁶ Most research until now has focused on understanding the role of the intrinsic properties of the catalyst surface on the kinetics and the eventual product selectivity of CO₂ reduction, in competition with the HER.⁶⁻¹² The role of the local concentrations of various reactive species (such as CO₂, HCO₃⁻, OH⁻ and H⁺), on the competition between these interfacial reactions has received less scrutiny.¹³⁻¹⁵ A weakly buffered electrolyte like bicarbonate will develop diffusional gradients of the aforementioned species, caused by their interfacial reactions at the electrode and the sluggish acid-base equilibrium of bicarbonate.¹⁶⁻¹⁸ Hence, these concentration gradients are expected to play an important role in the kinetic bifurcation between CO₂RR and HER. In principle, an enhanced mass transport can help in mitigating the concentration gradients at the interface by transporting the CO₂ from the bulk to the interface and at the same time sweeping away the OH⁻ ions formed in the vicinity of the electrode. Therefore, studies performed under well-defined mass transport conditions can give indispensable information about the near electrode concentration gradients and their impact on the competition between the HER and CO₂RR. In this regard, several recent studies have employed porous electrode morphologies for CO₂RR, with the aim of controlling the diffusional concentration gradients within the porous channels by changing the catalyst thickness/roughness in a systematic fashion.^{15, 19-23} Generally it is observed that the selectivity towards CO₂RR can be improved by increasing the thickness/roughness of the porous channels of the catalyst layer, which has been attributed to the suppression of bicarbonate-mediated HER. However, contradicting conclusions have been drawn on the role of concentration gradients (i.e. mass transport limitation) for the CO formation rate. In a study on porous Au catalysts performed by Surendranath and co-workers, the CO formation rate was shown to be largely independent of the thickness of the porous catalysts.¹⁵ The authors attributed this to the negligible concentration gradients for CO₂ within the porous channels, which is also in accordance with the slow hydration kinetics of CO₂-bicarbonate system (equation 1, $t_{1/2} = 19$ s at near-neutral pH):²⁴



However, in a similar study by Cheng and co-workers, a contrasting dependence of CO₂RR partial current density on porous structures was reported. They showed that the rate of CO formation decreases with increasing roughness of the porous Au catalyst, which was attributed to the increasing mass transport limitation for CO₂ in the rougher porous channels.

It is also interesting to note that in a separate study on porous Ag catalysts by Surendranath and co-workers, the partial current density for CO formation increased with increasing thickness of the porous channels,²² in contrast with their results on porous Au catalysts. The authors speculated that it might be related to details of the mechanistic pathway of CO₂RR. Additionally, Bell and co-workers also conducted mass transport dependent studies on planar Ag electrodes wherein they tuned the flow rate of CO₂/electrolyte to control the mass transport to the electrode.²⁵⁻²⁶ Similar to Cheng and co-workers, they reported that the rate of CO formation increases with the increasing mass transport (flow rate) and hence concluded that CO₂RR is mass transport dependent. Interestingly, in contrast with the previous studies, they observed that the rate of the competing HER decreased with the increasing flow rate (i.e. mass transport). However, this trend was not discussed in further detail by the authors.

Summarizing, the current literature presents apparently conflicting results on the role of local concentration gradients, even under relatively similar experimental conditions (electrolyte identity, roughness factor, applied overpotential etc.). In the existing studies, the lack of precise control on the various aspects of the catalytic structure (such as pore size, length, facets, grain size, tortuosity etc.) leads to a complicated mass transport effect and various ambiguities still remain about the role of concentration gradients on the reaction kinetics of CO₂RR and HER.

Another limitation that mires the current understanding of near electrode reactant/product distribution during CO₂RR, arises from the use of bulk electrolysis analysis, performed in tandem with offline sampling techniques (such as gas chromatography and high performance liquid chromatography).^{4-5, 7, 27} These analytical techniques do not capture the dynamic evolution of the local concentration gradients with the real-time evolution of the products. This is an issue especially for CO₂RR studies, since the concentration gradients generated by interfacial heterogeneous reactions (CO₂RR and HER) also shift the corresponding homogeneous acid – base equilibria of the electrolyte.^{18, 28-31} In a recent paper by Nocera and co-workers it was shown that CO₂RR studies performed on long-time scales (≈ 20 min, gas chromatographic analysis) are intimately entangled with the homogenous reactions happening in the electrolyte.³⁰ The authors showed that it is necessary to take the roughness factor as well as the bicarbonate equilibria equations into account for formulating a micro-kinetic model that could explain the observed results on Au catalysts of different morphologies. In the light of this work, it should be expected that previous offline studies on porous electrodes also suffered from an unwanted participation of homogenous reactions in the overall concentration gradients at the interface. Hence, a technique that allows for the online and immediate analysis of the product distribution should lead to a better understanding of the interplay between the reactions at the electrode (HER and CO₂RR) and the corresponding acid-base equilibria in the bicarbonate electrolyte that happen at transient time-scales.^{24, 26}

Here, we develop a rotating ring disk electrode (RRDE) voltammetry method to circumvent the abovementioned limitations. By a judicious choice of the ring material (namely gold), this method allows us to study the competition between CO₂RR and HER on a gold electrode quantitatively, with a high time resolution under well-defined mass transport conditions. Previous RRDE studies on CO₂RR used a Pt ring, where CO stripping was performed to calculate the Faradaic efficiency of CO₂RR.³²⁻³³ However, similar to the offline techniques, such stripping experiments do not shed light on the real-time evolution of local electrolyte composition and its influence on the competition between CO₂RR and HER. Kriek and co-workers performed an online investigation where they employed the RRDE-technique featuring a Pt-ring electrode to quantify the H₂ evolved at the disk.³⁴ However, due to the non-selective oxidation behavior of Pt for H₂ and CO, this method does not allow for any quantitative analysis. The main advantage of the RRDE set-up introduced in this study arises from the use of a gold ring, which can selectively oxidize CO under diffusion limited conditions, while being inactive for hydrogen oxidation reaction (HOR). Au is known to be an excellent catalyst for CO oxidation, reaching diffusion limited currents both at acidic and alkaline pH values.³⁵⁻³⁸

We will show here that under well-defined mass transport conditions, the rate of CO₂RR is largely independent of the mass transport effects (i.e. disk rotation rate). However, the overall Faradaic selectivity for CO₂RR improves with increasing disk rotation speed (enhanced mass transport) which is caused by the decreasing rate of HER. We show that at 0.1 M bicarbonate concentration, water reduction is the dominant branch of HER competing with CO₂RR, and that enhanced mass transport essentially mitigates the local alkalinity, thereby suppressing the water reduction rate. Our work shows that control of mass transport conditions is important for selective CO₂RR in ways that have not been elucidated previously, and provides rational guidelines for steering concentration gradients and product selectivity in practical electrode geometries.

2.2. Experimental section

2.2.1. Chemicals

The electrolytes were prepared from H₂SO₄ (98%, EMSURE, Merck), NaHCO₃ (≥ 99.7%, Honeywell Fluka), NaClO₄ (99.99%, trace metals basis, Sigma-Aldrich), NaOH (32% by wt. solution, analysis grade, Merck) and Ultrapure water (MilliQ gradient, ≥18.2 MΩcm, TOC < 5 ppb). Ar (6.0 purity, Linde), CO (4.7 purity, Linde), CO₂ (4.5 purity, Linde) and H₂ (5.0 purity, Linde) were used for purging the electrolytes. The dopamine coating for the modification of RRDE was prepared from dopamine hydrochloride (≥98.5%, Sigma-Aldrich). For collection efficiency determination, K₃Fe(CN)₆ (> 99%, Sigma Aldrich) was used.

2.2.2. General electrochemical methods

All the electrochemical measurements were carried out in home-made borosilicate glass cells in which the reference electrode was separated from the working compartment with the help of a Luggin capillary. The counter

electrode (Au wire, 99.99% purity, unless otherwise stated) was separated from the working compartment with a fine porous frit. The glassware was cleaned prior to each experiment by boiling it five times in ultrapure water. When not in use, the glassware was stored in 1 g/L solution of KMnO_4 (acidified). Before boiling, any traces of KMnO_4 and MnO_2 were removed from the glassware by submerging it in a diluted solution of acidified H_2O_2 (few drops of conc. H_2SO_4 and 10-15 mL H_2O_2 in excess water) for half an hour. Before every experiment, the electrolytes were purged for ca. 20 minutes with the suitable gas required for the experiment, namely, Ar for electrochemical characterization and HER studies, H_2 for HOR studies, CO for CO oxidation studies, and CO_2 for CO_2RR studies. This was done to remove any dissolved oxygen from the electrolyte. Moreover, during the measurements, gases were also bubbled over the headspace of the electrochemical cell, in order to eliminate any interference from ambient oxygen. For the electrochemical polishing/characterization as well as for the CO oxidation, HOR and HER studies, a home-made reversible hydrogen electrode (RHE) was used as the reference electrode. For the CO_2RR measurements and collection efficiency determination, a Ag/AgCl reference electrode (Pine Research Instrumentation, sat. KCl, $E = 0.197$ V vs. standard hydrogen electrode) was used and the potentials were later converted to the RHE scale for reporting. All the electrochemical measurements were carried out either using an IviumStat bipotentiostat (Ivium Technologies) or a Biologic (VSP-300) potentiostat. For all the measurements, 85% Ohmic drop compensation was performed. The Ohmic drop of the electrolyte was determined by carrying out electrochemical impedance spectroscopy (EIS) at open circuit potential, unless otherwise stated. The RRDE/rotating disk electrode (RDE) measurements were performed with a Modulated Speed Rotator and E6/E5 ChangeDisk tips in a PEEK shroud (Pine Research).

2.2.3. Working electrode preparation and dopamine modification

Before each experiment, the gold disk (diameter = 5mm, Pine instruments) was mechanically polished on Buehler micro-polishing cloth (8 inches) with decreasing sizes of diamond polishing suspension, namely, $3\mu\text{m}$, $1\mu\text{m}$ and $0.25\mu\text{m}$. Next, the disk was sonicated in ultrapure water and acetone for 10 minutes to remove any organic/inorganic impurities, and mounted on the RRDE/RDE tip depending on the experiment that was performed. For the RRDE tip, the Au disk and Au ring were short-circuited in order to electrochemically polish the system in 0.1 M H_2SO_4 (0.05 V to 1.75 V vs RHE, 200 cycles at a scan rate of 1Vs^{-1}) by going to the Au oxide formation and reduction region.³⁹ For the RDE measurements, the Au disk was electro-polished without short-circuiting. A characterization cyclic voltammetry (CV) of the ring and disk as well as just the disk was obtained in the same potential window where the electrochemical polishing was performed (at a scan rate of 50mVs^{-1}). The electrochemically active surface area (ECSA) of the disk was determined by calculating the charge from the reduction peak in the characterization CV and dividing it by the specific charge of one

monolayer of Au ($390 \mu\text{C cm}^{-2}$).³⁹ The working electrode was then ready for the electrochemical measurements.

For the CO₂RR experiments as well as for collection efficiency determination, further modification of the RRDE tip was performed by coating it with dopamine.⁴⁰ This was done to prevent bubble attachment on the Teflon spacer between the disk and the ring of the RRDE tip, which interferes with the RRDE collection factor. Briefly, the RRDE tip was immersed in a 2g/L solution of dopamine hydrochloride (prepared with 20 mL buffer of pH \approx 7) for 2 hours, where the RRDE was rotated at 400 rotations per minute (rpm). After the coating, the ring and the disk were electrochemically polished once again in 0.1 M H₂SO₄ electrolyte, in order to remove any dopamine that may have deposited on the ring and/or disk. Next, a characterization CV was obtained for the ring and the disk as well as just the disk and they were compared with the characterization CVs of the unmodified surface (as shown in Appendix A Figure S1). A good agreement between these CVs indicated that the surface morphology and ECSA did not change before and after the coating procedure, and hence further experiments could be done without any additional modifications.

2.2.4. CO oxidation and CO₂RR studies

For the determination of a suitable ring potential and for validation of the existence of purely mass transport limited currents on the ring, CO oxidation was performed in CO saturated 0.1 M NaHCO₃ electrolyte. For these experiments an RDE tip was used instead of the RRDE tip and no dopamine modification was performed. The working electrode was prepared and characterized as outlined in section 2.3 and the general electrochemical procedure is outlined in section 2.2. Once the electrolyte was saturated with CO (for c.a. 20 min.), CO oxidation CVs were obtained in the potential window of 0.05 V to 1.2V vs RHE (scan rate of 25 mVs⁻¹) according to the previously reported studies.³⁸ Measurements were done at six different rotation speeds, namely, 400 rpm, 800 rpm, 1200 rpm, 1600 rpm, 2000 rpm, and 2500 rpm. Thereafter, the electrolyte was saturated with H₂ and the measurements were repeated in the same potential window, in order to determine if the surface is active for HOR in the given potential window.

For the RRDE experiments, the working electrode was prepared as mentioned in section 2.3. The measurements were done in CO₂ saturated 0.1 M NaHCO₃ electrolyte. The ring potential was set to 1 V vs RHE (unless otherwise stated) and the disk was cycled in the potential window of 1.75 V to -1 V vs RHE at a scan rate of 25 mVs⁻¹, with the ring current measured simultaneously. It was observed that at potentials more negative than -1 V (vs RHE), the RRDE tip suffered from bubble attachment and hence, it was not possible to go to more negative potentials in these experiments. The measurements were performed at six different rotation speeds, namely, 400 rpm, 800 rpm, 1200 rpm, 1600 rpm, 2000 rpm, and 2500 rpm and the CO₂RR and HER currents were de-convoluted after the experiments according to section 2.7. In order to make sure that the surface did not change during the measurement, the disk and the ring were short-circuited and cycled in the Au oxide formation/reduction potential window in the

working cell (0.05 V to 1.75 V vs RHE) in between every measurement. Post experiment, the ring currents were corrected for any possible time-delay, by obtaining the difference between the maxima of the disk-ring currents (vs. time) and correcting the potential on the ring correspondingly. Generally, the maxima of the two currents coincided (as shown in Appendix A Figure S2) and hence, no time-delay corrections had to be performed at the investigated rotation speeds (≥ 800 rpm).

2.2.5. Collection efficiency determination

The apparent collection efficiency of the ring was determined after every RRDE experiment, in order to account for the changes in tip geometry that incur with the assembling of the tip. 5 mM K_3FeCN_6 was added to the working cell (Ar sat. 0.1 M $NaHCO_3$). Thereafter, the disk was cycled between -0.45 V to 0.54 V (vs Ag/AgCl) and the ring potential was set to -0.23 V (vs Ag/AgCl). The readings were taken at different rotation speeds and the collection efficiency was determined by using equation 2. It should be noted here that the RRDE tip was mechanically polished prior to each run to avoid any possible effects from the gold corrosion induced by hexacyanoferrates during the collection efficiency determination.⁴¹

2.2.6. HER studies in $NaHCO_3$ and NaOH

For direct comparison with RRDE experiments, HER studies were done in Ar saturated 0.1 M $NaHCO_3$ electrolyte; for this experiment, an RHE reference and an RDE tip were used. The working electrode was prepared according to section 2.3. The CVs were taken in the potential window of 0 V to -1 V vs RHE at a scan rate of 25 mVs^{-1} at different rotation speeds. Additional studies were also done at different bicarbonate concentrations (0.025 M, 0.05 M, 0.2 M, 0.4 M and 0.5 M) by following the same procedure as above. In order to study the role of pH on water reduction reaction, further studies were done at pH 10, 11, 12 and 13 by using NaOH, where the ionic strength of the electrolyte was maintained at 0.1 M by adding $NaClO_4$. This was done in order to eliminate any effects from the cation concentration changes in the bulk and to have a comparable ionic strength with the experiments done in $NaHCO_3$. In these studies, the CVs were taken in the potential window of 0 V to -0.8 V vs RHE at a scan rate of 25 mVs^{-1} , at 2500 rpm.

2.2.7. RRDE set-up: development and methodology

The advantage of the RRDE set-up used in this work hinges on the selective oxidation of CO on the Au ring, under diffusion limited conditions. As has been mentioned in the Introduction, CO oxidation has been shown to reach diffusion limited currents on the Au electrode surface both for acidic and alkaline pH values. However, there are no studies for CO oxidation on Au in a bicarbonate electrolyte (pH ≈ 7). The onset of CO electro-oxidation on the Au surface is pH dependent, with the more alkaline pH showing less positive onset potential.³⁶ Moreover, in the presence of strongly adsorbing anions, the CO oxidation reaction can be hampered, because anions can block the surface for OH^- ions, which are essential for CO oxidation mechanism.⁴² Therefore, it is important to investigate the CO oxidation reaction on Au in

the bicarbonate electrolyte system and determine the potential window where this reaction reaches diffusion limitation (if at all). Hence, we performed CO oxidation in 0.1 M NaHCO₃ using a gold RDE. In Figure S3 (Appendix A) we show that CO oxidation has an onset potential of ca. 0.4 V vs RHE and reaches diffusion limitation in the potential window of 0.7 to 1.1 V in 0.1 M NaHCO₃ (CO sat.) electrolyte. Moreover, the Koutecky-Levich analysis at 1 V (Fig. S3, inset) is linear with an intercept ≈ 0 , providing further confirmation that there is no kinetic limitation for the process in the given potential window. Thereafter, the Au surface was also studied in H₂ atmosphere in the bicarbonate electrolyte at different rotation speeds in the same potential window, to make sure that the surface is not active for HOR under these conditions. Figure S4 (Appendix A) illustrates that the current has no rotation speed dependence in the presence of H₂, which establishes that only double layer charging occurs on the Au surface. Hence, these studies confirm that the proposed RRDE set-up is suitable for the quantitative detection of CO during CO₂RR in bicarbonate electrolytes. Furthermore, based on the Koutecky-Levich analysis the ring potential was set to 1 V vs RHE for the studies performed with the RRDE.

The apparent collection efficiency (N , refer to equation 2) of the dopamine modified RRDE tip was evaluated by using the Fe[CN]₆³⁻/Fe[CN]₆⁴⁻ redox couple (as outlined in section 2.5) and it was determined to be 0.23 (± 0.02). This is in good agreement with the reported literature value.⁴³ This also confirms that the dopamine coating on the Teflon spacer does not interfere with the mass transfer equations and the boundary conditions that are applicable for the RRDE set-up.⁴⁴ Hence, the dopamine modification of the RRDE tip provided a stable and reproducible collection efficiency in the potential window of the RRDE experiments (0 to -1 V vs RHE), which is essential for the quantification of CO₂RR and HER using this set-up.

$$N = \left| \frac{i_{disk}}{i_{ring}} \right| \quad (2)$$

The RRDE set-up can be used for the deconvolution of CO₂RR and HER under the assumption that H₂ and CO are the only products on the Au polycrystalline disk in the potential window of our studies. This is a reasonable assumption given that most long-term electrolysis studies have determined CO to be the only appreciable product of CO₂ reduction on Au surface.^{4, 6, 27} The partial current density for CO formation can be simply calculated from the experimental ring current (i_{ring}) and the experimentally determined apparent collection efficiency (N) as:

$$J_{CO} = \frac{-i_{ring}}{N \times ECSA_{disk}} \quad (3)$$

where ECSA_{disk} is the electrochemically active surface area of the disk which has been determined according to experimental section 2.3. The Faradaic efficiency for CO formation can be calculated as:

$$FE_{CO} = \frac{i_{ring} \times 100}{|i_{disk}| \times N} \quad (4)$$

where i_{disk} is the experimentally obtained total current on the disk during the RRDE measurements in 0.1 M NaHCO₃ (CO₂ sat., pH ≈ 6.9) electrolyte. The partial current density and Faradaic efficiency for HER can be calculated from:

$$J_{HER} = J_{disk} - J_{CO} \quad (5)$$

$$FE_{HER} = 100 - FE_{CO} \quad (6)$$

where J_{disk} is the total current density during RRDE measurements calculated by dividing the i_{disk} with the electrochemically active surface area of the disk (ECSA_{disk}). Thus, the RRDE set-up employed can be used for the online quantitative studies on the competition between HER and CO₂RR, under well-defined mass transport conditions.

2.3. Results and discussion

Figure 1 shows the results of an experiment in which the effect of the mass transport rate (disk rotation rate) and electrode potential on the CO₂RR Faradaic selectivity are summarized, based on the data shown in Figure 2. Figure 2a shows the total current density measured on the disk, and Figure 2b shows the associated ring current corresponding to CO oxidation during a typical RRDE experiment. Following the procedure outlined in section 2.7, the partial current densities for the reduction of CO₂ to CO and the competing HER are plotted in Figures 2c and 2d, respectively. From the results in Figure 2c and 2d, the Faradaic efficiency for the conversion of CO₂ to CO can be evaluated as a function of disk rotation rate and electrode potential, as shown in Figure 1. It should be noted here that the Faradaic selectivity trend with the applied potential is identical to previous studies that were performed using long-term electrolysis, with a maximum Faradaic efficiency of 83% for CO formation achieved at -0.6 V (vs RHE).⁴⁻⁵

Furthermore, Figure 1 shows that the Faradaic efficiency for CO formation increases with higher mass transport rate, in agreement with previous studies performed by Bell and co-workers and Cheng and co-workers.^{23, 25} However, the reason for the enhanced efficiency is not, or not only, the improved mass transport of CO₂, but rather the lower rate of HER with increased disk rotation rate. In fact, Figure 2c shows that the CO₂RR rate itself does not strongly depend on the rotation rate. This alludes to the lack of CO₂ concentration depletion at the interface, either via the heterogeneous CO₂RR or via the shift of the homogeneous CO₂ hydration equilibria. CO₂RR induced CO₂ depletion is understandably absent, on account of the low experimental current densities which are at least an order of magnitude lower than the theoretically limiting current densities (see Table S1 in Appendix A). This is in contrast with the previous studies by Bell and co-workers, who observed that the partial current density for CO formation increased with increasing flow rate.²⁵⁻²⁶ However, it should be noted that

their studies involved drastically different diffusion layer thicknesses ($\geq 100 \mu\text{m}$) compared to the RRDE set-up discussed here ($\leq 2 \mu\text{m}$). Hence, it appears that mass transport limitations become operational for CO₂RR only in the cases where diffusion layer thicknesses are at least few orders of magnitude higher than the present study. Notably, the local pH gradient, which is dependent on rotation rate, does not deplete the CO₂ concentration at the interface (according to equation 1), suggesting that the convection control alleviates the homogenous depletion of CO₂, in accordance with the slow kinetics of this reaction ($t_{1/2} = 19\text{s}$, at near-neutral pH). This is in agreement with a previous study by Xu and co-workers, who showed that a stirring rate of $\geq 450 \text{ rpm}$ suffices to maintain the CO₂ concentration at the interface to its bulk value.^{13, 16} This shows that a stable rate for CO formation can be achieved by maintaining the CO₂ bulk concentration at the interface and appropriate convection control is a straightforward route to achieve that.

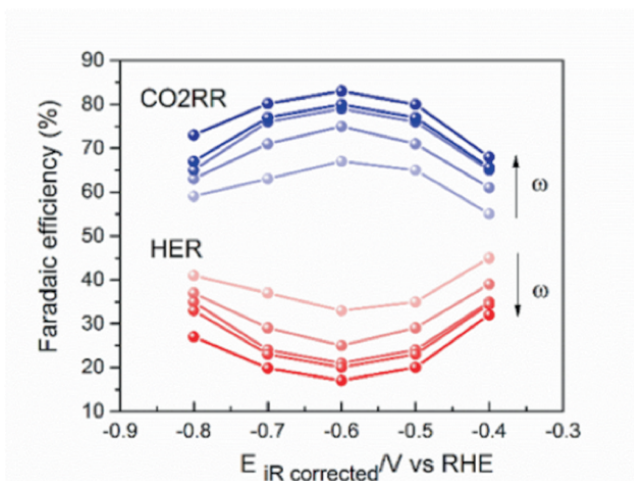


Figure 2 Faradaic efficiency for CO formation (blue) and HER (red) as a function of potential (vs RHE) and rotation rate for Au polycrystalline surface in CO₂ sat. 0.1 M NaHCO₃ (bulk pH = 6.8) as calculated from equation 4 and 6 respectively. The direction of the arrow indicates increasing rotation speed, from 800 to 2500 rpm.

Since the change in Faradaic efficiency of CO₂RR with the rotation rate is intimately related to the HER rate, we have studied the rotation rate and pH dependence of the HER separately.

HER in bicarbonate (near-neutral pH) can be considered to proceed via two pathways, either by the so-called proton reduction where HCO₃⁻ acts as the proton donor or via water reduction (shown in eqn. 7 and 8, respectively).⁴⁵⁻⁴⁶



For HCO₃⁻ mediated HER, increasing the rotation rate will promote the rate of the reaction by transporting away the OH⁻ ions formed in the vicinity of

the electrode, thereby alleviating the homogenous depletion of bicarbonate by reaction 9:

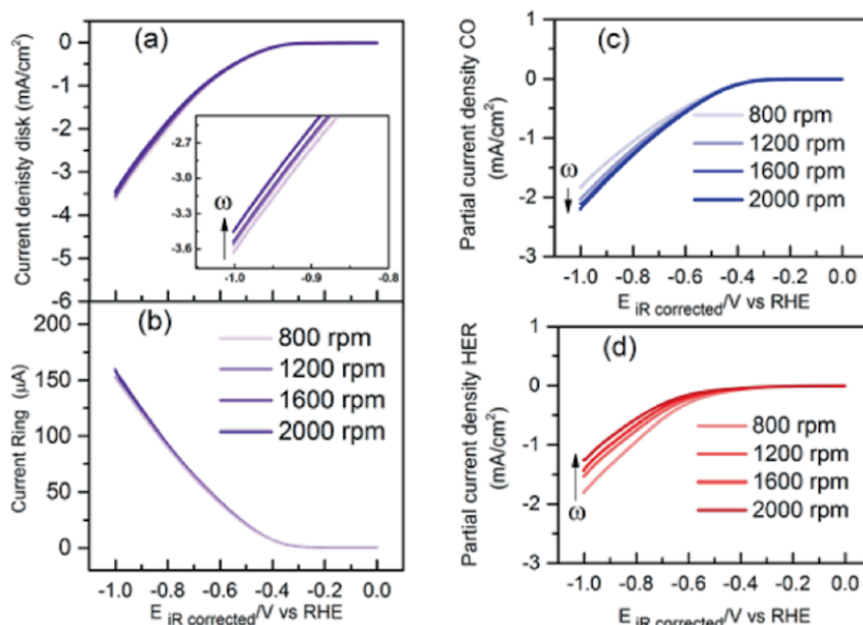
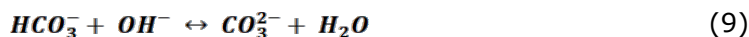


Figure 3 (a) Total current density on the Au polycrystalline disk at different rotation speeds (b) Associated CO oxidation current on Au ring at different rotation speeds during RRDE studies in CO_2 sat. 0.1 M NaHCO_3 (bulk $\text{pH} = 6.8$) with a scan rate of 25 mVs^{-1} . De-convoluted (c) Partial current density for CO formation (d) Partial current density for HER, as calculated from the RRDE experiments according to equation 3 and 5 respectively. The direction of the arrow indicates increasing rotation rate in all the figures.

Consequently, with decreasing local alkalinity, the availability of HCO_3^- for contributing to HER will increase. However, the opposite rotation rate dependence for HER activity is observed in our experiments (as shown in Figure 2d). Notably, these results are in agreement with the previous studies by Bell and co-workers wherein they reported that on planar Ag foils, partial current density for HER decreases with increasing mass transport (flow rate) in 0.1 M bicarbonate electrolytes.²⁵⁻²⁶ However, the nature of this effect was not discussed in further detail. We further investigated the rotation rate dependence of HER in Ar sat. NaHCO_3 (shown in Figure 3) so as to eliminate any possible artefact from the simultaneous CO_2RR . However, a similar rotation rate dependence is observed for HER, both in Ar sat. and CO_2 sat. 0.1 M bicarbonate electrolyte. Hence, the experimental data shows that water reduction is more likely to be the dominating branch for HER in 0.1 M bicarbonate electrolyte. We note that at higher buffer strength of the electrolyte (0.5 M NaHCO_3), the rotation rate dependence of HER is in fact reversed (as shown in Figure S5, Appendix A).

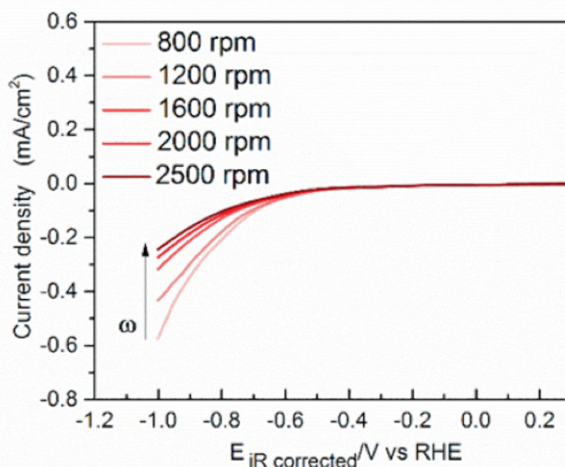


Figure 4 CVs obtained at different rotation rates for HER using the RDE on Au polycrystalline surface in Ar sat. 0.1 M NaHCO₃ (bulk pH = 9) at 25 mVs⁻¹. The direction of the arrow indicates increasing rotation rate.

Further analysis with increasing bicarbonate concentration (as shown in Figure 4) shows that the dominant branch tips towards the bicarbonate-mediated HER with the increasing buffer capacity of the electrolyte (≈ 0.2 M bicarbonate). Hence, the dominant branch of HER is fundamentally dependent on the polarization induced pH gradient at the interface, which is influenced by the electrolyte buffer strength as well as by the rotation rate. In-fact, the rotation speed dependence of HER is a straight forward way to ascertain the dominant branch of HER under given experimental conditions. We focus here on the role of rotation rate in determining CO₂RR/HER selectivity only in 0.1 M bicarbonate electrolyte as it has been shown previously that at this bicarbonate concentration the selectivity towards CO is optimal.^{17, 47-48} An in-depth study on the effect of changing electrolyte buffer strength for CO₂RR/HER selectivity will be presented elsewhere. Note that the absolute currents for HER are higher under CO₂ sat. conditions (Fig. 2d) compared to the Ar sat. conditions (fig 3). This can be attributed to the lower concentration of HCO₃⁻ (≈ 0.095 M) under Ar sat. electrolytes (pH =9), due to the bicarbonate-carbonate speciation reaction.⁴⁸ Once the CO₂ is bubbled into the electrolyte, it equilibrates with the hydroxyl ions to give back the bicarbonate and hence CO₂ saturated conditions enhance the contribution from bicarbonate mediated HER. Nevertheless, a similar rotation speed dependence indicates that water reduction provides the majority current in 0.1 M bicarbonate electrolyte, under both the environments (Ar and CO₂) that are investigated.

Since water reduction determines the overall selectivity under the given experimental conditions, water reduction reaction was probed further at alkaline pH (pH 10 to pH 13) in order to circumvent any interference from other Faradaic processes. Interestingly, it was observed that on a Au

polycrystalline surface, HER due to water reduction increases with increasing alkalinity (as shown in Figure 5).

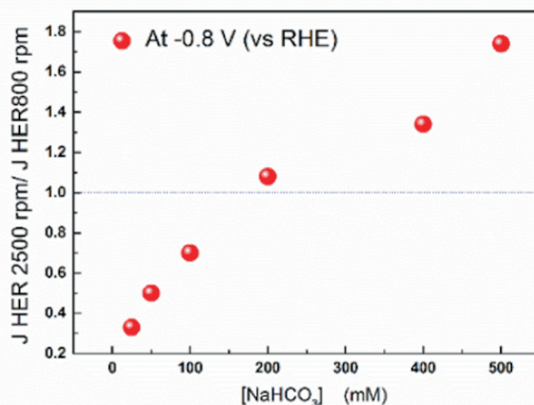


Figure 5 Ratio of HER current density at 2500 rpm and 800 rpm at -0.8 V (vs RHE) as a function of the sodium bicarbonate concentration in mM, obtained under Ar sat. conditions on Au polycrystalline surface using RDE. A ratio of less than 1 indicates that the water reduction is the dominant branch of HER and a ratio of greater than 1 indicates that bicarbonate mediated HER is the dominant branch.

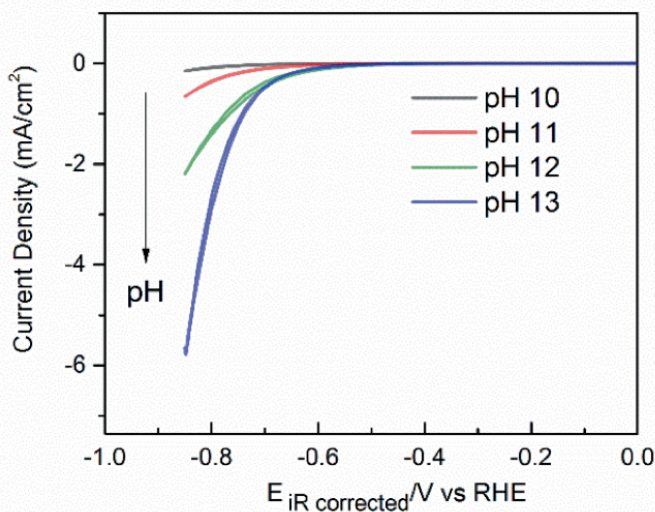


Figure 5 CVs obtained for HER on Au polycrystalline surface at 2500 rpm in 0.1 M NaOH (pH 13), 0.01 M NaOH + 0.09 M NaClO₄ (pH 12), 0.001 M NaOH + 0.099 M NaClO₄ (pH 11) and 0.0001 M NaOH + 0.0999 M NaClO₄ (pH 10), at 25 mVs⁻¹. The direction of the arrow indicates increasing bulk pH.

These results are counter-intuitive since water reduction reaction is expected to be pH independent and hence it should not be affected either by the bulk pH or by the local pH variations. However, the pH dependence for HER on gold in alkaline media as shown in Fig. 5 has been observed before.⁴⁹⁻⁵¹ More recently, Bell and co-workers have also reported a

comparable trend for the pH dependence of HER on polycrystalline Cu surface.⁵² Further investigations are needed in order to fully understand the pH dependence of water reduction reaction on gold. Notably, in contrast with the Au surface, Pt (111) surface shows a decrease in water reduction activity with the increasing alkalinity.⁵³ However, given the opposite cation effect for water reduction reaction on these surfaces, a different pH dependence is not unexpected.⁵⁴ The important point to make here is that the pH dependence for water reduction on the Au surface agrees very well with the observed decrease of the HER rate with increasing rotation rate in 0.1 M bicarbonate electrolyte. Since the OH⁻ ions are transported away from the electrode at an accelerated rate with the increasing rotation, the decrease in local alkalinity decreases the water reduction correspondingly. Hence, the pH regulation provided by the rotation during RRDE experiments subdues the rate of water reduction and carves the path for higher CO₂RR selectivity.

2.4. Conclusions and future work

In conclusion, we have developed here an online rotating ring disk electrode voltammetry method for the quantification of CO and H₂ formation during the course of CO₂RR. In this respect, Au acts as a model catalyst and in the future this technique can be employed for the fast screening of novel catalysts that are expected to make CO as the most significant product of electrocatalytic CO₂RR. Moreover, we show that by providing convection, the concentration of CO₂ at the interface is maintained to be equivalent to its concentration in the bulk and therefore, a stable rate for CO₂RR is achieved. Importantly, enhanced mass transport also acts as a local pH regulator because it mitigates the local buildup of OH⁻ ions formed in the vicinity of the electrode. This helps steering the Faradaic selectivity towards CO₂RR by suppressing water reduction to H₂. Interestingly, it is observed that water reduction on the Au surface, improves with increasing alkalinity. This further points to the fact that water reduction is the pre-dominant branch of HER that competes with CO₂RR in the usually employed 0.1M bicarbonate electrolytes. However, care should be exercised in extending the conclusions of the present study beyond the coinage metals, since the reaction mechanism (including the rate determining step and the product identity) can also have a profound impact on the observed trends for rotation rate dependence.

The inferences drawn from this work show that mass transport provides a flexible way for tuning the Faradaic efficiency towards CO₂RR in aqueous electrolytes. In this regard, future work will focus on elucidating the role of various electrolyte parameters (buffer strength, nature of anions and cations) for CO₂RR and HER kinetics under well-defined mass transport conditions. Moreover, additional experimental work will allow to formulate a comprehensive quantitative mass transport model which can provide more general insights on the role of local concentration gradients in CO₂RR/HER selectivity.

Acknowledgements

We gratefully acknowledge Dr. Emanuela Negro from Shell Global Solutions for the useful discussions on the development of the RRDE set-up. This work is part of the Advanced Research Center for Chemical Building Blocks (ARC CBBC) consortium, co-financed by the NWO and Shell Global Solutions B.V.

References

1. Seh, Z. F. W.; Kibsgaard, J.; Dickens, C. F.; Chorkendorff, I.; Nørskov, J. K.; Jaramillo, T. F., Combining theory and experiment in electrocatalysis: Insights into materials design. *Science* **2017**, *355* (6321).
2. Liu, X.; Xiao, J.; Peng, H.; Hong, X.; Chan, K.; Nørskov, J. K., Understanding trends in electrochemical carbon dioxide reduction rates. *Nature Communications* **2017**, *8*, 15438.
3. Wang, Y.; Liu, J.; Wang, Y.; Al-Enizi, A. M.; Zheng, G., Tuning of CO₂ Reduction Selectivity on Metal Electrocatalysts. *Small* **2017**, *13* (43), 1701809.
4. Cave, E. R.; Montoya, J. H.; Kuhl, K. P.; Abram, D. N.; Hatsukade, T.; Shi, C.; Hahn, C.; Nørskov, J. K.; Jaramillo, T. F., Electrochemical CO₂ reduction on Au surfaces: mechanistic aspects regarding the formation of major and minor products. *Physical Chemistry Chemical Physics* **2017**, *19* (24), 15856-15863.
5. Hori, Y.; Murata, A.; Kikuchi, K.; Suzuki, S., Electrochemical reduction of carbon dioxides to carbon monoxide at a gold electrode in aqueous potassium hydrogen carbonate. *Journal of the Chemical Society, Chemical Communications* **1987**, (10), 728-729.
6. Zhao, S.; Jin, R.; Jin, R., Opportunities and Challenges in CO₂ Reduction by Gold- and Silver-Based Electrocatalysts: From Bulk Metals to Nanoparticles and Atomically Precise Nanoclusters. *ACS Energy Letters* **2018**, *3* (2), 452-462.
7. Chen, Y.; Li, C. W.; Kanan, M. W., Aqueous CO₂ Reduction at Very Low Overpotential on Oxide-Derived Au Nanoparticles. *Journal of the American Chemical Society* **2012**, *134* (49), 19969-19972.
8. Feng, X.; Jiang, K.; Fan, S.; Kanan, M. W., Grain-Boundary-Dependent CO₂ Electroreduction Activity. *Journal of the American Chemical Society* **2015**, *137* (14), 4606-4609.
9. Hori, Y.; Takahashi, I.; Koga, O.; Hoshi, N., Electrochemical reduction of carbon dioxide at various series of copper single crystal electrodes. *Journal of Molecular Catalysis A: Chemical* **2003**, *199* (1), 39-47.
10. Todoroki, N.; Tei, H.; Tsurumaki, H.; Miyakawa, T.; Inoue, T.; Wadayama, T., Surface Atomic Arrangement Dependence of Electrochemical CO₂ Reduction on Gold: Online Electrochemical Mass Spectrometric Study on Low-Index Au(hkl) Surfaces. *ACS Catalysis* **2019**, 1383-1388.
11. Rosen, J.; Hutchings, G. S.; Lu, Q.; Rivera, S.; Zhou, Y.; Vlachos, D. G.; Jiao, F., Mechanistic Insights into the Electrochemical Reduction of CO₂ to CO on Nanostructured Ag Surfaces. *ACS Catalysis* **2015**, *5* (7), 4293-4299.
12. Zhang, X.-G.; Jin, X.; Wu, D.-Y.; Tian, Z.-Q., Selective Electrocatalytic Mechanism of CO₂ Reduction Reaction to CO on Silver Electrodes: A Unique Reaction Intermediate. *The Journal of Physical Chemistry C* **2018**, *122* (44), 25447-25455.
13. Dunwell, M.; Yang, X.; Setzler, B. P.; Anibal, J.; Yan, Y.; Xu, B., Examination of Near-Electrode Concentration Gradients and Kinetic Impacts on the Electrochemical Reduction of CO₂ using Surface-Enhanced Infrared Spectroscopy. *ACS Catalysis* **2018**, 3999-4008.

14. Mistry, H.; Behafarid, F.; Reske, R.; Varela, A. S.; Strasser, P.; Roldan Cuenya, B., Tuning Catalytic Selectivity at the Mesoscale via Interparticle Interactions. *ACS Catalysis* **2016**, *6* (2), 1075-1080.
15. Hall, A. S.; Yoon, Y.; Wuttig, A.; Surendranath, Y., Mesostructure-Induced Selectivity in CO₂ Reduction Catalysis. *Journal of the American Chemical Society* **2015**, *137* (47), 14834-14837.
16. Gupta, N.; Gattrell, M.; MacDougall, B., Calculation for the cathode surface concentrations in the electrochemical reduction of CO₂ in KHCO₃ solutions. *Journal of Applied Electrochemistry* **2006**, *36* (2), 161-172.
17. Kas, R.; Kortlever, R.; Yilmaz, H.; Koper, M. T. M.; Mul, G., Manipulating the Hydrocarbon Selectivity of Copper Nanoparticles in CO₂ Electroreduction by Process Conditions. *ChemElectroChem* **2015**, *2* (3), 354-358.
18. Wuttig, A.; Yoon, Y.; Ryu, J.; Surendranath, Y., Bicarbonate Is Not a General Acid in Au-Catalyzed CO₂ Electroreduction. *Journal of the American Chemical Society* **2017**, *139* (47), 17109-17113.
19. Jiang, X.; Cai, F.; Gao, D.; Dong, J.; Miao, S.; Wang, G.; Bao, X., Electrocatalytic reduction of carbon dioxide over reduced nanoporous zinc oxide. *Electrochemistry Communications* **2016**, *68* (Supplement C), 67-70.
20. Kas, R.; Hummadi, K. K.; Kortlever, R.; de Wit, P.; Milbrat, A.; Luiten-Olieman, M. W. J.; Benes, N. E.; Koper, M. T. M.; Mul, G., Three-dimensional porous hollow fibre copper electrodes for efficient and high-rate electrochemical carbon dioxide reduction. *Nature Communications* **2016**, *7*, 10748.
21. Luo, W.; Zhang, J.; Li, M.; Züttel, A., Boosting CO Production in Electrocatalytic CO₂ Reduction on Highly Porous Zn Catalysts. *ACS Catalysis* **2019**, *9* (5), 3783-3791.
22. Yoon, Y.; Hall, A. S.; Surendranath, Y., Tuning of Silver Catalyst Mesostructure Promotes Selective Carbon Dioxide Conversion into Fuels. *Angewandte Chemie International Edition* **2016**, *55* (49), 15282-15286.
23. Chen, C.; Zhang, B.; Zhong, J.; Cheng, Z., Selective electrochemical CO₂ reduction over highly porous gold films. *Journal of Materials Chemistry A* **2017**, *5* (41), 21955-21964.
24. Schulz, K. G.; Riebesell, U.; Rost, B.; Thoms, S.; Zeebe, R. E., Determination of the rate constants for the carbon dioxide to bicarbonate interconversion in pH-buffered seawater systems. *Marine Chemistry* **2006**, *100* (1), 53-65.
25. Clark, E. L.; Resasco, J.; Landers, A.; Lin, J.; Chung, L.-T.; Walton, A.; Hahn, C.; Jaramillo, T. F.; Bell, A. T., Standards and Protocols for Data Acquisition and Reporting for Studies of the Electrochemical Reduction of Carbon Dioxide. *ACS Catalysis* **2018**, *8* (7), 6560-6570.
26. Clark, E. L.; Bell, A. T., Direct Observation of the Local Reaction Environment during the Electrochemical Reduction of CO₂. *Journal of the American Chemical Society* **2018**, *140* (22), 7012-7020.
27. Hori, Y.; Kikuchi, K.; Suzuki, S., Production of CO and CH₄ in electrochemical reduction of CO₂ at metal electrodes in aqueous hydrogencarbonate solution. *Chemistry Letters* **1985**, *14*, 1695-1698.
28. Dunwell, M.; Lu, Q.; Heyes, J. M.; Rosen, J.; Chen, J. G.; Yan, Y.; Jiao, F.; Xu, B., The Central Role of Bicarbonate in the Electrochemical Reduction of Carbon Dioxide on Gold. *Journal of the American Chemical Society* **2017**, *139* (10), 3774-3783.
29. Feaster, J. T.; Shi, C.; Cave, E. R.; Hatsukade, T.; Abram, D. N.; Kuhl, K. P.; Hahn, C.; Nørskov, J. K.; Jaramillo, T. F., Understanding Selectivity for the

Electrochemical Reduction of Carbon Dioxide to Formic Acid and Carbon Monoxide on Metal Electrodes. *ACS Catalysis* **2017**, 7 (7), 4822-4827.

30. Zhang, B. A.; Ozel, T.; Elias, J. S.; Costentin, C.; Nocera, D. G., Interplay of Homogeneous Reactions, Mass Transport, and Kinetics in Determining Selectivity of the Reduction of CO₂ on Gold Electrodes. *ACS Central Science* **2019**, 5 (6), 1097-1105.

31. Singh, M. R.; Goodpaster, J. D.; Weber, A. Z.; Head-Gordon, M.; Bell, A. T., Mechanistic insights into electrochemical reduction of CO(2) over Ag using density functional theory and transport models. *Proc Natl Acad Sci U S A* **2017**, 114 (42), E8812-E8821.

32. Wadas, A.; Rutkowska, I. A.; Bartel, M.; Zoladek, S.; Rajeshwar, K.; Kulesza, P. J., Rotating ring-disk voltammetry: Diagnosis of catalytic activity of metallic copper catalysts toward CO₂ electroreduction. *Russian Journal of Electrochemistry* **2017**, 53 (10), 1194-1203.

33. Zhang, J.; Pietro, W. J.; Lever, A. B. P., Rotating ring-disk electrode analysis of CO₂ reduction electrocatalyzed by a cobalt tetramethylpyridoporphyrazine on the disk and detected as CO on a platinum ring. *Journal of Electroanalytical Chemistry* **1996**, 403 (1), 93-100.

34. Lates, V.; Falch, A.; Jordaan, A.; Peach, R.; Kriek, R. J., An electrochemical study of carbon dioxide electroreduction on gold-based nanoparticle catalysts. *Electrochimica Acta* **2014**, 128, 75-84.

35. Duan, Z.; Henkelman, G., Calculations of the pH-Dependent Onset Potential for CO Electrooxidation on Au(111). *Langmuir* **2018**, 34 (50), 15268-15275.

36. Blizanac, B. B.; Arenz, M.; Ross, P. N.; Marković, N. M., Surface Electrochemistry of CO on Reconstructed Gold Single Crystal Surfaces Studied by Infrared Reflection Absorption Spectroscopy and Rotating Disk Electrode. *Journal of the American Chemical Society* **2004**, 126 (32), 10130-10141.

37. Rodriguez, P.; Garcia-Araez, N.; Koverga, A.; Frank, S.; Koper, M. T. M., CO Electrooxidation on Gold in Alkaline Media: A Combined Electrochemical, Spectroscopic, and DFT Study. *Langmuir* **2010**, 26 (14), 12425-12432.

38. Lin, A. S.; Lin, J.; Huang, J. C., Electrochemical oxidation of dissolved carbon monoxide on gold electrode in alkaline medium. *Gold Bulletin* **2007**, 40 (1), 82-85.

39. Łukaszewski, M.; Soszko, M.; Czerwiński, A., Electrochemical Methods of Real Surface Area Determination of Noble Metal Electrodes – an Overview. *International Journal of Electrochemical Science* **2016**, 11, 4442-4469.

40. Vos, J. G.; Koper, M. T. M., Examination and prevention of ring collection failure during gas-evolving reactions on a rotating ring-disk electrode. *Journal of Electroanalytical Chemistry* **2019**, 850, 113363.

41. Alzahrani, H. A. H.; Buckingham, M. A.; Marken, F.; Aldous, L., Success and failure in the incorporation of gold nanoparticles inside ferri/ferrocyanide thermogalvanic cells. *Electrochemistry Communications* **2019**, 102, 41-45.

42. Rodriguez, P.; Garcia-Araez, N.; Koper, M. T. M., Self-promotion mechanism for CO electrooxidation on gold. *Physical Chemistry Chemical Physics* **2010**, 12 (32), 9373-9380.

43. Vos, J. G.; Wezendonk, T. A.; Jeremiassi, A. W.; Koper, M. T. M., MnO(x)/IrO(x) as Selective Oxygen Evolution Electrocatalyst in Acidic Chloride Solution. *Journal of the American Chemical Society* **2018**, 140 (32), 10270-10281.

44. Bard, A. J.; Faulkner, L. R., *Electrochemical methods : fundamentals and applications* Wiley: New York, **1980**.

45. Wuttig, A.; Yaguchi, M.; Motobayashi, K.; Osawa, M.; Surendranath, Y., Inhibited proton transfer enhances Au-catalyzed CO₂-to-fuels selectivity. *Proceedings of the National Academy of Sciences* **2016**, *113* (32), E4585-E4593.
46. Ooka, H.; Figueiredo, M. C.; Koper, M. T. M., Competition between Hydrogen Evolution and Carbon Dioxide Reduction on Copper Electrodes in Mildly Acidic Media. *Langmuir* **2017**, *33* (37), 9307-9313.
47. Hori, Y.; Murata, A.; Takahashi, R., Formation of hydrocarbons in the electrochemical reduction of carbon dioxide at a copper electrode in aqueous solution. *Journal of the Chemical Society, Faraday Transactions 1: Physical Chemistry in Condensed Phases* **1989**, *85* (8), 2309-2326.
48. Zhong, H.; Fujii, K.; Nakano, Y.; Jin, F., Effect of CO₂ Bubbling into Aqueous Solutions Used for Electrochemical Reduction of CO₂ for Energy Conversion and Storage. *The Journal of Physical Chemistry C* **2015**, *119* (1), 55-61.
49. Ohmori, T.; Enyo, M., Hydrogen evolution reaction on gold electrode in alkaline solutions. *Electrochimica Acta* **1992**, *37* (11), 2021-2028.
50. Sasaki, T.; Matsuda, A., Mechanism of hydrogen evolution reaction on gold in aqueous sulfuric acid and sodium hydroxide. *Journal of the research institute for catalysis Hokkaido university* **1982**, *29* (3), 113-132.
51. Pentland, N.; Bockris, J. O. M.; Sheldon, E., Hydrogen Evolution Reaction on Copper, Gold, Molybdenum, Palladium, Rhodium, and Iron: Mechanism and Measurement Technique under High Purity Conditions. *Journal of The Electrochemical Society* **1957**, *104* (3), 182-194.
52. Resasco, J.; Lum, Y.; Clark, E.; Zeledon, J. Z.; Bell, A. T., Effects of Anion Identity and Concentration on Electrochemical Reduction of CO₂. *ChemElectroChem* **2018**, *5* (7), 1064-1072.
53. Birdja, Y. Y.; Pérez-Gallent, E.; Figueiredo, M. C.; Göttle, A. J.; Calle-Vallejo, F.; Koper, M. T. M., Advances and challenges in understanding the electrocatalytic conversion of carbon dioxide to fuels. *Nature Energy* **2019**, *4* (9), 732-745.
54. Xue, S.; Garlyyev, B.; Watzele, S.; Liang, Y.; Fichtner, J.; Pohl, M. D.; Bandarenka, A. S., Influence of Alkali Metal Cations on the Hydrogen Evolution Reaction Activity of Pt, Ir, Au, and Ag Electrodes in Alkaline Electrolytes. *ChemElectroChem* **2018**, *5* (17), 2326-2329.



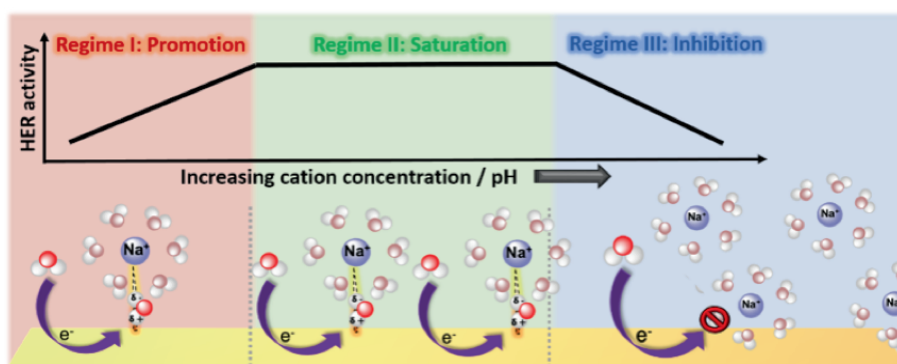
Chapter 3

The interrelated effect of cations and electrolyte pH on the hydrogen evolution reaction on gold electrodes in alkaline media



Abstract

In this work we study the role of alkali metal cation concentration and electrolyte pH in altering the kinetics of hydrogen evolution reaction (HER) at gold (Au) electrodes. We show that at moderately alkaline pH (pH = 11), increasing cation concentration significantly enhances the HER activity on Au electrodes (with a reaction order ~ 0.5). Based on these results we suggest that cations play a central role in stabilizing the transition state of the rate-determining Volmer step by favorably interacting with the dissociating water molecule ($*\text{H}-\text{OH}^{\delta-}-\text{cat}^+$). Moreover, we show that increasing electrolyte pH (pH 10 to pH 13) tunes the local field strength which in turn indirectly enhances the activity of HER by tuning the near-surface cation concentration. Interestingly, a too high near-surface cation concentration (at high pH and high cation concentration) leads to a lowering of the HER activity, which we ascribe to a blockage of the surface by near-surface cations.



This chapter is based on the article:

Goyal, A.; Koper, M. T. M., The Interrelated Effect of Cations and Electrolyte pH on the Hydrogen Evolution Reaction on Gold Electrodes in Alkaline Media. *Angewandte Chemie International Edition* **2021**, 60 (24), 13452-1346

3.1. Introduction

Research on the electrochemical hydrogen evolution reaction (HER) is at the heart of realizing a sustainable and economically feasible hydrogen-based economy. Additionally, this “simple” two-electron transfer reaction serves as a test ground for the laws of electrocatalysis and therefore continues to be of utmost importance, both in fundamental electrochemistry and for application purposes. However, the rigorous experimental and theoretical studies that have been undertaken to discern the activity descriptors governing the kinetics of HER at acidic pH ($2\text{H}^+ + 2\text{e}^- \rightarrow \text{H}_2$; proton reduction),^{1, 2-3} cannot satisfactorily explain the activity trends that have been observed at alkaline pH ($2\text{H}_2\text{O} + 2\text{e}^- \rightarrow \text{H}_2 + 2\text{OH}^-$; water reduction).⁴⁻⁶ This gap in the understanding of HER in alkaline media is a major hindrance in the optimization of alkaline water electrolyzers, which can in principle be more cost efficient than the acidic Proton Exchange Membrane electrolyzers.⁷⁻⁸

The major caveat in the present understanding of HER in alkaline media arises from two main factors, (1) lack of systematic studies on surfaces other than Pt in a broad pH window,⁹⁻¹⁰ and (2) sole focus on the hydrogen adsorbed on the metal surface (H_{upd} and H_{opd}) as the key descriptor for HER.¹¹⁻¹⁴ Platinum is considered the best metal for HER since it catalyzes HER at negligible overpotential (in acidic media), owing to its optimal hydrogen binding energy ($\Delta G_{\text{H,adsorption}} \approx 0$). The large variations in the rate of HER (up to few orders of magnitude) on different electrode materials have been typically correlated to the variations in the free energy of hydrogen adsorption on these catalysts.^{1, 12-13} It is reasonable to assume that these activity trends would also hold in alkaline pH. However, there is ample experimental evidence that catalysts that bind hydrogen less optimally than Pt (such as Pt-Ru alloys, Ir and 3d metal hydroxide, chalcogenide and phosphide modified electrodes) show superior catalytic activity in alkaline media.¹⁵⁻¹⁸ Additionally, the loss in the activity of HER on the different crystal facets of Pt in going from acidic pH to alkaline pH, cannot be explained satisfactorily by the changes in the hydrogen binding energy (HBE) either. Yan and co-workers have suggested that the sluggish kinetics of HER in alkaline media can be attributed to the increasing HBE with increasing pH, as derived from the positive shift of the underpotential hydrogen (H_{upd}) peak in the blank voltammetry.¹¹ However, it has been shown that the positive shift in the H_{upd} peak arises from the weakening of the OH adsorption on Pt(100) and Pt(110) sites due to the presence of alkali metal cations near the interface, and that there is no direct relation to changes in the HBE.¹⁹⁻²⁰ Moreover, unlike Pt(100) and Pt(110), Pt(111) does not show changes in the experimentally observed HBE with a change in electrolyte pH, however it still shows a drastic drop in the HER activity as the electrolyte pH is increased.²¹ These apparently conflicting trends point to a fundamentally different nature of HER in alkaline media, where the dissociation of water at the metal interface can introduce an additional energy barrier for the reaction and therefore, the overall reaction rate can depend on additional factors, such as the interaction of water and its dissociation products with the (electro-)chemical environment at the metal-

electrolyte interface. Recently, our group has shown that reorganization of interfacial water may be an important descriptor for the activity of HER in alkaline media on Pt(111), which can be modified indirectly via the electrolyte pH and/or by the clusters of Ni(OH)₂ at the surface through their influence on the potential of zero charge and the resulting interfacial electric field. These results showed that the interfacial electric field affects the structure of the water network at the interface which in turn controls the HER kinetics in alkaline media.²¹ Nevertheless, in order to arrive at a clear molecular picture of what dictates the activity of HER in alkaline media, it is vital to also probe the short-range interactions that can affect the metal-water interface locally.

In this regard, the non-covalent interactions between the water molecules and alkali metal cations have been shown to play a significant role in determining the HER activity by locally interacting with the reactants/products of HER. Most notably, Markovic and co-workers have probed the promotional role of Li⁺ ions in improving the HER activity in alkaline media^{15, 22}. More recently, Grimaud and co-workers have shown that these effects are also operational in organic electrolytes.²³ In general, these studies attribute the promotion of the electrochemical water dissociation step to favorable cation-water interactions. However, various discrepancies still exist in the current literature since the HER activity has been observed to decrease from Li⁺ to Cs⁺ on the different facets of Pt and Ir, while the opposite trend has been observed on Au and Ag.²⁴ The trend on Pt and Ir is in good agreement with the previous works of Markovic and co-workers, however, the discriminant behavior of the alkali metal cations on the transition metal electrodes (Pt, Ir and Rh) and the coinage metal electrodes (Au and Ag) indicates that a wide range of electrode-electrolyte combinations needs to be probed in order to completely understand the role of metal-adsorbate interactions in the kinetics of HER in alkaline media.

In this work, we address these issues by systematically studying HER in alkaline media on Au electrodes. We will show that the HER activity on polycrystalline Au and Au(111) surfaces is enhanced significantly with the increasing alkali metal cation concentration in the electrolyte, but only in a limited pH region around pH 11. We propose that the cations near the interface interact favorably with the transition state of the rate-determining Volmer step by stabilizing the (partially) negative hydroxide which is being split off from the reacting water molecule (*H--OH^{δ-}--cat⁺). Remarkably, at higher pH, the effect of the concentration of alkali cations is diminished, and it is even negative at pH=13. Furthermore, capacitance curves obtained from impedance spectroscopy suggest that the electrolyte pH also influences the near surface composition of the electrolyte such that an increasing electrolyte pH leads to a corresponding increase in the near-surface cation concentration. This results in an apparent pH dependence for the HER activity on the Au electrodes where similar to the cation concentration effect, saturation is observed at extreme pH values (pH 13 to pH 14). We attribute the saturation and inhibitive effects observed at high pH and at high cation concentration to a blockage of the surface by cations when they reach a threshold concentration.

This work shows that the electrolyte pH and the near-surface cation concentration are inter-dependent parameters, which cannot be easily decoupled in alkaline media. Hence, our work provides foundational insights on the complex molecular origin of the pH dependence of HER, and we believe that these insights will be instrumental in guiding further fundamental work and eventually the design of optimized catalyst-electrolyte conditions for HER in alkaline media.

3.2. Experimental section

3.2.1. Chemicals

The electrolytes were prepared from H₂SO₄ (98% by wt. solution, EMSURE, Merck), HClO₄ (60% by wt. solution), NaClO₄ (99.99%, trace metals basis, Sigma-Aldrich), NaOH (32% by wt. solution, analysis grade, Merck) and Ultrapure water (MilliQ gradient, ≥ 18.2 M Ω cm, TOC < 5 ppb). Ar (6.0 purity, Linde) and H₂ (5.0 purity, Linde) were used for purging the electrolytes. To prepare the roughened Au electrodes for *in situ* Raman studies, KAu(CN)₂ (99.95 %, trace metals basis, Sigma-Aldrich), KAg(CN)₂ (Sigma-Aldrich), Na₂CO₃ ($\geq 99.5\%$, Sigma-Aldrich) and HClO₄ (60% by wt. solution, EMSURE, Merck) were used.

3.2.2. General electrochemical methods

The electrochemical measurements at pH 10 to pH 12 were carried out in home-made borosilicate glass cells and measurements at pH 13 were carried out in a home-made PTFE cell. The reference electrode was separated from the working compartment with the help of a Luggin capillary and the counter electrode was a Au wire (99.99% purity), unless otherwise stated. The glassware was cleaned prior to each experiment by boiling it five times in ultrapure water. When not in use, the glassware was stored in 1 g/L solution of KMnO₄ (acidified). Before boiling, any traces of KMnO₄ and MnO₂ were removed from the glassware by submerging it in a diluted solution of acidified H₂O₂ (few drops of conc. H₂SO₄ and 10-15 mL H₂O₂ in excess water) for half an hour. Before every experiment, the electrolytes were purged for ca. 20 minutes with Ar to remove any dissolved oxygen from the electrolyte. Moreover, during the measurement, Ar was also bubbled over the headspace of the electrochemical cell, in order to eliminate any interference from the ambient oxygen. A home-made reversible hydrogen electrode (RHE) or a Ag/AgCl reference (Pine research instrumentation, sat. NaCl, $E = 0.197$ V vs standard hydrogen electrode) were used as the reference electrode in all the experiments. All the electrochemical measurements were carried out using a Biologic (VSP-300) potentiostat and a MSR rotator (Pine Research). For all the CVs taken, 85% Ohmic drop compensation was performed and for all the steady-state potentiostatic measurements 100% Ohmic drop compensation was applied. The Ohmic drop of the electrolyte was determined by carrying out electrochemical impedance spectroscopy (EIS) at 0.05 V (vs RHE; double-layer region). All the measurements with Au polycrystalline were performed with E6/E5 ChangeDisk tips in a PEEK shroud (Pine Research) and all the

measurements with Au(111) were performed with a home-made PEEK shroud compatible with the MSR rotator.

For the pre-electrolysis studies, a home-made PTFE cell was used in which overnight (16 hrs.) chronopotentiometry was performed in 0.1 M NaOH electrolyte at a constant current of -1 mA and polycrystalline Pt wires were used, both as the counter and as the working electrode. Thereafter, the electrodes were removed from the electrolyte under potential control. The results from the pre-electrolysis studies are shown in Figure S7 (Appendix B).

3.2.3. Working electrode preparation

Au Polycrystalline: Before each experiment, the Au polycrystalline disk (diameter = 5mm, Pine instruments) was mechanically polished on Buehler micro-polishing cloth (8 inches) with decreasing sizes of diamond polishing suspension, namely, 3 μ m, 1 μ m and 0.25 μ m. Next, the disk was sonicated in ultrapure water and acetone for 10 minutes to remove any organic/inorganic impurities, and mounted on the RDE tip. Thereafter, the Au polycrystalline disk was electrochemically polished in 0.1 M H₂SO₄ (0.05 V to 1.75 V vs RHE, 200 cycles at a scan rate of 1 V s⁻¹) by going to the Au oxide formation and reduction region.²⁵ Prior to each experiment, a characterization cyclic voltammetry (CV) of the disk was obtained in the same potential window where the electrochemical polishing was performed (at a scan rate of 50 mV s⁻¹), as shown in Figure S1 (Appendix B). For calculating the current densities in the HER activity the electrochemically active surface area (ECSA) of the disk was determined by calculating the charge from the reduction peak for the Au oxide in the characterization CV and dividing it by the specific charge of one monolayer of Au (390 μ C cm⁻²).²⁵ The working electrode was then used for the electrochemical measurements.

Au(111): Before each experiment, the Au(111) disk (diameter = 7mm) was prepared by performing multiple cycles (\approx 10) of flame annealing (ca. 1 min) and quenching (MilliQ water).²⁶ Thereafter, it was transferred to the electrochemical cell with a protective layer of MilliQ water. The quality of the single crystal preparation was ascertained by checking its double layer features in 0.1 M H₂SO₄ (0.1 V to 1.15 V vs RHE), as shown in Figure S1 (Appendix B). For calculating the current densities in the HER activity experiments, the geometric surface area of the crystal (0.38 cm²) was used.

3.2.4. Electrochemical measurements for HER activity

Table 1 Compositions of the electrolytes employed for the pH dependence studies of HER

Bulk pH	[HClO ₄] / M	[NaOH] / M	[NaClO ₄] / M	Total ion concentration / M
1	10 ⁻¹	—	—	2 \times 10 ⁻¹
2	10 ⁻²	—	9 \times 10 ⁻²	2 \times 10 ⁻¹
3	10 ⁻³	—	9.9 \times 10 ⁻²	2 \times 10 ⁻¹
7	—	—	10 ⁻¹	2 \times 10 ⁻¹

10	—	10^{-4}	9.99×10^{-2}	2×10^{-1}
11	—	10^{-3}	9.9×10^{-2}	2×10^{-1}
12	—	10^{-2}	9×10^{-2}	2×10^{-1}
13	—	10^{-1}	—	2×10^{-1}
14	—	10^0	—	2×10^0

All the studies for the pH dependence of HER were done in Ar sat. 0.1 M electrolytes (except pH =14), as shown Table 1. The CVs were taken in the potential window of 0 V to -0.65 V vs RHE at a scan rate of 25 mVs^{-1} and the working electrode was rotated at 2500 rpm in every measurement. Additionally, to obtain the Tafel data, chronoamperometry was performed in the potential window of the CVs at 50 mV potential steps while rotating the electrode (2500 rpm). Generally, 20 seconds per potential step were enough to reach the steady-state. EIS measurements were performed at different pH values (pH 10 to pH 13) with Au(111) in two potential windows, the double layer region (0.1 V to 0.6 V vs RHE) and the near HER region (0 V to -0.3 V vs RHE), with frequencies ranging from 30 KHz to 1 Hz and a peak to peak amplitude of 5 mV. Moreover, a $10 \mu\text{F}$ shunt capacitor bridge was added between a secondary counter electrode (Au wire) and the reference electrode in order to eliminate any artefacts caused by the non-ideal behavior of the potentiostat at high frequencies. The impedance data was fit with the help of EIS Zfit (part of Biologic's EC-Lab software) by using the equivalent electric circuit shown in Figure 5a. The typical EIS plots (and fits) obtained during the experiments are shown in Figure S9, S10 and S11 (Appendix B).

All the studies for the bulk cation concentration dependence of HER were done at pH 11 (10^{-3} M NaOH), pH 12 (10^{-2} M NaOH) and pH 13 (0.1 M NaOH) where the cation concentration was varied in the electrolyte by adjusting the concentration of NaClO_4 , as shown in Table 2. The CVs were taken in the potential window of 0 V to -0.65 V vs RHE at a scan rate of 25 mVs^{-1} and the working electrode was rotated at 2500 rpm in every measurement. Additionally, to obtain the Tafel data, chronoamperometry was performed in the potential window of the CVs at 50 mV potential steps while rotating the electrode (2500 rpm). Generally, 20 seconds per potential step were enough to reach the steady-state. Impedance measurements were also performed in the double-layer region (0.1 V to 0.6 V vs RHE) and the near HER region (0 V to -0.3 V vs RHE) at 2 different concentrations of NaClO_4 , namely 5 mM and 50 mM and different electrolyte pH values (pH 10 to pH 12). The parameters of the EIS measurements were same as above.

Table 2 Compositions of the electrolytes employed for the cation concentration dependence studies of HER

Bulk pH	[NaOH] / M	[NaClO ₄] / M	Total ion concentration / M
11	10^{-3}	5×10^{-3}	1.2×10^{-2}
		5×10^{-2}	1.02×10^{-1}
		2.5×10^{-1}	5.02×10^{-1}

12	10^{-2}	5×10^{-1}	$\approx 10^0$
		10^0	2×10^0
		5×10^{-3}	3×10^{-2}
		5×10^{-2}	1.2×10^{-1}
		2.5×10^{-1}	5.2×10^{-1}
		5×10^{-1}	1.02×10^0
13	10^{-1}	10^0	2.02×10^0
		5×10^{-3}	2.1×10^{-1}
		5×10^{-2}	3×10^{-1}
		2.5×10^{-1}	7×10^{-1}
		5×10^{-1}	1.2×10^0
		10^0	2.2×10^0

3.2.5. *In situ* surface enhanced Raman Spectroscopy measurements

In situ surface enhanced Raman spectroscopy (SERS) measurements were performed with a LabRam HR800 (Horiba Jobin Yvon) confocal microscope, which featured a HeNe laser (632.81 nm) where the laser beam was introduced through an objective lens to the roughened Au electrode in a vertical arrangement.²⁷ In order to avoid beam damage the laser beam was attenuated by a factor of 10 resulting in a measured beam energy at the location of the Raman cell of 0.28 W. The measurements were performed with electrolytes of different pH (pH 10 to pH 13) with a fixed total ion concentration (0.2 M; refer to Table 1) where the spectra were recorded in the potential window of 0.2 V to -0.6 V (vs RHE and vs NHE) at 200 mV potential steps. It was not possible to go more negative than -0.6 V (vs RHE) because beyond these potentials, the hydrogen bubbles attached to the surface disturbed the vertical spatial resolution in the optical window. The polycrystalline Au electrode was prepared for the SERS studies by electrochemically depositing roughened nano-porous Au channels at the flat Au electrode by following the procedure outlined by Searson and co-workers and Eich and co-workers.²⁸⁻²⁹ Briefly, a binary alloy solution of Ag₈₀Au₂₀ was prepared with KAg(CN)₂ and KAu(CN)₂ in 0.25 M Na₂CO₃ buffer solution and it was electrochemically deposited onto the Au substrate electrode at -1.2 V (vs Ag/AgCl) for 7 min. Thereafter, Ag was de-alloyed from the film by electrochemically cycling (20 cycles) the electrode in a 1 M HClO₄ solution between 1.05 V to 1.2 V (vs Ag/AgCl) at 5mVs⁻¹. Thereafter, the electrode was ready for the SERS measurements.

3.3. Results

3.3.1. Role of cations in the HER kinetics in alkaline media

First, we examine the effect of cation concentration on the kinetics of HER, for constant values of the electrolyte pH. In Figure 1a and 1b we show that at moderately alkaline electrolyte pH (pH 11), the HER activity increases significantly with increasing Na⁺ cation concentration in the electrolyte, both on polycrystalline Au and Au(111) surfaces. These experiments illustrate that on a Au electrode, at pH=11, increasing the (near-surface)

concentration of the cations positively affects the kinetics of HER in the alkaline media. Interestingly, measurements at higher pH (shown in Figure 2) show that HER reaction orders in cation concentration are pH dependent. The HER reaction order in cation concentration is around 0.5 at pH 11 (shown in Figure 2a and 2b), around 0 at pH 12 (shown in Figure 2c and 2d), whereas at pH 13 negative reaction orders are obtained (shown in Figure 2e and 2f). We note that for isolated data points in Fig.1 (especially pH=11 and 5 mM NaClO₄), we cannot neglect the possible contribution of OH⁻ migration to the measured current. However, this effect can be safely neglected for the higher concentrations of NaClO₄, and therefore there is no significant effect of OH⁻ migration on the derived reaction orders. The pH dependence of the (fractional) reaction orders suggests that the cation induced alteration in the rate limiting step affects a species which is adsorbed at the electrified interface. The Tafel slope of ~120 mV/dec in the low overpotential range (see Figure S2 in Appendix B) further indicates that the first electron transfer step ($\text{H}_2\text{O} + \text{e}^- + * \rightarrow \text{H}-* + \text{OH}^-$; Volmer step) is rate determining.³⁰ In this scenario, fractional reaction orders at pH 11 correspond to a regime with intermediate cation concentration in the double layer which will in-turn lead to an intermediate coverage of the activated water molecule at the interface.

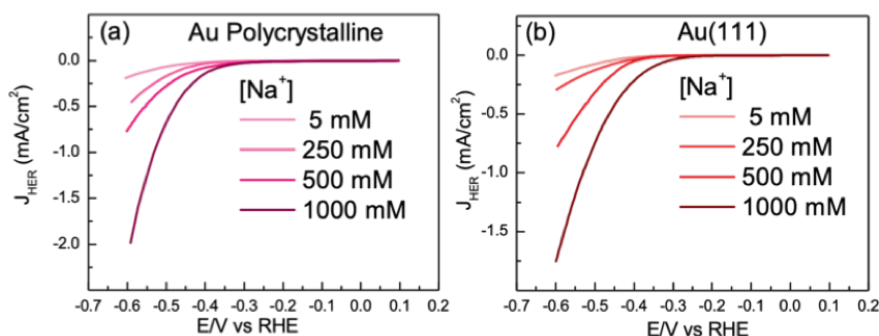


Figure 1 Cyclic voltammograms obtained for HER on (a) Au polycrystalline surface and (b) Au(111) surface at 2500 rpm in 0.001 M NaOH (pH 11) for different concentrations of NaClO₄ (5 mM, 250 mM, 500 mM and 1000 mM) in Ar sat. environment at 25 mVs⁻¹.

The near zero reaction orders obtained at pH 12 indicate that, in addition to the bulk cation concentration, the electrolyte pH also affects the near-surface concentration of cations. A pH dependent cation concentration near the interface can be rationalized based on the fact that the potential of zero charge (E_{pzc}) shifts positively with the increasing electrolyte pH ($E_{pzc} = E_{pzc}^0 + 0.059\text{pH}$; $E_{pzc} = 1.12 \text{ V/RHE}$ at pH 11), thus resulting in a quite negative interfacial electric field ($\Delta E = E - E_{pzc}$) under the conditions used in these measurements.³¹⁻³³ Hence, it can be expected that at these moderately alkaline conditions the near surface cation concentration starts to approach saturation.

Interestingly, a closer look at the effect of the cation concentration changes at pH 12 (see Figures 2c and d and Figure S3 in Appendix B) reveals that while an initial increase in the cation concentration shows a small positive

effect on the activity of HER, at higher concentrations, a slight drop in the HER activity is observed. Furthermore, at pH 13 the increasing cation concentration exhibits an entirely inhibitive effect on HER activity (see Figures 2e and f and Figure S3 in Appendix B). These results show that above a certain threshold concentration, the promotional effect of the cations first plateaus and then inhibits the kinetics of HER.

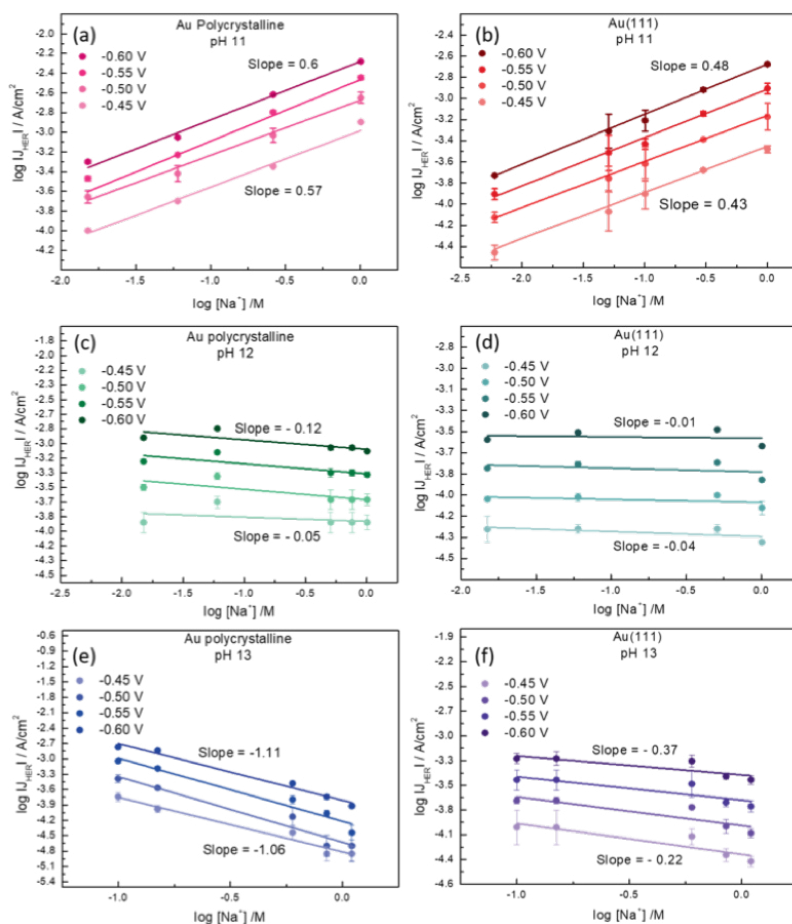


Figure 2 Reaction order plot of HER in the cation concentration at pH 11 on (a) Au polycrystalline and (d) Au(111), at pH 12 on (b) Au polycrystalline and (e) Au(111) and at pH 13 on (c) Au Polycrystalline and (f) Au(111), at 50 mV potential steps (vs RHE) plotted as a function of the logarithm of the current density on the y-axis and logarithm of the $[Na^+]$ concentration on the x-axis. The corresponding slopes (reaction orders) are indicated next to the plots, where the slope at the bottom corresponds to the applied potential of -0.45 V (vs RHE) and the slope at the top corresponds to the applied potential of -0.60 V (vs RHE) in all the graphs.

Here, the pH dependence of HER reaction orders in cation concentration would signify a correlation between the electrolyte pH and the near-surface cation concentration. In the next section we elucidate these effects further by studying the role of electrolyte pH in tuning the kinetics of HER for a constant value of bulk cation concentration.

3.3.2. HER kinetics in alkaline media as a function of the bulk pH

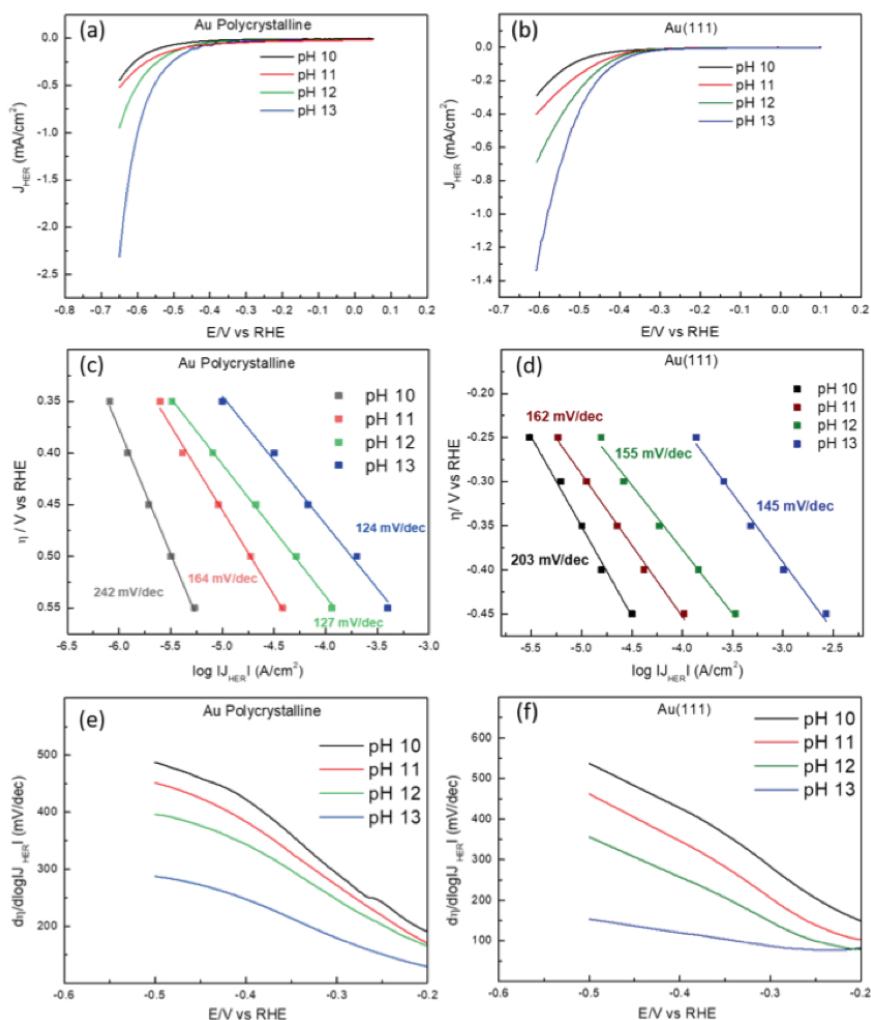


Figure 3 Cyclic voltammograms obtained for HER on (a) Au polycrystalline surface and (b) Au(111) surface at 2500 rpm in 0.1 M NaOH (pH 13), 0.01 M NaOH + 0.09 M NaClO₄ (pH 12), 0.001 M NaOH + 0.099 M NaClO₄ (pH 11) and 0.0001 M NaOH + 0.0999 M NaClO₄ (pH 10), in Ar sat. environment at 25 mVs⁻¹. Steady-state current obtained at 50 mV potential steps at 2500 rpm on (c) Au polycrystalline surface and (d) Au(111) surface at different pH values (same as above), plotted as function of the applied overpotential on the y-axis and the logarithm of the current density on the x-axis where the corresponding Tafel slopes at each pH value are indicated next to the plot. Tafel slopes obtained from the differentiation of the cyclic voltammograms in (a) and (b) plotted as a function of the applied potential (vs RHE) for (e) Au polycrystalline and (f) Au (111) at different pH values.

In Figures 3a and 3b we show that both polycrystalline Au and Au(111) exhibit an increase in the HER activity on the RHE scale with increasing electrolyte pH, at a constant concentration of cations (0.1 M) in the bulk. Moreover, chronoamperometry measurements in Figures 3c and 3d show that the steady-state currents for the HER also increase with the increasing

pH. The Tafel slopes thus obtained decrease with the increasing pH, confirming that the increasing electrolyte pH enhances the potential dependence of the HER reaction on Au electrodes. Additionally, in Figures 3e and 3f we plot the Tafel slopes, as derived from the cyclic voltammograms, as a function of the applied potential, confirming the trend of the steady-state chronoamperometry: Tafel slopes of around 120 mV/dec are obtained at low overpotentials for all the pH values and they increase with lower pH.

The pH dependence of the HER kinetics is interesting because thermodynamically, the onset for HER is expected to remain constant on the pH dependent RHE scale ($E_{\text{RHE}} = E_{\text{NHE}} + 0.059\text{pH}$), because for a given potential on the RHE scale, the thermodynamic driving force is the same, regardless of pH.

However, if the Volmer step is indeed rate limiting (as indicated by the Tafel slopes), the kinetics for this reaction should not depend on the electrolyte pH because no proton or hydroxide is involved in the reactant side of the rate limiting reaction equation ($\text{H}_2\text{O} + \text{e}^- + * \rightarrow \text{H}-* + \text{OH}^-$), implying that the rate should be constant on the pH independent NHE (Normal Hydrogen Electrode) reference scale. Figure 4 shows the data of Figures 3a and 3b on the NHE scale. Remarkably, there is also a pH dependence of the kinetics of HER under alkaline conditions on the NHE scale: the HER kinetics become slower with increasing pH, in contrast to the situation on the RHE scale, where the reaction becomes faster. Since the (bulk) cation concentration is constant in these measurements, this result appears to imply an intrinsic pH dependence of the HER on Au.

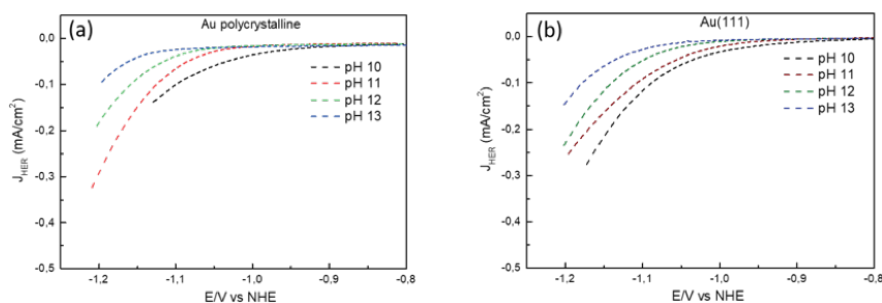


Figure 4 Cyclic voltammograms for HER plotted on the NHE scale for (a) Au polycrystalline surface and (b) Au(111) surface at 2500 rpm in 0.1 M NaOH (pH 13), 0.01 M NaOH + 0.09 M NaClO₄ (pH 12), 0.001 M NaOH + 0.099 M NaClO₄ (pH 11) and 0.0001 M NaOH + 0.0999 M NaClO₄ (pH 10), in Ar sat. environment at 25 mVs⁻¹ where the data has been obtained from Figures 3a and b respectively, by converting the potentials from the RHE scale to the NHE scale ($E_{\text{NHE}} = E_{\text{RHE}} - 0.059\text{pH}$).

The enhancement in the HER kinetics with the increasing electrolyte pH (on the RHE scale) agrees with the observed pH dependence of cation concentration effects. Together, these results indicate that the increasing electrolyte pH leads to an increase in the near-surface concentration of cations which positively affects the HER kinetics on the RHE scale. Remarkably, the near saturation effects are also captured for the reaction order of HER in the bulk electrolyte pH, as shown in Figures 5a and 5b where the reaction order on the bulk pH decreases from around 0.2 to 0 in going

from pH 7 to pH 14. Similar trends in the experimental reaction orders for the cation concentration and the electrolyte pH suggest that these two parameters are tuning the same active species at the interface.

3.3.3. Probing the Au interface in alkaline media

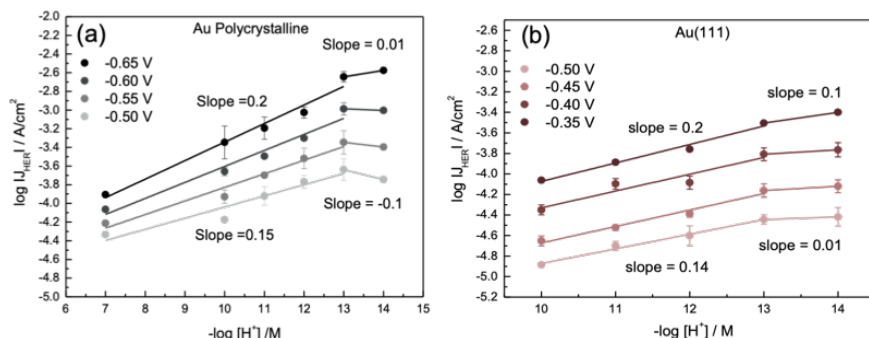


Figure 5 Reaction order of HER in bulk electrolyte pH for a constant concentration of cations in the bulk (0.1 M; except pH 14 where it is 1 M) on (a) Au polycrystalline and (b) Au(111) at 50 mV potential steps (vs RHE) plotted as a function of the logarithm of the current density on the y-axis and bulk pH on the x-axis. The corresponding slopes (reaction orders) are indicated next to the plots, where the slope at the bottom corresponds to the applied potential of -0.50 V (vs RHE) and the slope at the top corresponds to the applied potential of -0.65 V (vs RHE).

In order to gain a better understanding of the pH dependence of the Au-water interface in alkaline media, we performed electrochemical impedance spectroscopy (EIS) to determine the capacitance of the Au(111) electrode-electrolyte interface at different pH values. Figure 6 summarizes these results, where we fit the EIS data with the circuit shown in Figure 6a and in Figure 6b and 6c we plot the specific capacitance as obtained through these fits as a function of the applied potential (vs RHE) in the double layer region and the near HER region, respectively. It should be noted here that in order to fit the double-layer capacitance (C_{dl}) we have to employ a constant phase element (CPE; $Z_{\text{CPE}} = C_{\text{dl}}^{-1}(j\omega)^{-n}$) indicating that the double layer behaves non-ideally in these experiments, possibly due to interfacial heterogeneities arising from the surface disorder or due to the surface position dependent ion adsorption/diffusion phenomena.³⁴

Interestingly, even with the Au(111) electrode, the CPE exponent term (n) decreases with the increasing pH (see Figure S10 in Appendix B), indicating that the CPE behavior of the double layer must originate from the changes in the metal-electrolyte interactions as the electrolyte pH is changed. In fact, Lipkowski and co-workers have shown using *in situ* infrared spectroscopy measurements that anions such as OH^- , SO_4^{2-} and Cl^- can adsorb on Au(111) surface in the double layer region under near-neutral and alkaline conditions.³⁵ Thus, it can be expected that in our experiments, OH^- specific adsorption at the interface contributes to pseudocapacitive charging resulting in the CPE behavior of the double layer. Consequently, it is impossible to differentiate between the physical meaning of the double-layer capacitance (C_{dl}) term and the adsorption capacitance (C_{ad}) term in

the EEC (shown in Figure 6a) of the system, since both of these terms represent changes in the ion adsorption behavior at the interface.

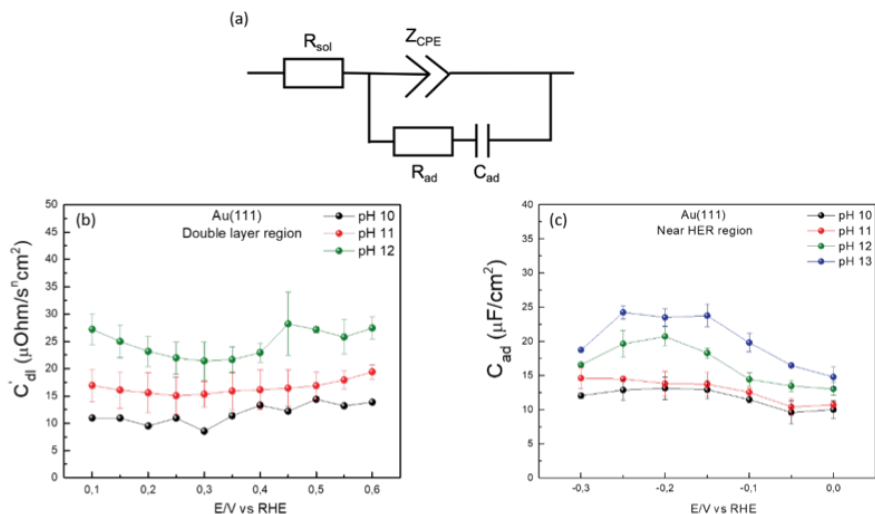


Figure 6 Electrochemical impedance spectroscopy on Au(111) in 0.1 M solutions at different pH values. (a) The equivalent electrical circuit (EEC) that was used to fit the data, featuring the R_{sol} term for the internal solution resistance, constant phase element term (Z_{CPE}) which is used to derive the double layer capacitance ($Z_{CPE} = C_{dl}^{-1}(j\omega)^{-n}$) under the assumption that C_{dl} represents the true double layer capacitance (C_{dl}) in the limit of $n \geq 0.95$ and R_{ad} , C_{ad} terms for the charge transfer resistance and the capacitance related to any adsorption phenomena at the interface. In the double layer region, where no Faradaic adsorption processes happen, R_{ad} and C_{ad} terms can be neglected as the main contribution in the overall capacitance comes from the Z_{CPE} (C_{dl}) term whereas near the onset of HER it is assumed that the main contribution in the overall capacitance comes from the C_{ad} term as the exponent term (n) for Z_{CPE} becomes quite low ($n \approx 0.2$), thereby losing any physical meaning. We plot the specific capacitance ($\mu F/cm^2$) as obtained through these fits in (b) double layer region and in (c) near-HER region, given by the C_{dl} term and C_{ad} term respectively, as a function of the applied potential (vs RHE).

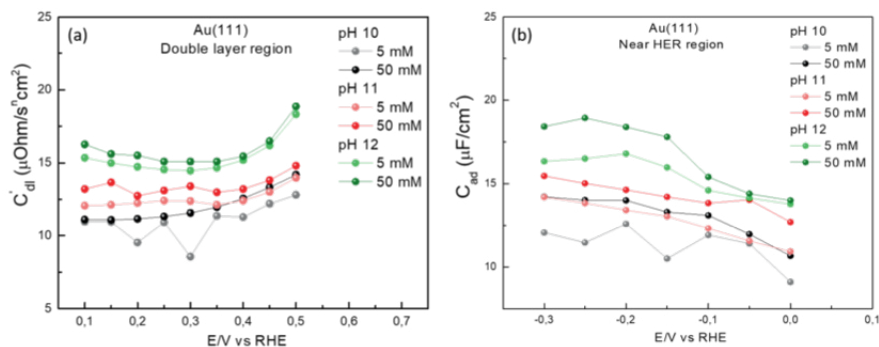


Figure 7 Electrochemical impedance spectroscopy on Au(111) at different cation concentrations (and pH) in the electrolyte, where the capacitance is derived from the same EEC as in Figure 5a. Here we plot the specific capacitance ($\mu F/cm^2$) as obtained from the fits at pH 10, pH 11 and pH 12, in the (a) double layer region (C_{dl}) and (b) near HER region (C_{ad}) at two different concentrations of the $NaClO_4$, namely, 5 mM and 50 mM, represented by light and dark data points respectively.

Additionally, it should be noted that all the potentials applied during the impedance measurements are more negative than the E_{pzc} of Au(111)

(0.474 V vs RHE at pH 0; $E_{pzc} = E^0_{pzc} + 0.059\text{pH}$),³³ resulting in a net negative interfacial electric field ($\Delta E = E - E_{pzc}$) at the electrode at all the investigated potentials. Hence, an increase in the interfacial capacitance (both C_{dl} and C_{ad}) with the increasing pH suggests a corresponding increase in the interfacial concentration of the cations. In order to confirm this effect, we performed additional EIS measurements at a constant pH with varying concentration of the cations in the electrolyte (shown in Figure 7). In agreement with our hypothesis, we observe an increase in the interfacial capacitance with the increasing cation concentration in the electrolyte. These analogous variations in the capacitance curves evidence that these two parameters, namely, the electrolyte pH and the bulk cation concentration, affect the electrode-electrolyte interface in a similar manner.

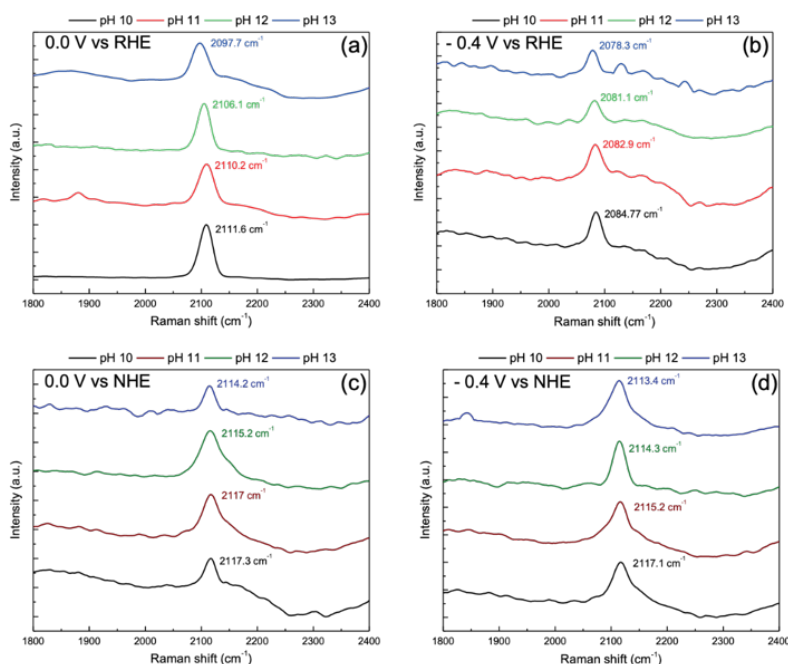


Figure 8 *In situ* surface Raman spectra of hydrogen adsorption on roughened Au polycrystalline electrode at (a) 0.0 V, (b) -0.4 V vs RHE and (c) 0.0 V, (d) -0.4 V vs NHE obtained in 0.1 M NaOH (pH 13), 0.01 M NaOH + 0.09 M NaClO₄ (pH 12), 0.001 M NaOH + 0.099 M NaClO₄ (pH 11) and 0.0001 M NaOH + 0.0999 M NaClO₄ (pH 10), in Ar sat. environment.

In order to gain further insights into the intrinsic pH dependence of the Au–water interface during hydrogen evolution we also performed *in situ* surface enhanced Raman spectroscopy (SERS) to probe the changes in the Au–H vibrational band as a function of the electrolyte pH. Figure 8 presents the SERS results, where we attribute the band located around 2100 cm⁻¹ to the H bonded on top of the Au surface atom.^{36–38} These results show that the Au–H vibrational band shifts to lower wavenumbers with the increasing electrolyte pH (pH 10 to pH 13) indicating that the nature of the adsorbed hydrogen is indeed pH dependent. Moreover, the pH dependent shift in the

band occurs both on the RHE scale and on the NHE scale, suggesting that these changes have an intrinsic pH dependence and they are not convoluted by the changes in the near-surface cation concentration. In principle, a shift to a lower wavenumbers with the increasing pH could indicate that the hydrogen bond strength decreases with the increasing pH, though one must be careful in electro-sorption systems to correlate changes in metal-adsorbate frequencies to corresponding changes in binding energies because there is no theoretical basis for such a correlation.³⁹⁻⁴⁰ Interestingly, Mao and co-workers have previously observed a similar pH dependence for the Pt—H vibrational band.³⁸ Notably, the observed Stark tuning effect for the Au—H band (see Appendix B Figure S12) is also similar to the previously reported Stark tuning effect for the Pt—H band.³⁸ While these spectroscopy measurements do not allow us to draw detailed quantitative conclusions, together with the impedance data, they do lead to two important qualitative conclusions that are in line with the conclusions of the previous section: (i) there is an intrinsic pH dependence of the (double layer structure of the) gold-aqueous electrolyte interface, presumably resulting in associated changes in the (weak) specific OH⁻ adsorption in double layer and the strength of the hydrogen adsorption in the HER window, and (ii) cation and pH effects are convoluted in the sense that higher pH invoke higher near-surface cation concentrations. We believe that an investigation into the nature of conclusion (i) requires a detailed study of its own.

3.4. Discussion

It is now well established that in alkaline media, the HER kinetics cannot be described aptly by only taking the changes in the HBE into account. There is ample experimental proof that in the alkaline pH window traditional descriptors fail to capture the complex non-Nernstian pH dependence of HER activity.⁴¹ Instead, various groups have successfully identified alternative interfacial parameters that impact the HER kinetics in alkaline media, for example the potential of zero charge pzc (or the interfacial electric field strength), the binding energy of the co-adsorbed hydroxyl ion or oxophilicity of surface sites in general, and the solvation energy of the spectator cations.^{15, 21, 24, 42} These parameters are believed to influence the rate-determining step in alkaline media, i.e. $\text{H}_2\text{O} + \text{e}^- + * \rightarrow \text{H}-* + \text{OH}^-$. However, in order to arrive at a unified theory that can capture all the experimental anomalies that exist in present literature, it is important to understand how these key parameters influence each other and which reaction conditions can be realized to amplify their effect on the HER kinetics.

Our results show that on Au electrodes, the overall activity for HER in alkaline media is indeed controlled the first electron transfer step, hence by the barrier of the electrochemical water dissociation ($\text{H}_2\text{O} + \text{e}^- + * \rightarrow \text{H}-* + \text{OH}^-$). This rate of this reaction is enhanced in the presence of cations near the surface under moderately alkaline conditions (pH 11). We note here that the cation concentration dependence of HER is reminiscent of the studies that have been conducted by Markovic and co-workers on modified

transition metal electrodes.¹⁵⁻¹⁷ Moreover, based on their experimental findings, they proposed a bi-functional mechanism for HER where in addition to the H adsorption, the HER activity is also dependent on the OH adsorption at the interface. However, in accordance with the recent studies by Tang and co-workers, we believe that any direct involvement of the adsorbed OH species in the HER mechanism would not be expected.⁴³ It is more likely that the cations improve the intrinsic kinetics of HER by bringing down the kinetic barrier for the electrochemical water dissociation step. This is very similar to a model suggested recently by our group in which the hydroxide is (transiently) stabilized by an oxophilic adatom on the platinum electrode.⁴² Therefore, the reactivity scales with (theoretical) oxophilicity of the adatoms, even though under conditions of HER, no OH is (or is expected to be) adsorbed at the interface, as supported by first-principles density functional theory calculations. Hence, we propose here that the cations in the (outer-)Helmholtz plane promote the hydrogen evolution by likewise favorably interacting with the transition state of the reaction ($\text{H}_2\text{O} + \text{e}^- + * + \text{cat}^+ \rightarrow * \text{H} \cdots \text{OH}^\delta \cdots \text{cat}^+ + (1-\delta)\text{e}^- \rightarrow * \text{H} + \text{OH}^- + \text{cat}^+$) thereby increasing the probability of electrochemical water dissociation at the metal interface. An alternative explanation would invoke the idea that the electric field in the double layer is affected by the cation concentration. We have previously argued that this electric field effect may influence the reorganization of interfacial water and thereby the rate of OH^- transfer through the double layer. We advocate here the model that cations favorably interact locally with the negatively-charged transition state because it is a simple and intuitive idea, but as in our recent paper,^[19] we cannot fully discard the more "global" electric field model (generating global field lines normal to the electrode surface). We note that this local promoting effect of cations (generating electric field radiating from the ion), stabilizing a key intermediate, has also been suggested for the electrocatalytic CO_2 reduction.⁴⁴ However, a more global effect has also been suggested, by some of the same authors.⁴⁵

At increasingly negative potential, we expect the concentration of cations near the surface to level off and to eventually to reach a maximum (very much like in a Langmuir or Frumkin isotherm). This would explain the near-zero reaction order in cation concentration at pH=12 (as shown in Figure 2) and, at very high cation concentration, the observed negative reaction order. The negative reaction order suggests an inhibitive effect, which is traditionally modeled by site blocking. Since it is unclear whether the cations actually chemically adsorb on surface sites (but see the computational work by Janik and co-workers)⁴⁶ or rather accumulate in double layer, the exact origin of this inhibition may not be fully clear. We do expect however that a high accumulation of cations in the double layer may have an adverse effect on the extent to which reactive water can reach the gold surface.

Therefore, an "empirical" rate law accounting for the observed cation effects would take the form:

$$v_1 = k_1^{eff,0} \left(1 - \frac{\Gamma_{cat,s}}{\Gamma_{max}}\right) \exp\left(-\frac{\alpha FE}{RT}\right) \Gamma_{cat,s}^\gamma \quad (1)$$

$k_1^{eff,0}$ is some effective standard rate constant, α is the transfer coefficient, F is Faraday's constant (96485 C mol⁻¹), E is the applied potential with respect to the standard potential of the reaction, R is the universal gas constant (8.314 J K⁻¹ mol⁻¹), T is the temperature (K), $\Gamma_{cat,s}$ is the surface concentration of cations (in mol cm⁻²), Γ_{max} is the maximum (saturated) surface concentration of cations, and γ is the (empirical) reaction order in the (local) cation concentration. This expression could be rewritten to show more explicitly that the activation energy of the reaction is lowered by a factor $\gamma RT \ln(\Gamma_{cat,s} / \Gamma_{max})$ due to the presence of cations near the interface. The potential dependence of $\Gamma_{cat,s}$ is then given by its corresponding isotherm expression (the Frumkin isotherm probably being the simplest reasonable candidate):

$$\frac{\Gamma_{cat,s}}{\Gamma_{max}-\Gamma_{cat,s}} = K^\circ \exp\left(\frac{F(E-E_{pzc})}{RT}\right) \exp\left(-g \frac{\Gamma_{cat,s}}{\Gamma_{max}}\right) [cat^+]_b \quad (2)$$

where K° is the standard equilibrium constant for cation adsorption at the bare surface, E_{pzc} is the potential of zero charge ($E_{pzc} = E_{pzc}^0 + 0.059\text{pH}_{\text{surface}}$ vs RHE) which incorporates the pH dependence of the HER kinetics, Γ_{max} is the maximum (saturated) surface concentration of cations, g is the Frumkin interaction parameter ($g > 0$ signifying repulsive interactions), and $[cat^+]_b$ is the bulk cation concentration. We stress that equations 1 and 2 are not supposed to model our data quantitatively; they are only meant to illustrate the various interrelated effects of cations in a simple model.

Alternatively, it can also be argued that the buffering effect of Na⁺ cations due to their hydrolysis at more alkaline conditions ($\text{pK}_{\text{hydrolysis}} = 14.2$) can lower the OH⁻ surface concentration $[\text{OH}^-]_s$ as the bulk electrolyte pH becomes more alkaline, thus countering the increase in the $\Gamma_{cat,s}$.⁴⁴ However, the experimentally (and theoretically) observed drop in the electrolyte pH with the increasing cation concentration (at pH 13; see Figure S13 in Appendix B) is small in comparison with the observed drop in the HER activity. Hence, it is much more likely that high cation coverage impedes the HER kinetics due to blockage effects.

Interestingly, the pH dependence of the observed reaction orders in cation concentration suggests that in addition to the bulk cation concentration, $\Gamma_{cat,s}$ can also be tuned via the electrolyte pH. Essentially, we observe that increasing electrolyte pH leads to a corresponding increase in the near surface cation concentration, at a constant potential on the RHE scale, and reaches saturation at pH=12. These results can be reconciled with the previously reported pH dependence of the interfacial electric field ($\Delta E = E - E_{pzc}$) due to the positive shift in the E_{pzc} with the increasing electrolyte pH ($E_{pzc} = E_{pzc}^0 + 0.059\text{pH}_{\text{surface}}$ vs RHE)^{21, 31-32} which will in-turn lead to an increase in the $\Gamma_{cat,s}$ (see eqn.2). An important consequence in terms of Eq.1 and 2 is that it may reproduce the pH dependence of HER on the RHE scale as an implicit function of the cation dependence of HER kinetics. Experimental results shown in section 3.2 confirm this prediction as we observe an increase in the HER activity on Au with the increasing pH (on the

RHE scale; refer to Figure 3). This is interesting because previously, the pH dependence of the local field strength has been correlated rather to the changes in the local solvent structure.^{21, 47} Here we emphasize that any changes in the interfacial electric field will also affect the local composition of the electrolyte thus establishing a direct correlation between the pH dependence and the cation dependence of HER activity. The combined effect of the cations/interfacial electric field on the kinetics of HER will be hard to decouple in an experiment, since they essentially emphasize local vs. global electric field effects that may be difficult to unequivocally separate.

It should be noted here, that on a pH independent scale (NHE or Ag/AgCl) where the E_{pzc} does not change with the electrolyte pH ($E_{pzc} = E^0_{pzc}$), eqn. 1 predicts a pH independent $\Gamma_{cat.s}$ and hence a pH independent reaction rate at a fixed potential (on the NHE scale). This agrees with the expectation that for a rate-limiting electrochemical water dissociation step an inherent pH dependence should not exist since no protons or hydroxide ions are involved in the reactant side of the rate limiting reaction ($H_2O + e^- + * \rightarrow H-* + OH^-$). However, the experimental results on the NHE scale show that the HER kinetics become more sluggish with the increasing pH (Figure 4), suggesting that the electrolyte pH has an intrinsic effect on the HER kinetics. These results show that in addition to its subsidiary role in tuning the near-surface cation concentration on the RHE scale, the electrolyte pH also affects the HER kinetics directly. One possible reason for the intrinsic pH dependence of the HER kinetics could be the changes in the HBE with the changing electrolyte pH. In fact, the pH dependence of the Au—H vibrational band, as shown in Figure 8, suggests that the nature of the adsorbed hydrogen changes with the electrolyte pH. However, further experimental and theoretical work is required in order to completely understand the intrinsic pH dependence of the HER kinetics on Au in the alkaline media. Importantly, of these two effects, the role of electrolyte pH in tuning $\Gamma_{cat.s}$ is dominant as it dictates the overall activity trend on the RHE scale where both effects of electrolyte pH should be operational. Additionally, the existence of these two opposing effects also explains the slightly lower reaction orders in the bulk electrolyte pH (≈ 0.2 ; pH 7 to pH 12) for a constant cation concentration (0.1 M) in comparison with the reaction orders obtained in cation concentration at moderately alkaline pH (≈ 0.5 at pH 11).

3.5. Conclusion

From the experimental evidence presented in this paper we conclude that that there exists an intricate interrelation between the cation and the pH effects on the HER kinetics in the alkaline media. We have shown here that on Au electrodes, the rate for the sluggish Volmer step is increased when the near-surface cation concentration is increased. Based on these results, we propose that the cations tune the kinetic energy barrier for HER by favorably interacting with the transition state of the rate determining step ($*H \text{ -- } OH^{\delta-} \text{ -- } cat^+$). Moreover, with the help of kinetic measurements and interfacial capacity measurements we elucidate the indirect role of bulk pH in tuning the near-surface cation concentration and shed light on the convoluted nature of pH effects for HER activity. Essentially, we observe

that on the RHE scale increasing pH results in increasing near-surface cation concentration, thereby improving the HER kinetics. Interestingly, it appears that in addition to these effects, electrolyte pH also affects the HER kinetics directly, by tuning the pre-exponential factor of the reaction. However, the overall activity trends demonstrate that near-surface cation concentration is the more important parameter in describing the HER activity in alkaline media on Au electrodes.

Furthermore, we show that on the Au surface cations provide optimal enhancement of the HER activity at intermediate pH values and that this promotional effect slows down at very high near-surface cation concentrations (with increasing pH and increasing bulk cation concentration in the bulk), even becoming inhibitive above a threshold concentration. This suggests that the optimal concentration of cations for promoting HER varies depending on the degree of stabilization required by the transition state of the reaction indicating that the observed activity trends are strongly dependent on the strength of the metal-water-cation interactions. Therefore, in order to optimize the activity of HER on different electrocatalysts it is imperative to study these interfaces individually.

To conclude, this work has elucidated the convoluted role of interfacial field strength and the electrolyte cation concentration in tuning the rate of the alkaline Volmer step. Essentially, we consider both the bulk cation concentration and the electrolyte pH affect the local surface concentration of cations, the latter by influencing the local field strength. Interfacial cations alter the kinetic barrier of the water dissociation step by transiently stabilizing the transition state in which the hydroxyl ion splits off from the water molecule. Moreover, the electrolyte pH also affects the nature of the adsorbed hydrogen at the interface, which further indicates a possible pH dependence of the hydrogen bond strength. Our results demonstrate that the different interfacial parameters that are generally proposed to play a key role in the HER kinetics, all play out simultaneously at the gold-electrolyte interface, thereby making it very difficult to experimentally decouple these effects and identify a single activity descriptor for HER in alkaline media. Instead, different electrode-electrolyte combinations need to be probed individually in order to assess which parameter is the more important for describing the HER activity on a given surface.

Acknowledgments

This work is part of the Advanced Research Center for Chemical Building Blocks (ARC CBBC) consortium, co-financed by the Netherlands Organization for Scientific Research (NWO) and Shell Global Solutions B.V.

References

1. Pentland, N.; Bockris, J. O. M.; Sheldon, E., Hydrogen Evolution Reaction on Copper, Gold, Molybdenum, Palladium, Rhodium, and Iron. *Journal of The Electrochemical Society* **1957**, *104* (3), 182.

2. Nørskov, J. K.; Bligaard, T.; Logadottir, A.; Kitchin, J. R.; Chen, J. G.; Pandelov, S.; Stimming, U., Trends in the Exchange Current for Hydrogen Evolution. *Journal of The Electrochemical Society* **2005**, *152* (3), J23.
3. Durst, J.; Simon, C.; Hasché, F.; Gasteiger, H. A., Hydrogen Oxidation and Evolution Reaction Kinetics on Carbon Supported Pt, Ir, Rh, and Pd Electrocatalysts in Acidic Media. *Journal of The Electrochemical Society* **2014**, *162* (1), F190-F203.
4. Sheng, W.; Gasteiger, H. A.; Shao-Horn, Y., Hydrogen Oxidation and Evolution Reaction Kinetics on Platinum: Acid vs Alkaline Electrolytes. *Journal of The Electrochemical Society* **2010**, *157* (11), B1529.
5. Durst, J.; Siebel, A.; Simon, C.; Hasché, F.; Herranz, J.; Gasteiger, H. A., New insights into the electrochemical hydrogen oxidation and evolution reaction mechanism. *Energy & Environmental Science* **2014**, *7* (7), 2255-2260.
6. Strmcnik, D.; Lopes, P. P.; Genorio, B.; Stamenkovic, V. R.; Markovic, N. M., Design principles for hydrogen evolution reaction catalyst materials. *Nano Energy* **2016**, *29*, 29-36.
7. Barber, J. H.; Conway, B. E., Structural specificity of the kinetics of the hydrogen evolution reaction on the low-index surfaces of Pt single-crystal electrodes in 0.5 M dm⁻³ NaOH. Dedicated to Professor W. Vielstich on the occasion of his 75th birthday.1. *Journal of Electroanalytical Chemistry* **1999**, *461* (1), 80-89.
8. Danilovic, N.; Subbaraman, R.; Strmcnik, D.; Stamenkovic, V.; Markovic, N., Electrocatalysis of the HER in acid and alkaline media. *Journal of the Serbian Chemical Society* **2013**, Medium: ED; Size: p. 2007-2015.
9. Zheng, J.; Sheng, W.; Zhuang, Z.; Xu, B.; Yan, Y., Universal dependence of hydrogen oxidation and evolution reaction activity of platinum-group metals on pH and hydrogen binding energy. *Science Advances* **2016**, *2* (3), e1501602.
10. Rheinländer, P. J.; Herranz, J.; Durst, J.; Gasteiger, H. A., Kinetics of the Hydrogen Oxidation/Evolution Reaction on Polycrystalline Platinum in Alkaline Electrolyte Reaction Order with Respect to Hydrogen Pressure. *Journal of The Electrochemical Society* **2014**, *161* (14), F1448-F1457.
11. Sheng, W.; Zhuang, Z.; Gao, M.; Zheng, J.; Chen, J. G.; Yan, Y., Correlating hydrogen oxidation and evolution activity on platinum at different pH with measured hydrogen binding energy. *Nature Communications* **2015**, *6* (1), 5848.
12. Parsons, R., The rate of electrolytic hydrogen evolution and the heat of adsorption of hydrogen. *Transactions of the Faraday Society* **1958**, *54* (0), 1053-1063.
13. Trasatti, S., Work function, electronegativity, and electrochemical behaviour of metals: III. Electrolytic hydrogen evolution in acid solutions. *Journal of Electroanalytical Chemistry and Interfacial Electrochemistry* **1972**, *39* (1), 163-184.
14. Conway, B. E.; Tilak, B. V., Interfacial processes involving electrocatalytic evolution and oxidation of H₂, and the role of chemisorbed H. *Electrochimica Acta* **2002**, *47* (22), 3571-3594.
15. Subbaraman, R.; Tripkovic, D.; Strmcnik, D.; Chang, K.-C.; Uchimura, M.; Paulikas, A. P.; Stamenkovic, V.; Markovic, N. M., Enhancing Hydrogen Evolution Activity in Water Splitting by Tailoring Li⁺-Ni(OH)₂-Pt Interfaces. *Science* **2011**, *334* (6060), 1256-1260.
16. Staszak-Jirkovský, J.; Malliakas, Christos D.; Lopes, Pietro P.; Danilovic, N.; Kota, Subrahmanyam S.; Chang, K.-C.; Genorio, B.; Strmcnik, D.; Stamenkovic, Vojislav R.; Kanatzidis, M. G.; Markovic, N. M., Design of active and stable Co-Mo-Sx chalcogels as pH-universal catalysts for the hydrogen evolution reaction. *Nature Materials* **2016**, *15* (2), 197-203.

17. Strmcnik, D.; Uchimura, M.; Wang, C.; Subbaraman, R.; Danilovic, N.; van der Vliet, D.; Paulikas, A. P.; Stamenkovic, V. R.; Markovic, N. M., Improving the hydrogen oxidation reaction rate by promotion of hydroxyl adsorption. *Nature Chemistry* **2013**, *5* (4), 300-306.
18. Fester, J.; García-Melchor, M.; Walton, A. S.; Bajdich, M.; Li, Z.; Lammich, L.; Vojvodic, A.; Lauritsen, J. V., Edge reactivity and water-assisted dissociation on cobalt oxide nanoislands. *Nature Communications* **2017**, *8* (1), 14169.
19. Chen, X.; McCrum, I. T.; Schwarz, K. A.; Janik, M. J.; Koper, M. T. M., Co-adsorption of Cations as the Cause of the Apparent pH Dependence of Hydrogen Adsorption on a Stepped Platinum Single-Crystal Electrode. *Angewandte Chemie International Edition* **2017**, *56* (47), 15025-15029.
20. McCrum, I. T.; Chen, X.; Schwarz, K. A.; Janik, M. J.; Koper, M. T. M., Effect of Step Density and Orientation on the Apparent pH Dependence of Hydrogen and Hydroxide Adsorption on Stepped Platinum Surfaces. *The Journal of Physical Chemistry C* **2018**, *122* (29), 16756-16764.
21. Ledezma-Yanez, I.; Wallace, W. D. Z.; Sebastián-Pascual, P.; Climent, V.; Feliu, J. M.; Koper, M. T. M., Interfacial water reorganization as a pH-dependent descriptor of the hydrogen evolution rate on platinum electrodes. *Nature Energy* **2017**, *2* (4), 17031.
22. Strmcnik, D.; Kodama, K.; van der Vliet, D.; Greeley, J.; Stamenkovic, V. R.; Marković, N. M., The role of non-covalent interactions in electrocatalytic fuel-cell reactions on platinum. *Nature Chemistry* **2009**, *1* (6), 466-472.
23. Dubouis, N.; Serva, A.; Berthin, R.; Jeanmairet, G.; Porcheron, B.; Salager, E.; Salanne, M.; Grimaud, A., Tuning water reduction through controlled nanoconfinement within an organic liquid matrix. *Nature Catalysis* **2020**, *3* (8), 656-663.
24. Xue, S.; Garlyyev, B.; Watzel, S.; Liang, Y.; Fichtner, J.; Pohl, M. D.; Bandarenka, A. S., Influence of Alkali Metal Cations on the Hydrogen Evolution Reaction Activity of Pt, Ir, Au, and Ag Electrodes in Alkaline Electrolytes. *ChemElectroChem* **2018**, *5* (17), 2326-2329.
25. Łukaszewski, M.; Soszko, M.; Czerwiński, A., Electrochemical Methods of Real Surface Area Determination of Noble Metal Electrodes – an Overview. *International Journal of Electrochemical Science* **2016**, *11*, 4442-4469.
26. Darwish, N. A.; Eggers, P. K.; Yang, W.; Paddon-Row, M. N.; Gooding, J. J. In *Step by step fabrication and characterization of Au (111) exposed single crystals*, 2010 International Conference on Nanoscience and Nanotechnology, 22-26 Feb. 2010; 2010; pp 302-305.
27. Lai, S. C. S.; Kley, S. E. F.; Rosca, V.; Koper, M. T. M., Mechanism of the Dissociation and Electrooxidation of Ethanol and Acetaldehyde on Platinum As Studied by SERS. *The Journal of Physical Chemistry C* **2008**, *112* (48), 19080-19087.
28. Ji, C.; Searson, P. C., Fabrication of nanoporous gold nanowires. *Applied Physics Letters* **2002**, *81* (23), 4437-4439.
29. Graf, M.; Jalaš, D.; Weissmüller, J.; Petrov, A. Y.; Eich, M., Surface-to-Volume Ratio Drives Photoelectron Injection from Nanoscale Gold into Electrolyte. *ACS Catalysis* **2019**, *9* (4), 3366-3374.
30. Shinagawa, T.; Garcia-Esparza, A. T.; Takanabe, K., Insight on Tafel slopes from a microkinetic analysis of aqueous electrocatalysis for energy conversion. *Scientific Reports* **2015**, *5* (1), 13801.
31. Garcia-Araez, N.; Climent, V.; Feliu, J., Potential-Dependent Water Orientation on Pt(111), Pt(100), and Pt(110), As Inferred from Laser-Pulsed

- Experiments. Electrostatic and Chemical Effects. *The Journal of Physical Chemistry C* **2009**, *113* (21), 9290-9304.
32. Sebastian, P.; Martinez-Hincapie, R.; Climent, V.; Feliu, J. M., Study of the Pt (111) vertical bar electrolyte interface in the region close to neutral pH solutions by the laser induced temperature jump technique. *Electrochimica Acta* **2017**, *228*, 667-676.
33. Kolb, D. M.; Schneider, J., Surface reconstruction in electrochemistry: Au(100)-(5 × 20), Au(111)-(1 × 23) and Au(110)-(1 × 2). *Electrochimica Acta* **1986**, *31* (8), 929-936.
34. Bard, A. J.; Faulkner, L. R., *Electrochemical methods : fundamentals and applications* Wiley: New York, **1980**.
35. Chen, A.; Lipkowski, J., Electrochemical and Spectroscopic Studies of Hydroxide Adsorption at the Au(111) Electrode. *The Journal of Physical Chemistry B* **1999**, *103* (4), 682-691.
36. Hesse, E.; Creighton, J. A., Investigation by Surface-Enhanced Raman Spectroscopy of the Effect of Oxygen and Hydrogen Plasmas on Adsorbate-Covered Gold and Silver Island Films. *Langmuir* **1999**, *15* (10), 3545-3550.
37. Bicelli, L.; Bozzini, B.; Mele, C.; D'Urzo, L., A Review of Nanostructural Aspects of Metal Electrodeposition. *International Journal of Electrochemical Science* **2008**, *3*.
38. Tian, Z.-Q.; Ren, B.; Chen, Y.-X.; Zou, S.-Z.; Mao, B.-W., Probing electrode/electrolyte interfacial structure in the potential region of hydrogen evolution by Raman spectroscopy. *Journal of the Chemical Society, Faraday Transactions* **1996**, *92* (20), 3829-3838.
39. Wasileski, S. A.; Koper, M. T. M.; Weaver, M. J., Metal electrode-chemisorbate bonding: General influence of surface bond polarization on field-dependent binding energetics and vibrational frequencies. *The Journal of Chemical Physics* **2001**, *115* (17), 8193-8203.
40. Wasileski, S. A.; Koper, M. T. M.; Weaver, M. J., Field-Dependent Electrode-Chemisorbate Bonding: Sensitivity of Vibrational Stark Effect and Binding Energetics to Nature of Surface Coordination. *Journal of the American Chemical Society* **2002**, *124* (11), 2796-2805.
41. Rebollar, L.; Intikhab, S.; Oliveira, N. J.; Yan, Y.; Xu, B.; McCrum, I. T.; Snyder, J. D.; Tang, M. H., "Beyond Adsorption" Descriptors in Hydrogen Electrocatalysis. *ACS Catalysis* **2020**, *10* (24), 14747-14762.
42. McCrum, I. T.; Koper, M. T. M., The role of adsorbed hydroxide in hydrogen evolution reaction kinetics on modified platinum. *Nature Energy* **2020**, *5* (11), 891-899.
43. Rebollar, L.; Intikhab, S.; Snyder, J. D.; Tang, M. H., Determining the Viability of Hydroxide-Mediated Bifunctional HER/HOR Mechanisms through Single-Crystal Voltammetry and Microkinetic Modeling. *Journal of the Electrochemical Society* **2018**, *165* (15), J3209-J3221.
44. Resasco, J.; Chen, L. D.; Clark, E.; Tsai, C.; Hahn, C.; Jaramillo, T. F.; Chan, K.; Bell, A. T., Promoter Effects of Alkali Metal Cations on the Electrochemical Reduction of Carbon Dioxide. *Journal of the American Chemical Society* **2017**, *139* (32), 11277-11287.
45. Ringe, S.; Clark, E. L.; Resasco, J.; Walton, A.; Seger, B.; Bell, A. T.; Chan, K., Understanding cation effects in electrochemical CO₂ reduction. *Energy & Environmental Science* **2019**, *12* (10), 3001-3014.
46. Mills, J. N.; McCrum, I. T.; Janik, M. J., Alkali cation specific adsorption onto fcc(111) transition metal electrodes. *Physical Chemistry Chemical Physics* **2014**, *16* (27), 13699-13707.

47. Reboilar, L.; Intikhab, S.; Snyder, J. D.; Tang, M. H., Kinetic Isotope Effects Quantify pH-Sensitive Water Dynamics at the Pt Electrode Interface. *The Journal of Physical Chemistry Letters* **2020**, *11* (6), 2308-2313.



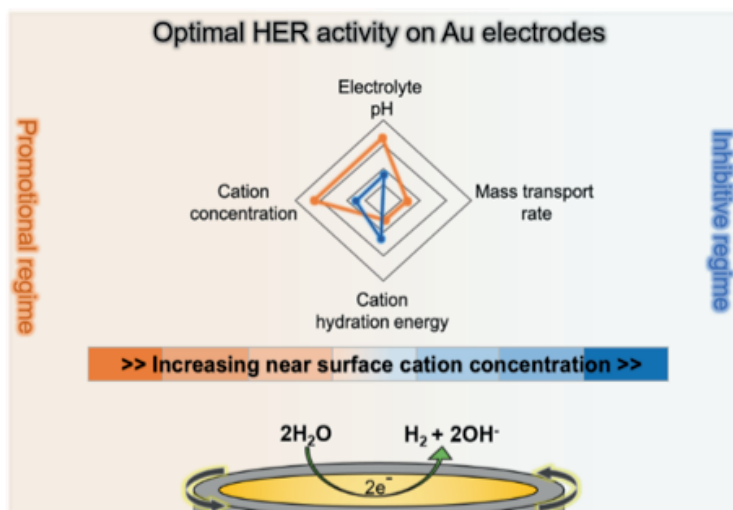
Chapter 4

Understanding the role of mass transport in tuning the hydrogen evolution kinetics on gold in alkaline media



Abstract

In this work we present an in-depth study on the role of mass transport conditions in tuning the hydrogen evolution kinetics on gold by the means of rotation rate control. Interestingly, we find that the HER activity decreases with increasing rotation rate of the electrode. As we increase the rotation (mass transport) rate, the locally generated hydroxyl ions ($2\text{H}_2\text{O} + 2\text{e}^- \rightarrow \text{H}_2 + 2\text{OH}^-$) are transported away from the electrode surface at an accelerated rate. This results in decreasing local pH and, due to the need to satisfy local electroneutrality, decreasing near-surface cation concentration. This decrease in the near-surface cation concentration results in the suppression of HER. This is because the cations near the surface play a central role in stabilizing the transition state for the rate determining Volmer step ($^*\text{H} \text{---} \text{OH}^{\delta-} \text{---} \text{cat}^+$). Furthermore, we present a detailed analytical model that qualitatively captures the observed mass transport dependence of HER solely based on the principle of electroneutrality. Lastly, we also correlate the cation identity dependence of HER on gold ($\text{Li}^+ < \text{Na}^+ < \text{K}^+$) to the changes in the effective concentration of the cations in the double layer with the changes in their solvation energy.



This chapter is based on the article:

Goyal, A.; Koper, M. T. M., Understanding the role of mass transport in tuning the hydrogen evolution kinetics on gold in alkaline media. *The Journal of Chemical Physics* **2021**, *155* (13), 134705.

4.1. Introduction

Research on the hydrogen evolution reaction (HER) in alkaline media ($2\text{H}_2\text{O} + 2\text{e}^- \rightarrow \text{H}_2 + 2\text{OH}^-$) continues to be of utmost importance for the generation of green hydrogen via alkaline water electrolysis.¹⁻² Moreover, understanding the activity trends for HER is also crucial for the development of other renewable energy technologies, such as CO_2 electroreduction and electrochemical biomass upconversion, where HER can bring down the Faradaic efficiency of the process by acting as a parasitic side reaction.³⁻⁷ Additionally, understanding the kinetic trends for this reaction is also central to our fundamental understanding of electrochemistry, since HER has long served as a model reaction for the theories and laws of electrocatalysis. In this regard, the slow kinetics of HER in alkaline media remains an active area of research, since traditional activity descriptors fail to capture/predict the experimentally observed trends under alkaline conditions.

Traditionally, the hydrogen binding energy (HBE) on the electrocatalyst surface has been used to describe the HER kinetics in acidic electrolytes, where it successfully captures the changes in the HER activity on different metal surfaces.⁸⁻¹¹ However, this descriptor suffers from certain shortcomings as it not only fails to capture the experimental trends on different catalysts in alkaline media, but it also fails to explain the non-Nernstian pH dependence of HER kinetics.¹² It is now widely accepted that in order to describe the HER kinetics completely, especially under alkaline conditions, there is a need to move beyond HBE as main descriptor, and instead focus on the influence of the electrochemical environment at the metal-electrolyte interface. In fact, various groups have successfully identified different interfacial parameters such as the interfacial field strength, oxophilicity of the surface sites, and the cation solvation energy, to name a few, as important descriptors for the kinetics of hydrogen evolution in alkaline media.¹³⁻¹⁶ It has been shown that these interfacial parameters can affect the HER kinetics by means of favorable/unfavorable interactions with the dissociating water molecule at the interface ($\text{H}_2\text{O} + \text{e}^- + * \rightarrow \text{H}-* + \text{OH}^-$). Hence, it appears that in addition to the HBE, the interaction of the reacting water molecules and the resulting hydroxyl ions also need to be considered in order to describe the electrochemical water dissociation (Volmer step) in alkaline media completely. Eventually, a combination of different parameters may be required to accurately predict the overall HER rate.

In this light, alkali metal cations are one of the most crucial electrolyte parameters in describing the HER kinetics in alkaline media as they can have a strong interaction with the metal surface as well as the reactants ($\text{H}_2\text{O}_{\text{ads}}$) and products (OH_{ads} , OH^-) of HER. Markovic and co-workers have shown that on transition metal hydroxide modified Pt electrodes, HER kinetics improves in Li^+ ion containing electrolytes, which they attribute to the stabilizing effect of Li^+ ions on the adsorbed hydroxyl ($*\text{OH}^{\text{--cat}^+}$) species at the interface.¹⁷⁻¹⁸ However, more recently, our group, as well as Tang and co-workers, have shown that a direct involvement of the adsorbed hydroxyl species is not always viable under the conditions of HER (very negative overpotentials).^{15, 19} Instead, it is expected that cations affect the

reacting water molecule at the surface, by changing the barrier height for the rate determining Volmer step. In addition to the debated role of the cations in stabilizing the $\text{H}_2\text{O}_{\text{ads}}/\text{OH}_{\text{ads}}$ at the surface, it has also been shown that cations can directly adsorb at the interface (by partially losing their hydration shell), thus disrupting the $\text{H}_2\text{O}-\text{OH}_{\text{ads}}$ network and weakening the binding of OH_{ads} at the surface.²⁰⁻²¹ However, the exact mechanism behind the cation assisted HER in alkaline media remains disputed, as inconsistencies exist in the activity trends with cation identity on HER kinetics. It has been shown by Bandarenka and co-workers that while on Pt and Ir electrodes, the HER kinetics improves in going from $\text{CsOH} < \text{KOH} < \text{NaOH} < \text{LiOH}$, on Au and Ag electrodes the opposite trend is observed.²² Recently, we have shown that in addition to the inconsistencies in the alkali metal cation identity effects, pH affects the HER rate on Pt(111) and Au(111) electrodes differently.²³ While it was shown previously that on the Pt(111) surface HER activity increases in going from pH 13 to pH 11, in the case of Au(111), the opposite trend is observed. We have shown that there is a direct correlation between pH effects and cation effects for HER kinetics on gold, showing that as the electrolyte pH is increased, the near-surface cation concentration also increases due to the increasing negative charge density at the electrode. This work demonstrated the central role of cations on the kinetics of HER in alkaline media and explained, in part, the anomalous pH dependence of this reaction. Moreover, we showed that at high cation concentrations, the promotional effect of cations plateaus and eventually becomes inhibitive, which we ascribed to the blockage/crowding of the reactive surface by the near-surface cations.²⁴

In this work, we study the role of mass transport in tuning the HER kinetics on polycrystalline Au electrodes by the means of controlling the local pH gradients. We exploit the fact that as the mass transport conditions are enhanced, the local alkalinity at the surface is suppressed due to the accelerated transport of OH^- ions away from the electrode. Rather than a direct pH effect, we attribute the effect of mass transport on HER kinetics to a corresponding decrease in the near-surface cation concentration due to the need to satisfy the conservation of local electroneutrality. Hence, the increasing rotation rate lowers HER activity on Au by indirectly controlling the local cation concentration at the interface, which is a central parameter in tuning HER kinetics. Moreover, we show that the rotation rate dependence of HER is dependent on both bulk pH and cation identity. These trends underscore the lower effective concentration of Li^+ cations in near-surface region due to their larger hydration shell. In summary, this work provides rational guidelines for selectively tuning the HER kinetics in alkaline media by carefully manipulating the near surface electrolyte environment by means of bulk pH, cation identity and mass transport.

4.2. Experimental section

4.2.1. Chemicals

The electrolytes were prepared from H_2SO_4 (98% by wt. solution, EMSURE, Merck), LiClO_4 (99%, anhydrous, Alfa Aesar), NaClO_4 (99.99%, trace metals basis, Sigma-Aldrich), KClO_4 ($\geq 99.99\%$, trace metals basis, Sigma-Aldrich),

LiOH (99.995%, Alfa Aesar), NaOH (32% by wt. solution, analysis grade, Merck), KOH ($\geq 99.995\%$, Suprapur, Merck) and Ultrapure water (MilliQ gradient, $\geq 18.2 \text{ M}\Omega\text{cm}$, TOC $< 5 \text{ ppb}$). Ar (6.0 purity, Linde) and H₂ (5.0 purity, Linde) were used for purging the electrolytes.

4.2.2. General electrochemical methods

The electrochemical measurements at pH 10 to pH 12 were carried out in home-made borosilicate glass cells and measurements at pH 13 (and higher) were carried out in a home-made PTFE cell. The reference electrode was separated from the working compartment with the help of a Luggin capillary and the counter electrode was a Au wire (99.99% purity), unless otherwise stated. The glassware was cleaned prior to each experiment by boiling it five times in ultrapure water. When not in use, the glassware was stored in 1 g/L solution of KMnO₄ (acidified). Before boiling, any traces of KMnO₄ and MnO₂ were removed from the glassware by submerging it in a diluted solution of acidified H₂O₂ (few drops of conc. H₂SO₄ and 10-15 mL H₂O₂ in excess water) for half an hour. Before every experiment, the electrolytes were purged for ca. 20 minutes with Ar to remove any dissolved oxygen from the electrolyte. Moreover, during the measurement, Ar was also bubbled over the headspace of the electrochemical cell, in order to eliminate any interference from the ambient oxygen. A home-made reversible hydrogen electrode (RHE) was used as the reference electrode in all the experiments. All the electrochemical measurements were carried out using a Ivium technologies (CompactStat.h standard) potentiostat and a MSR rotator (Pine Research). For all the CVs taken, 85% Ohmic drop compensation was performed. The Ohmic drop of the electrolyte was determined by carrying out electrochemical impedance spectroscopy (EIS) at 0.05 V (vs RHE; double-layer region). In all the measurements the working electrode was a Au polycrystalline disk in E6/E5 ChangeDisk tips embedded a PEEK shroud (Pine Research).

Before each experiment, the Au polycrystalline disk (diameter = 5mm, Pine instruments) was mechanically polished on Buehler micro-polishing cloth (8 inches) with decreasing sizes of diamond polishing suspension, namely, 3 μm , 1 μm and 0.25 μm . Next, the disk was sonicated in ultrapure water and acetone for 10 minutes to remove any organic/inorganic impurities, and mounted on the RDE tip. Thereafter, the Au polycrystalline disk was electrochemically polished in 0.1 M H₂SO₄ (0.05 V to 1.75 V vs RHE, 200 cycles at a scan rate of 1 V s⁻¹) by going to the Au oxide formation and reduction region.²⁵ Prior to each experiment, a characterization cyclic voltammetry (CV) of the disk was obtained in the same potential window where the electrochemical polishing was performed (at a scan rate of 50 mV s⁻¹), as shown in Figure S5 (Appendix C). For calculating the current densities for the HER activity, the electrochemically active surface area (ECSA) of the disk was determined by calculating the charge from the reduction peak for the Au oxide in the characterization CV and dividing it by the specific charge of one monolayer of Au (390 $\mu\text{C cm}^{-2}$).²⁵ The working electrode was then used for the electrochemical measurements.

Table 1 Compositions of the electrolytes employed for the pH dependence studies of HER

Bulk pH	[CatOH] /M Cat ⁺ = Li ⁺ , Na ⁺ , K ⁺	[CatClO ₄] /M Cat ⁺ = Li ⁺ , Na ⁺ , K ⁺	Total ion concentration /M
10	10 ⁻⁴	9.99 × 10 ⁻²	2 × 10 ⁻¹
11	10 ⁻³	9.9 × 10 ⁻²	2 × 10 ⁻¹
12	10 ⁻²	9 × 10 ⁻²	2 × 10 ⁻¹
13	10 ⁻¹	—	2 × 10 ⁻¹

4.2.3. Electrochemical measurements for HER activity

The studies for the pH dependence and the disk rotation rate dependence of HER were done in Ar sat. 0.1 M electrolytes, as shown Table 1. Additionally, studies were done in 1 M and 2 M KOH containing electrolytes in a PTFE cell. The CVs were taken in the potential window of 0 V to -0.65 V vs RHE at a scan rate of 25 mVs⁻¹ and the working electrode was rotated at different rotation rates (2500 rpm, 2100 rpm, 1800 rpm, 1600 rpm, 1400 rpm and 1200 rpm) in every measurement. The rotation rate was always changed from the highest to the lowest rate, to make sure that any changes in the local pH from the previous measurement do not interfere with the current measurement. Moreover, in between different measurements, the electrode was rotated at a given rotation rate for two minutes, to make sure that the system had enough time to reach steady state conditions.

All the studies for the bulk cation concentration dependence of HER were done at pH 11 (10⁻³ M CatOH), and pH 13 (0.1 M CatOH) where the cation concentration was varied in the electrolyte by adjusting the concentration of CatClO₄, as shown in Table 2. The CVs were taken in the potential window of 0 V to -0.65 V vs RHE at a scan rate of 25 mV s⁻¹ and the working electrode was rotated at 2500 rpm in every measurement.

Table 2 Compositions of the electrolytes employed for the cation concentration studies for HER

Bulk pH	[CatOH] /M Cat ⁺ = Li ⁺ , Na ⁺ , K ⁺	[CatClO ₄] /M	Total ion concentration /M	
11	10 ⁻³	LiClO ₄ /NaClO ₄	5 × 10 ⁻³	1.2 × 10 ⁻²
			5 × 10 ⁻²	1.02 × 10 ⁻¹
			2.5 × 10 ⁻¹	5.02 × 10 ⁻¹
			5 × 10 ⁻¹	≈ 10 ⁰
			10 ⁰	2 × 10 ⁰
		KClO ₄	5 × 10 ⁻³	1.2 × 10 ⁻²
			2.5 × 10 ⁻²	5.2 × 10 ⁻²
			5 × 10 ⁻²	1.02 × 10 ⁻¹
			10 ⁻¹	2.02 × 10 ⁻¹
			—	—
13	10 ⁻¹	LiClO ₄ /NaClO ₄	5 × 10 ⁻³	2.1 × 10 ⁻¹
			5 × 10 ⁻²	3 × 10 ⁻¹
			2.5 × 10 ⁻¹	7 × 10 ⁻¹

		KClO ₄	5×10^{-1}	1.2×10^0
			10^0	2.2×10^0
			5×10^{-3}	2.1×10^{-1}
			2.5×10^{-2}	2.5×10^{-1}
			5×10^{-2}	3×10^{-1}
			10^{-1}	4×10^{-1}

4.3. Results and discussion

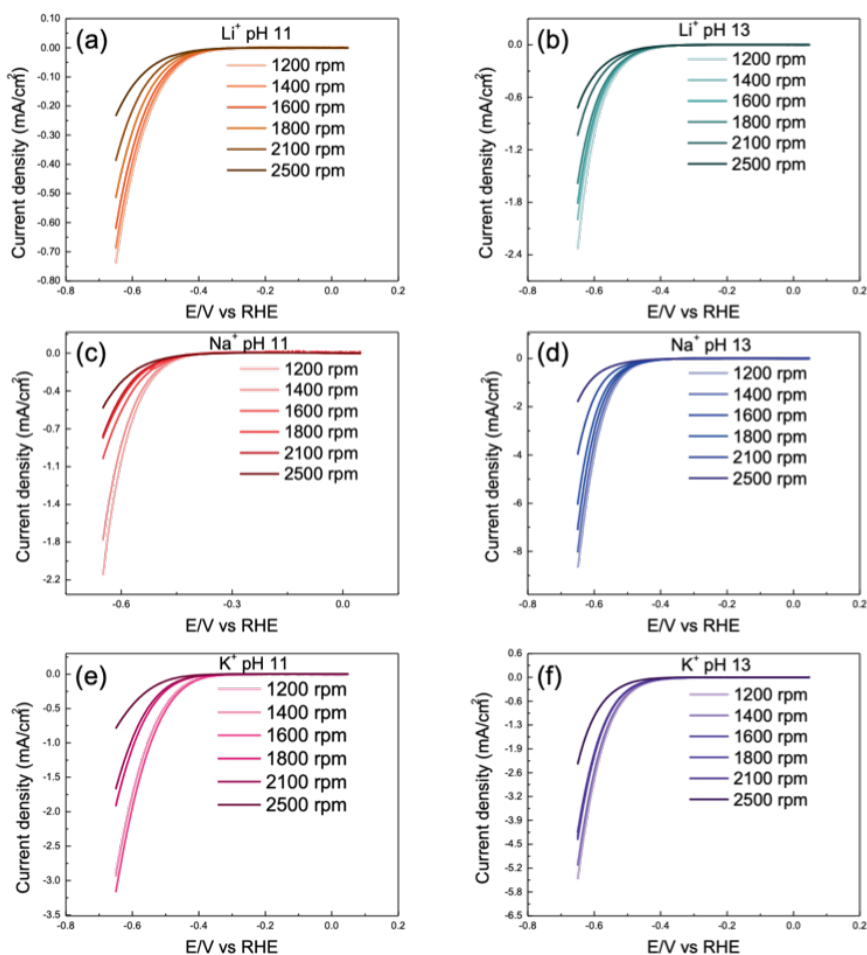


Figure 1 Negative-going scan of the cyclic voltammograms obtained for HER on Au polycrystalline surface in 0.1 M Li⁺ ion containing electrolytes at (a) pH 11 and (b) pH 13, in 0.1 M Na⁺ ion containing electrolytes at (c) pH 11 and (d) pH 13, and in 0.1 M K⁺ ion containing electrolytes at (e) pH 11 and (f) pH 13 at a fixed cation concentration in the bulk (0.1 M) at different rotation rates (2500 rpm, 2100 rpm, 1800 rpm, 1600 rpm, 1400 rpm and 1200 rpm) at a scan rate of 25 mVs⁻¹.

In Fig. 1 we show that on the polycrystalline Au surface, HER activity improves as we go from a lower rotation rate to a higher rotation rate in different alkali metal ion containing electrolytes. These results are counter-intuitive since HER under alkaline conditions proceeds via water reduction

reaction ($2\text{H}_2\text{O} + 2\text{e}^- \rightarrow \text{H}_2 + 2\text{OH}^-$) and in principle, it should be mass transport independent. However, in addition to the enhanced mass transport of the reactants to the electrode surface, the rotation rate of the electrode also tunes the local pH gradients. It is well known that during HER the local pH in the diffusion layer is higher compared to the bulk, both in acidic conditions (proton reduction) and in alkaline conditions (water reduction), due to proton consumption and hydroxyl ion generation, respectively.²⁶⁻²⁸ Here, the rotating rate of the electrode tunes these gradients via the control of the diffusion layer thickness.^{3, 29} Briefly, an increasing rotation rate results in an accelerated transport of OH^- ions away from the electrode surface, thereby leading to a lower local alkalinity. Hence, the observed rotation rate dependence, as shown in Fig. 1, suggests a local pH dependence for HER on Au.

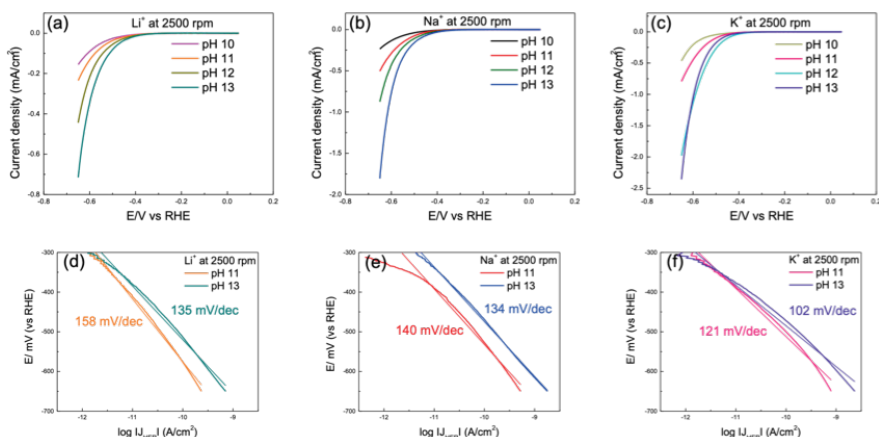


Figure 2 Negative-going scan of the cyclic voltammograms obtained for HER on Au polycrystalline surface in (a) Li^+ , (b) Na^+ and (c) K^+ containing electrolytes at a fixed cation concentration in the bulk (0.1 M) at different electrolyte pH (pH 10, pH 11, pH 12 and pH 13) at 2500 rpm and a scan rate of 25 mVs^{-1} . Tafel slope analysis for HER on Au polycrystalline surface in (a) Li^+ , (b) Na^+ and (c) K^+ containing electrolytes at pH 11 and pH 13, obtained from the data shown in (a), (b) and (c).

In Fig. 2 we probe this further and we find that the HER activity is indeed pH dependent. We see that it improves with increasing pH (pH 10 to pH 13) in electrolytes containing different alkali metal cations. Moreover, the Tafel slope analysis also confirms that the HER kinetics improves with the increasing bulk pH. Here, the pH dependence of HER kinetics agrees with our recent work where we have argued that since the potential of zero charge shifts positively (on the RHE scale) with the increasing pH ($E_{pzc} = E_{pzc}^0 + 0.059\text{pH}$), the interfacial electric field becomes more negative with the increasing pH at the same applied potential on the RHE scale.³⁰⁻³¹ Consequently, the near-surface cation concentration also increases with the electrolyte pH, to counter the increasingly negative charge density at the surface (at a constant E_{RHE}/V).²³ In our recent work, we proposed that cations near the surface can enhance the HER activity on Au electrodes by favorably interacting with the transition state of the rate determining Volmer

step ($\text{H}_2\text{O} + \text{e}^- + * + \text{cat}^+ \rightarrow * \text{H} - \text{OH}^{\delta-} - \text{cat}^+ + (1-\delta)\text{e}^- \rightarrow * \text{H} + \text{OH}^- + \text{cat}^+$).²³

This shows that the bulk pH dependence of the HER kinetics expresses, at least in part, a dependence on the near-surface cation concentration. This can be expressed as an empirical rate law expression for HER as follows:

$$v_1 = k_1^{eff0} \exp\left(-\frac{\alpha FE}{RT}\right) [\text{Cat}^+]_s^\gamma \quad (1)$$

where, k_1^{eff0} is the standard rate constant, α is the transfer coefficient, F is Faraday's constant (96485 C mol^{-1}), E is the applied potential with respect to the standard potential of the reaction, R is the universal gas constant ($8.314 \text{ J K}^{-1} \text{ mol}^{-1}$), T is the temperature (K), $[\text{Cat}^+]_s$ is the surface concentration of cations (in mol cm^{-3}) and γ is the (empirical) reaction order in the (local) cation concentration.

We note here that while the results shown in Fig. 2 capture the dependence of HER kinetics on near surface cation concentration as a function of the bulk pH, these results still do not elucidate the local pH dependence of HER, as shown in Fig. 1. This is because the bulk pH and hence, the interfacial electric field strength at a given potential (vs RHE) remains constant in all the measurements in Fig. 1, regardless of the rotation rate. However, in accordance with the conservation of local electroneutrality, we would expect the near-surface cation concentration to also vary with the local pH gradients even at a constant field strength. In principle, local electroneutrality will lead to a lower local cation concentration in response to a decrease in the local concentration of hydroxyl ions. Hence, increasing rotation rate will result in a corresponding lower local cation concentration due to the changes in the local pH, such that $[\text{Cat}^+]_s = [\text{Cat}^+]_b + \beta([\text{OH}^-]_s - [\text{OH}^-]_b)$ (where β is a kind of a local transference number; see section S1 in Appendix C for more details). This explains the observed suppression of HER with increasing rotation rate (as shown in Fig. 1). We can express this analytically in a simple model by assuming that under steady-state conditions the OH^- generation rate (HER rate) must be equal to its diffusion rate:

$$k_1^{eff0} \exp\left(-\frac{\alpha FE}{RT}\right) ([\text{Cat}^+]_b + \beta([\text{OH}^-]_s - [\text{OH}^-]_b))^\gamma = \frac{D_{\text{OH}^-}}{\delta_{\text{OH}^-}} ([\text{OH}^-]_s - [\text{OH}^-]_b) \quad (2)$$

Where, $[\text{OH}^-]_s$ is the surface concentration of hydroxyl ions (in mol cm^{-3}), $[\text{OH}^-]_b$ is the bulk concentration of hydroxyl ions (in mol cm^{-3}), δ_{OH^-} is the diffusion layer thickness ($\delta_{\text{OH}^-} = 1.61 \times D_{\text{OH}^-}^{\frac{1}{3}} \times \nu^{\frac{1}{6}} \times \omega^{\frac{1}{2}}$), D_{OH^-} is the diffusion coefficient of OH^- ($5.273 \times 10^{-5} \text{ cm}^2/\text{s}$), ν is the kinematic viscosity of water ($8.9 \times 10^{-3} \text{ cm}^2/\text{s}$) and ω is the angular frequency of rotation (in rad/s) and the rest of the symbols have the same meaning as before. Hence, the rotation rate/mass transport rate dependence of the diffusion layer thickness (δ ; calculated from the Levich eqn.) indirectly affects the near-surface cation concentration by controlling the local pH at the surface.

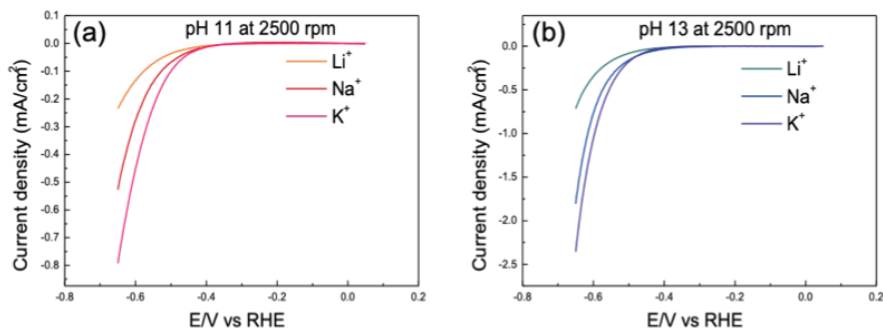


Figure 3 Negative-going scan of the cyclic voltammograms obtained for HER on Au polycrystalline surface for a fixed cation concentration in the bulk (0.1 M) at (a) pH 11 and (b) pH 13 at 2500 rpm and a scan rate of 25 mVs⁻¹ in electrolytes containing different alkali metal cations: Li⁺, Na⁺ and K⁺.

Moreover, we note here that the eqn. 1 and 2 could be rewritten to show more explicitly that the activation energy of the reaction is lowered by a factor $\gamma RT \ln(\Gamma_{\text{cat},s} / \Gamma_{\text{max}})$ due to the presence of cations near the interface, with $\Gamma_{\text{cat},s}$ the surface concentration of cations in the double layer (in mol cm⁻²) and Γ_{max} the maximum (saturated) surface concentration of cations in the double layer.²³ It is important to distinguish between surface concentration, which is the cation concentration just outside the double layer, and the cation concentration in the double layer, which includes the effect of cation interaction with the surface. For instance, for the same surface concentration, we expect Cs⁺ to have a higher double-layer concentration than Li⁺, due to its weaker hydration and stronger tendency for specific adsorption. Therefore, $\Gamma_{\text{cat},s}$ is related to $[\text{Cat}^+]_s$ by an isotherm expression including the interaction energy between ion and surface.

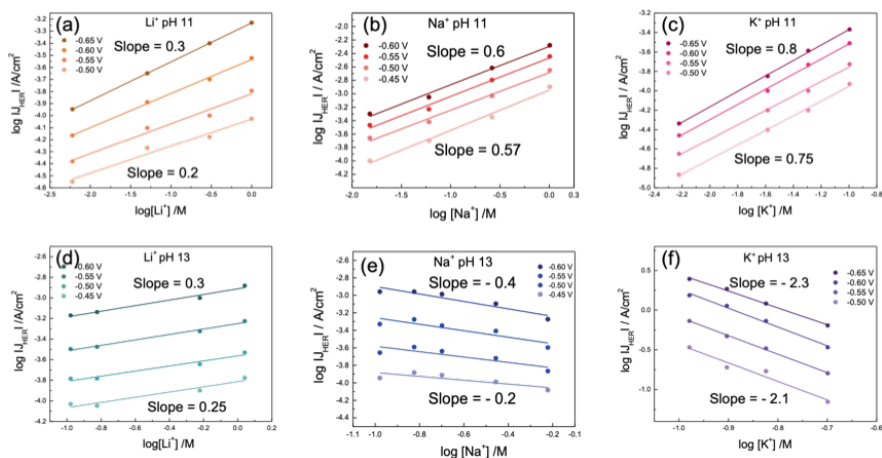


Figure 4 Reaction order plots obtained for HER on Au polycrystalline surface at pH 11 in (a) Li⁺, (b) Na⁺ and (c) K⁺ ion containing electrolytes and at pH 13 in (d) Li⁺, (e) Na⁺ and (f) K⁺ ion containing electrolytes with varying cation concentration in the bulk at different 2500 rpm at a scan rate of 25 mVs⁻¹ where the slope indicates the corresponding reaction order at a fixed potential (vs RHE).

We further studied the role of these cation interaction effects by varying the cation identity in the electrolyte. In fig. 3 we see that the HER activity on

Au electrodes increases in the order: $\text{Li}^+ < \text{Na}^+ < \text{K}^+$ in alkaline conditions (pH 11 and pH 13). Here the cation identity trend for HER kinetics agrees well with the expected interaction strength of cations with the metal interface and the reacting water molecule. Amongst the different alkali metal cations, Li^+ ions tend to have the weakest interaction with the electrified interface owing to their higher degree of solvation.^{20-21, 32} Moreover, Bandarenka and co-workers have also shown previously that on the Au(111) interface, the experimentally obtained double-layer capacitance increases in going from Li^+ to Cs^+ at a fixed bulk cation concentration, suggesting that the effective double-layer concentration of the cations increases ($\text{Li}^+ < \text{Na}^+ < \text{K}^+ < \text{Cs}^+$) with the decreasing solvation energy of the cations.³³⁻³⁴ Based on these results, we propose that the enhancement in the HER activity on Au electrodes in going from Li^+ to K^+ is associated to the increase in effective concentration of the cations near the surface ($\Gamma_{\text{cat,s}}$) with a lower degree of solvation.

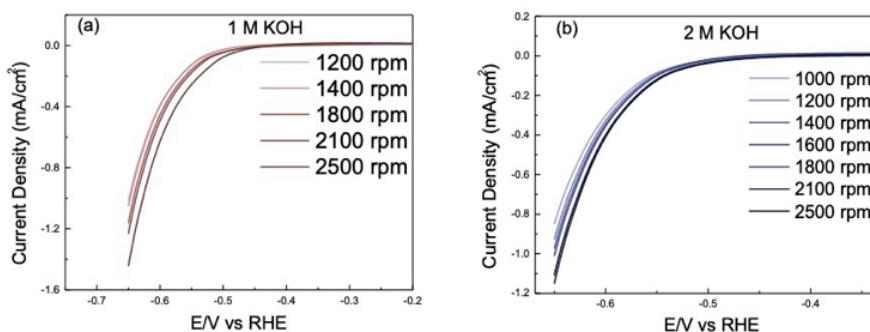


Figure 5 Negative going scan of the cyclic voltammograms obtained for HER on Au polycrystalline surface in (a) 1 M KOH (pH 14) and (b) 2 M KOH at different rotation rates at a scan rate of 25 mVs^{-1} . In contrast to Fig. 4 and S3, under these conditions we find that the HER increases with increasing rotation rate, in agreement with the idea that we are in the concentration regime where cation inhibit the HER.

Moreover, in Fig. 4, we plot the reaction order for HER in bulk cation concentration for different alkali metal cations, at pH 11 and at pH 13, respectively. At pH 11 the positive reaction order in cation concentration increases in going from $\text{Li}^+ < \text{Na}^+ < \text{K}^+$. This agrees with our hypothesis that the effective near-surface concentration of the cations depends on their hydration energy and hence, the increase in the reaction order can be attributed to the corresponding increase in the near-surface “double-layer” cation concentration in going from Li^+ to K^+ . Interestingly, we see that the reaction orders for all the cations are less than 1, which indicates that the inner-layer cation concentration is approaching saturation already at intermediate pH values. Furthermore, at pH 13, we see that while in Li^+ ion containing electrolytes the reaction order in cation concentration (≈ 0.3) is similar to the reaction order observed at pH 11, in Na^+ and K^+ containing electrolytes, the reaction orders become negative. Moreover, the reaction order is more negative for K^+ than it is for Na^+ . In fact, a closer look at the Na^+ ion containing electrolyte at pH 13 (Figure 3e) shows that while an initial increase in the cation concentration shows a near-zero reaction order

for HER, only at higher cation concentrations the reaction order becomes negative (also see Figure S2b in Appendix C) while in the case of K^+ ion containing electrolyte, a purely negative reaction order (Figure 3f) is obtained. These results show that as the bulk electrolyte pH, and thus, the near surface cation concentration increases, above a threshold (saturation) concentration, the promotional effect of the cations on the HER kinetics vanishes and effectively becomes inhibitive at very high cation concentrations. Traditionally, negative reaction orders above a threshold concentration are attributed to the blocking of the reactive sites at the surface. However, it remains an active area of debate in the field whether the cations chemically adsorb at the surface or simply accumulate in the outer-Helmholtz plane in the double layer.^{12, 24, 35} In either case, it would be expected that the accumulated cations near the surface can result in detrimental effects for HER if the cation-metal interactions are boosted at the expense of water-metal interactions. This hypothesis also explains the stronger "blocking" effect at pH 13 in K^+ ion containing electrolytes compared to Li^+ and Na^+ ion containing electrolytes, since Li^+ cations have the weakest interaction with the metal surface due to their higher degree of solvation.^{20-21, 24} Hence, these results suggest that intermediate electrolyte pH is optimal for the cation assisted HER mechanism in alkaline media and more extreme near-surface cation concentrations at very high pH can lead to a diminishing HER activity as the strong cation-metal interactions render the metal surface less active for HER. Since at extremely high pH values, K^+ ions show a negative reaction order for HER (Fig. 3f), we also looked at the rotation rate dependence of HER in 1 M and 2 M KOH containing electrolytes (Fig. 5). Interestingly, in contrast with the results obtained at lower pH values, we observe that under these conditions, an increasing rotation rate results in increasing HER activity in 1 M and 2 M KOH containing electrolytes. Here, the reversed rotation rate dependence confirms that at extremely high bulk pH/cation concentration values, an increasing near surface cation concentration ($[Cat^+]_s$) indeed inhibits HER. And hence, lowering the local pH and thereby the local cation concentration enhances the HER rate. In the current model eqns.(1) and (2) this effect can be modeled by assuming a negative γ , i.e. a negative reaction order in local cation concentration.²³ However, we also note here that the reversed rotation dependence (Fig. 5) is not as prominent as the inhibitive effect of cations obtained with increasing bulk cation concentration (Fig. 3e and 3f) and we believe that this is because while the mass transport changes can regulate the local cation concentration at the interface, in order to obtain the reversed rotation dependence we have to employ very high bulk pH/cation concentration (pH 14; 1 M) to begin with. Hence, even at the highest rotation rate (2500 rpm) the local pH/cation concentration is close to pH 14/ 1 M and therefore, a drastic improvement in the HER activity would not be expected.

4.4. Simulations from the analytical model for HER on Au electrodes

In this section, we present the simulated J - E curves as well as the calculated surface pH and surface cation concentration thus obtained from the eqns. written above and compare them to the experimentally observed trends

(see section S1 in Appendix C for more details). The model is based on the idea that the rate of HER depends on the local (interfacial) concentration of cations, since the cations interact favorably with the transition state because a (partially) negatively hydroxide is being split off from the reacting water molecule, which is written analytically in the form of eqn. 1 above. Moreover, the conservation of electro-neutrality within the diffusion layer dictates that an increase in the concentration of OH^- at the surface must be accompanied by a corresponding increase in the concentration of cations. Hence, the rotation rate/mass transport rate dependence of the diffusion layer thickness (δ ; calculated from the Levich eqn.) indirectly affects the near-surface cation concentration by controlling the local pH at the surface. We note here, that we make certain simplifying approximations in the model (see section S1 in Appendix C for more details) and the aim here is not to reproduce our experimental results quantitatively, but rather to capture the mass transport dependence of HER qualitatively.

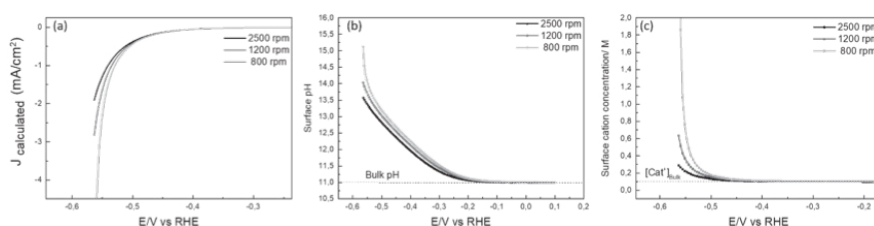


Figure 6 (a) Simulated linear sweep voltammogram for HER on Au electrodes as obtained from eqn. S12 (Appendix C) at different rotation rates (2500 rpm, 1200 rpm and 800 rpm). (b) The as calculated surface pH (eqn. S11) as a function of the applied overpotential (vs RHE) at different rotation rates, where the bulk pH is 11 in all the calculations. (c) The as calculated surface cation concentration (eqn. S7) as a function of the applied overpotential (vs RHE) at different rotation rates, where the bulk cation concentration is 0.1 M in all the calculations.

Fig. 6a illustrates that, in agreement with our experimental results, the simulated curves indeed show an increase in the HER current densities with decreasing rotation rate. Here, the increase in the local pH with the decreasing rotation rate (Fig. 6b) results in a corresponding increase in the local cation concentration (Fig. 6c) which in turn leads to the increase in $J_{\text{calculated}}$ with decreasing rotation. Hence, the simplified eqns. written on the basis of electroneutrality are able to qualitatively capture our experimental results in the low pH/cation concentration regime (pH = 11).

4.5. Conclusions

This work has explored the nature of mass transport effects in tuning the kinetics of HER on polycrystalline Au electrodes. We show that the HER kinetics can be selectively steered by tuning the mass transport rate, for achieving optimal near surface electrochemical environment for HER. It is shown that with the decreasing rotation speed of the electrode (increasing diffusion layer thickness) HER activity can be selectively enhanced on polycrystalline Au electrodes. This enhancement arises from the associated changes in the cation concentration near the interface, which is responding to local changes in OH^- concentration to conserve electroneutrality, as the rotation rate (local pH) is changed. This is because near surface cation

concentration is a central parameter in tuning the HER kinetics in alkaline media and we propose that cations assist in the HER mechanism by stabilizing the dissociating water molecule at the surface ($*\text{H}-\text{OH}^{\delta-}-\text{cat}^+$). Moreover, we also developed an analytical model based on electroneutrality that qualitatively captures the observed mass transport dependence of HER as an implicit function of its near-surface cation concentration dependence. Lastly, we show that the HER kinetics also improves as the bulk electrolyte pH is increased (pH 10 to pH 13) as well as with a change in the alkali metal cation identity in the electrolyte ($\text{Li}^+ < \text{Na}^+ < \text{K}^+$). We show that both of these trends are also correlated to the increase in the near surface cation concentration, which results in the enhancement of HER. In agreement with our previous work, we show that as the electrolyte pH increases, the near surface cation concentration also increases due to the changing interfacial electric field. Moreover, as we go from Li^+ to K^+ , the double-layer cation concentration increases due to the changing solvation energy of the cations. Interestingly, the promotional effect of cations saturates above a threshold concentration and even becomes inhibitive at extreme conditions (high bulk cation concentration and low rotation at high bulk pH). We attribute this inhibitive effect to the crowding of the double layer with extremely high near-surface cation concentrations, which can in turn lead to the crowding/blocking of the reactive sites for HER. This has interesting implications for the alkaline water electrolyzers, as it suggests that superior HER activity can be obtained at intermediate pH values with high ionic strength electrolytes instead of using the highly corrosive extremely alkaline conditions. Moreover, our results also suggest that depending on the strength of metal-water interactions vs metal-cation interactions, divergent HER activity trends can be obtained for the same electrolyte parameters. Hence, it is important to probe the different electrode-electrolyte combinations independently in order to assess the optimal reactions conditions for HER in alkaline media on a given catalyst.

Acknowledgements

This work is part of the Advanced Research Center for Chemical Building Blocks (ARC CBBC) consortium, co-financed by the Netherlands Organization for Scientific Research (NWO) and Shell Global Solutions International B.V.

References

1. Firouzjaie, H. A.; Mustain, W. E., Catalytic Advantages, Challenges, and Priorities in Alkaline Membrane Fuel Cells. *ACS Catalysis* **2020**, *10* (1), 225-234.
2. Anantharaj, S.; Noda, S.; Jothi, V. R.; Yi, S.; Driess, M.; Menezes, P. W., Strategies and Perspectives to Catch the Missing Pieces in Energy-Efficient Hydrogen Evolution Reaction in Alkaline Media. *Angewandte Chemie International Edition n/a* (n/a).
3. Goyal, A.; Marcandalli, G.; Mints, V. A.; Koper, M. T. M., Competition between CO_2 Reduction and Hydrogen Evolution on a Gold Electrode under Well-Defined Mass Transport Conditions. *Journal of the American Chemical Society* **2020**, *142* (9), 4154-4161.

4. Bondue, C. J.; Graf, M.; Goyal, A.; Koper, M. T. M., Suppression of Hydrogen Evolution in Acidic Electrolytes by Electrochemical CO₂ Reduction. *Journal of the American Chemical Society* **2021**, *143* (1), 279-285.
5. Li, K.; Sun, Y., Electrocatalytic Upgrading of Biomass-Derived Intermediate Compounds to Value-Added Products. *Chemistry – A European Journal* **2018**, *24* (69), 18258-18270.
6. Bondue, C. J.; Koper, M. T. M., Electrochemical Reduction of the Carbonyl Functional Group: The Importance of Adsorption Geometry, Molecular Structure, and Electrode Surface Structure. *Journal of the American Chemical Society* **2019**, *141* (30), 12071-12078.
7. Sanyal, U.; Lopez-Ruiz, J.; Padmaperuma, A. B.; Holladay, J.; Gutiérrez, O. Y., Electrocatalytic Hydrogenation of Oxygenated Compounds in Aqueous Phase. *Organic Process Research & Development* **2018**, *22* (12), 1590-1598.
8. Pentland, N.; Bockris, J. O. M.; Sheldon, E., Hydrogen Evolution Reaction on Copper, Gold, Molybdenum, Palladium, Rhodium, and Iron. *Journal of The Electrochemical Society* **1957**, *104* (3), 182.
9. Zheng, J.; Sheng, W.; Zhuang, Z.; Xu, B.; Yan, Y., Universal dependence of hydrogen oxidation and evolution reaction activity of platinum-group metals on pH and hydrogen binding energy. *Science Advances* **2016**, *2* (3), e1501602.
10. Trasatti, S., Work function, electronegativity, and electrochemical behaviour of metals: III. Electrolytic hydrogen evolution in acid solutions. *Journal of Electroanalytical Chemistry and Interfacial Electrochemistry* **1972**, *39* (1), 163-184.
11. Parsons, R., The rate of electrolytic hydrogen evolution and the heat of adsorption of hydrogen. *Transactions of the Faraday Society* **1958**, *54* (0), 1053-1063.
12. Rebollar, L.; Intikhab, S.; Oliveira, N. J.; Yan, Y.; Xu, B.; McCrum, I. T.; Snyder, J. D.; Tang, M. H., "Beyond Adsorption" Descriptors in Hydrogen Electrocatalysis. *ACS Catalysis* **2020**, *10* (24), 14747-14762.
13. Subbaraman, R.; Tripkovic, D.; Strmcnik, D.; Chang, K.-C.; Uchimura, M.; Paulikas, A. P.; Stamenkovic, V.; Markovic, N. M., Enhancing Hydrogen Evolution Activity in Water Splitting by Tailoring Li⁺-Ni(OH)₂-Pt Interfaces. *Science* **2011**, *334* (6060), 1256-1260.
14. Ledezma-Yanez, I.; Wallace, W. D. Z.; Sebastián-Pascual, P.; Climent, V.; Feliu, J. M.; Koper, M. T. M., Interfacial water reorganization as a pH-dependent descriptor of the hydrogen evolution rate on platinum electrodes. *Nature Energy* **2017**, *2*, 17031.
15. McCrum, I. T.; Koper, M. T. M., The role of adsorbed hydroxide in hydrogen evolution reaction kinetics on modified platinum. *Nature Energy* **2020**, *5* (11), 891-899.
16. Rebollar, L.; Intikhab, S.; Snyder, J. D.; Tang, M. H., Kinetic Isotope Effects Quantify pH-Sensitive Water Dynamics at the Pt Electrode Interface. *The Journal of Physical Chemistry Letters* **2020**, *11* (6), 2308-2313.
17. Strmcnik, D.; Kodama, K.; van der Vliet, D.; Greeley, J.; Stamenkovic, V. R.; Marković, N. M., The role of non-covalent interactions in electrocatalytic fuel-cell reactions on platinum. *Nature Chemistry* **2009**, *1* (6), 466-472.
18. Strmcnik, D.; Uchimura, M.; Wang, C.; Subbaraman, R.; Danilovic, N.; van der Vliet, D.; Paulikas, A. P.; Stamenkovic, V. R.; Markovic, N. M., Improving the hydrogen oxidation reaction rate by promotion of hydroxyl adsorption. *Nature Chemistry* **2013**, *5* (4), 300-306.
19. Rebollar, L.; Intikhab, S.; Snyder, J. D.; Tang, M. H., Determining the Viability of Hydroxide-Mediated Bifunctional HER/HOR Mechanisms through Single-

Crystal Voltammetry and Microkinetic Modeling. *Journal of the Electrochemical Society* **2018**, *165* (15), J3209-J3221.

20. Chen, X.; McCrum, I. T.; Schwarz, K. A.; Janik, M. J.; Koper, M. T. M., Co-adsorption of Cations as the Cause of the Apparent pH Dependence of Hydrogen Adsorption on a Stepped Platinum Single-Crystal Electrode. *Angewandte Chemie International Edition* **2017**, *56* (47), 15025-15029.

21. McCrum, I. T.; Janik, M. J., pH and Alkali Cation Effects on the Pt Cyclic Voltammogram Explained Using Density Functional Theory. *The Journal of Physical Chemistry C* **2016**, *120* (1), 457-471.

22. Xue, S.; Garlyyev, B.; Watzele, S.; Liang, Y.; Fichtner, J.; Pohl, M. D.; Bandarenka, A. S., Influence of Alkali Metal Cations on the Hydrogen Evolution Reaction Activity of Pt, Ir, Au, and Ag Electrodes in Alkaline Electrolytes. *ChemElectroChem* **2018**, *5* (17), 2326-2329.

23. Goyal, A.; Koper, M. T. M., The Interrelated Effect of Cations and Electrolyte pH on the Hydrogen Evolution Reaction on Gold Electrodes in Alkaline Media. *Angewandte Chemie International Edition* **2021**, *60* (24), 13452-13462.

24. Mills, J. N.; McCrum, I. T.; Janik, M. J., Alkali cation specific adsorption onto fcc(111) transition metal electrodes. *Physical Chemistry Chemical Physics* **2014**, *16* (27), 13699-13707.

25. Łukaszewski, M.; Soszko, M.; Czerwiński, A., Electrochemical Methods of Real Surface Area Determination of Noble Metal Electrodes – an Overview. *International Journal of Electrochemical Science* **2016**, *11*, 4442-4469.

26. Katsounaros, I.; Meier, J. C.; Klemm, S. O.; Topalov, A. A.; Biedermann, P. U.; Auinger, M.; Mayrhofer, K. J. J., The effective surface pH during reactions at the solid-liquid interface. *Electrochemistry Communications* **2011**, *13* (6), 634-637.

27. Ooka, H.; Figueiredo, M. C.; Koper, M. T. M., Competition between Hydrogen Evolution and Carbon Dioxide Reduction on Copper Electrodes in Mildly Acidic Media. *Langmuir* **2017**, *33* (37), 9307-9313.

28. Monteiro, M. C. O.; Jacobse, L.; Touzalin, T.; Koper, M. T. M., Mediator-Free SECM for Probing the Diffusion Layer pH with Functionalized Gold Ultramicroelectrodes. *Analytical Chemistry* **2020**, *92* (2), 2237-2243.

29. Marcandalli, G.; Goyal, A.; Koper, M. T. M., Electrolyte Effects on the Faradaic Efficiency of CO₂ Reduction to CO on a Gold Electrode. *ACS Catalysis* **2021**, *11* (9), 4936-4945.

30. Sebastian, P.; Martinez-Hincapie, R.; Climent, V.; Feliu, J. M., Study of the Pt (111) vertical bar electrolyte interface in the region close to neutral pH solutions by the laser induced temperature jump technique. *Electrochimica Acta* **2017**, *228*, 667-676.

31. Ganassin, A.; Sebastián, P.; Climent, V.; Schuhmann, W.; Bandarenka, A. S.; Feliu, J., On the pH Dependence of the Potential of Maximum Entropy of Ir(111) Electrodes. *Scientific Reports* **2017**, *7* (1), 1246.

32. Monteiro, M. C. O.; Datilla, F.; Hagedoorn, B.; García-Muelas, R.; López, N.; Koper, M. T. M., Absence of CO₂ electroreduction on copper, gold and silver electrodes without cations in solution. *Nature Catalysis* **2021**, *Accepted*.

33. Xue, S.; Garlyyev, B.; Auer, A.; Kunze-Liebhäuser, J.; Bandarenka, A. S., How the Nature of the Alkali Metal Cations Influences the Double-Layer Capacitance of Cu, Au, and Pt Single-Crystal Electrodes. *The Journal of Physical Chemistry C* **2020**, *124* (23), 12442-12447.

34. Garlyyev, B.; Xue, S.; Watzele, S.; Scieszka, D.; Bandarenka, A. S., Influence of the Nature of the Alkali Metal Cations on the Electrical Double-Layer

Capacitance of Model Pt(111) and Au(111) Electrodes. *The Journal of Physical Chemistry Letters* **2018**, 9 (8), 1927-1930.

35. Ringe, S.; Clark, E. L.; Resasco, J.; Walton, A.; Seger, B.; Bell, A. T.; Chan, K., Understanding cation effects in electrochemical CO₂ reduction. *Energy & Environmental Science* **2019**, 12 (10), 3001-3014.



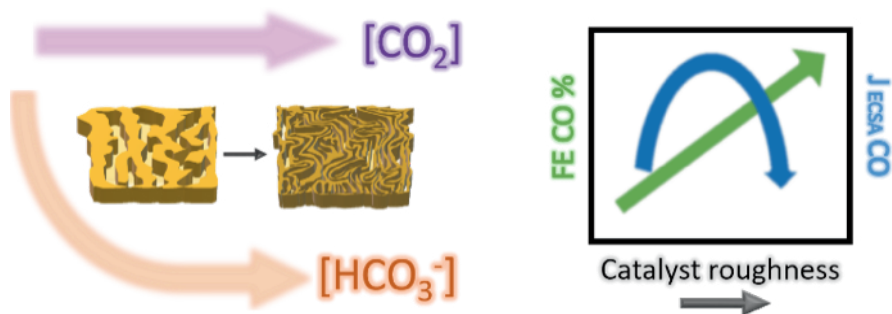
Chapter 5

Effect of pore diameter and length on electrochemical CO_2 reduction reaction at nanoporous gold catalysts



Abstract

In this work, we employ differential electrochemical mass spectrometry (DEMS) to track the real-time evolution of CO at nanoporous gold (NpAu) catalysts with varying pore parameters (diameter and length) during the electrochemical CO₂ reduction reaction (CO₂RR). We show that due to the increase in the local pH with increasing catalyst roughness, NpAu catalysts suppress bicarbonate-mediated hydrogen evolution reaction (HER) compared to a flat Au electrode. Additionally, the geometric current density for CO₂RR increases with the roughness of NpAu catalysts, which we attribute to the increased availability of active sites at NpAu catalysts. Together, the enhancement of CO₂RR and the suppression of competing HER results in a drastic increase in the Faradaic selectivity for CO₂RR with increasing pore length and decreasing pore diameter, reaching near 100% Faradaic efficiency for CO in the most extreme case. Interestingly, unlike the geometric current density, the specific current density for CO₂RR has a more complicated relation with the roughness of the NpAu catalysts. We show that this is due to the presence of Ohmic drop effects along the length of the porous channels. These Ohmic drop effects render the pores partially electrocatalytically inactive and hence, they play an important role in tuning the CO₂RR activity on nanoporous catalysts.



This chapter is based on the submitted manuscript:

Goyal, A.; Bondü, C. J.; Graf, M.; Koper, M. T. M., Effect of pore diameter and length on electrochemical CO₂ reduction reaction at nanoporous gold catalysts. *Chemical Science (Submitted)*

5.1. Introduction

Electrochemical reduction of CO₂ (CO₂RR) can be used to achieve a carbon-neutral energy cycle wherein carbon-based fuels can be produced with net zero emissions by using renewable electricity.¹⁻³ However, at present, the economic feasibility of this reaction remains an issue, primarily due to its low energy efficiency in commonly employed bicarbonate electrolytes, especially at high current densities.⁴⁻⁵ Consequently, significant research efforts have been made towards optimizing the catalyst design as well as the reaction process conditions for achieving better CO₂RR selectivities.⁶⁻⁹ Recently, meso- or nanoporous electrocatalyst materials have emerged as an interesting strategy to tune the selectivity of CO₂RR. To this end, most of the research has focused on the effect intrinsic properties of nanoporous structures (such as high, potentially active surface area, high relative density of stepped sites and grain boundaries) have on CO₂RR activity.¹⁰⁻¹⁵ However, the effect of porosity towards tuning the local reaction environment by regulating the near-surface concentration of different reactive species (such as CO₂, HCO₃⁻ and OH⁻) has received less scrutiny. Given that local concentration gradients play a significant role in tuning the competition between CO₂RR and the parasitic hydrogen evolution reaction (HER) on flat polycrystalline electrodes,^{8, 16-17} it can be expected that the mass transport limitations introduced by confinement effects in and around the nanoporous channels will also affect the competition between these two reactions.¹⁸⁻²⁰

In this respect, some recent studies have indeed emphasized the importance of local diffusional gradients in tuning the CO₂RR activity on nanoporous electrodes.²¹⁻²⁵ In general, it has been shown that with the increasing roughness/thickness of the nanoporous catalysts, the local pH at the surface also increases, resulting in the suppression of bicarbonate-mediated HER reaction ($\text{HCO}_3^- + 2e^- \rightarrow \text{H}_2 + 2\text{CO}_3^{2-}$). However, conflicting results have been obtained on the effect of local concentration gradients in tuning the rate of CO₂RR reaction on nanoporous catalysts. Surendranath and co-workers have shown the formation rate of CO on nanoporous gold (NpAu) is largely independent of the catalyst's pore dimensions, which they attributed to negligible concentration gradient for CO₂ between the bulk environment to the surface due to its slow acid-base equilibria in the electrolyte.^{22, 26} However, in the case of nanoporous silver catalysts, the same authors observe that increasing catalyst layer thickness results in higher partial current densities for CO₂RR.²¹ Meanwhile, Atwater and co-workers have observed a similar enhancement in the rate of CO₂RR in the case of NpAu catalysts, which they attributed to the presence of grain boundaries on nanoporous electrodes.²⁴ On the other hand, in a similar study, Cheng and co-workers have found the opposite effect of catalyst size on CO₂RR and attributed this to the decreasing solubility of CO₂ with increasing local pH at the surface.²⁵

One of the complications in unambiguously elucidating the role of nanoporous catalysts in tuning the activity of the electrocatalytic reactions (CO₂RR and HER) arises from the ancillary participation of homogenous acid-base equilibria ($\text{CO}_2(\text{aq.}) + \text{OH}^- \leftrightarrow \text{HCO}_3^-$; $\text{HCO}_3^- + \text{OH}^- \leftrightarrow \text{CO}_3^{2-} + \text{H}_2\text{O}$)

in regulating the local concentration gradients at the catalyst surface.²⁷⁻²⁹ Consequently, different concentration gradients can be generated near similar catalysts due to the convoluted interplay between the homogenous reactions, mass transport, and the heterogeneous reactions, especially in the case of long-term bulk electrolysis measurements.³⁰ Hence, in order to more reliably disentangle these effects, it is imperative to track the real-time evolution of the reaction products as well as the local concentration gradients by using an online detection technique. Moreover, cell geometries with well-defined mass transport conditions are also desirable in order to avoid the time-dependent concentration polarization effects.³¹ To circumvent these issues, we have recently developed two online methods, namely, a gold ring based rotating ring disk electrode (RRDE) technique and an online differential electrochemical mass spectrometry (DEMS) technique based on a dual thin-layer flow cell, for the quantitative detection of CO during CO₂RR under well-defined mass transport conditions.^{8, 17, 32-33}

In this paper, we present a study on the role of pore parameters (diameter and length) in tuning the competition between CO₂RR and HER on nanoporous Au (NpAu) catalysts by using our DEMS technique. We find that with decreasing pore diameter and increasing pore length the Faradaic selectivity for CO₂RR increases dramatically (up to ~100%), even under sub-optimal reaction conditions (0.5 atm. CO₂ in 0.1 M NaHCO₃ plus 0.4 M NaClO₄). We show that this enhancement arises due to two factors: (i) the suppression of bicarbonate mediated HER reaction with increasing local pH at the catalyst surface and (ii) the enhancement of CO₂RR at NpAu catalysts due to the increased availability of active sites with increasing catalyst roughness. Moreover, we show that the Ohmic drop effects across the porous channels play an important role in tuning the obtained specific current densities for CO₂RR as they render the pores partially inactive towards electrocatalysis. Hence, by using the online DEMS technique, we elucidate the convoluted interplay between catalyst geometry effects and local concentration gradient effects in tuning the activity/selectivity of CO₂RR at nanoporous catalysts.

5.2. Experimental section

5.2.1. Chemicals

The electrolytes were prepared from H₂SO₄ (98% by wt. solution, EMSURE, Merck), NaHCO₃ (≥ 99.7%, Honeywell Fluka), NaClO₄ (99.99%, trace metals basis, Sigma-Aldrich), NaH₂PO₄ (≥ 99.0%, EMSURE, Merck), Na₂HPO₄ (≥ 99.0%, EMSURE, Merck) and Ultrapure water (MilliQ gradient, ≥18.2 MΩcm, TOC < 5 ppb). CO (4.7 purity, Linde), Ar (6.0 purity, Linde) and CO₂ (4.5 purity, Linde) were used for purging the electrolytes. To prepare the nanoporous Au (NpAu) catalysts, KAu(CN)₂ (99.95 %, trace metals basis, Sigma-Aldrich), KAg(CN)₂ (Sigma-Aldrich), Na₂CO₃ (≥ 99.5%, Sigma-Aldrich) and HClO₄ (60% by wt. solution, EMSURE, Merck) were used.

5.2.2. NpAu catalyst synthesis and characterization

Before each experiment, the substrate electrode (polycrystalline Au) was mechanically polished on Buehler micro-polishing cloth (8 inches) with decreasing sizes of diamond polishing suspension, namely, 3 μm, 1 μm and 0.25 μm. Next, it was sonicated in ultrapure water and acetone for 10 minutes to remove any organic/inorganic impurities. Thereafter, the NpAu catalyst layer was formed on the substrate electrode by following the electrochemical alloying-dealloying procedure outlined previously.³⁴⁻³⁶ Briefly, a binary alloy solution of 5:1 ratio of Ag/Au was prepared with KAg(CN)₂ and KAu(CN)₂ in 0.25 M Na₂CO₃ buffer solution and it was potentiostatically electrodeposited onto the flat Au substrate electrode at -1.2 V (vs Ag/AgCl) for 9 min. Thereafter, Ag was de-alloyed from the film by electrochemically cycling (20 cycles) the electrode in 1 M HClO₄ solution between 1.05 V to 1.2 V (vs Ag/AgCl) at 5 mVs⁻¹. The as-prepared NpAu catalyst (referred to as "NpAu4") was thermally coarsened to obtain varying pore diameter and height, at 523.15 K, for 120 sec., 60 sec. and 30 sec. to form NpAu1, NpAu2 and NpAu3, respectively. To avoid faulty activity measurements due to any residual CO₂ in the pores, a new catalyst layer was prepared for each measurement. To determine the roughness factor of the catalysts, electrochemical characterization was performed in 0.1 M H₂SO₄ (0.05 V to 1.75 V vs RHE at a scan rate of 50 mV s⁻¹) to obtain the electrochemically active surface area (ECSA) of the catalyst by calculating the charge from the reduction peak for the Au oxide in the characterization CV and dividing it by the specific charge of one monolayer of Au (390 μC cm⁻²).³⁷

The morphology and the composition of the different NpAu catalysts was checked by using the ETD detector (for SEM imaging) and the EDS detector (for Energy Dispersive X-ray Spectroscopy) of Apreo SEM (Thermo Scientific), respectively. After the electrochemical measurements, the NpAu samples were rinsed with MilliQ water and upon drying placed on a custom-made SEM holder for analysis.

5.2.3. Differential electrochemical mass spectrometry (DEMS) measurements

All the electrochemical measurements were performed with a home-built DEMS set-up (described in detail elsewhere).³² The ionization potential of the ion source of the mass spectrometer was set to -27.5 V (vs the potential of the formation room and +72.5 V vs ground) to circumvent the fragmentation of CO₂ at mass 28 (CO⁺) which allowed for the ionic signal at mass 28 to be used for the quantitative detection of CO formed during CO₂RR.³² To achieve well-defined mass transport conditions during the CO₂RR studies, a dual thin layer cell with a flow cell geometry was used (described in detail elsewhere).³⁸ We note here that for all the CO₂RR measurements, instead of using CO₂ saturated conditions, we employed a 1:1 (vol.) ratio of Ar/CO₂. This was done in order to prevent bubble attachment in the microfluidic channels of the dual thin layer cell, which becomes unavoidable when high concentration of hydrophobic CO₂ is dissolved in the electrolyte, as it tends to salt out in the thin channels of the cell body (made of Kel-F) over the course of the measurements.¹⁷ Hence for

all the CO₂RR measurements, an Ar/CO₂ saturated electrolyte (0.1 M NaHCO₃ plus 0.4 M NaClO₄ or 0.1 M NaHCO₃ plus 2 M NaClO₄) was introduced into the top (electrochemical) compartment of the cell where the working electrode (NpAu or Flat Au) was placed. For all the CO₂RR studies, the cyclic voltammograms were recorded between -0.75 V and -1.2 V vs normal hydrogen electrode (NHE; where a Ag/AgCl reference was used in all the measurements and the potentials were converted to the NHE scale afterwards) at a scan rate of 5 mVs⁻¹. The flow of the electrolyte (5 μLs⁻¹) through the cell was achieved with a syringe pump which swept the electrolyte (along with the electrochemical products and the unreacted analyte) from the top compartment to the bottom compartment of the cell which was interfaced with the vacuum of the mass spectrometer with the help of a porous Teflon membrane and a porous steel frit. The products of HER and CO₂RR were detected at the ionic signal at m/z 2 (H₂) and m/z 28 (CO), respectively. The ionic current obtained with the DEMS is related to the molar flux of the species by eqn. 1:

$$I_{\text{ionic}(i)} = \frac{dn(i)}{dt} \times K^* \quad (1)$$

where, $I_{\text{ionic}(i)}$ is the ionic current due to a species i , $\frac{dn(i)}{dt}$ is the molar flux of i into the mass spectrometer and K^* is a proportionality constant that reflects the sensitivity of the DEMS setup for i , which among other things is dependent on the ionization probability of i .³⁹ Here, the molar flux $\frac{dn(i)}{dt}$ is associated to the Faradaic current $I_{\text{Faradaic}(i)}$ by Faraday's law:

$$\frac{dn(i)}{dt} = \frac{I_{\text{Faradaic}(i)} \times N}{zF} \quad (2)$$

where N is the transfer efficiency of species i in a given cell geometry/assembly, z is the number of electrons involved in the electrochemical reaction and F is Faraday's constant. By substituting eqn. 2 into eqn. 1, we obtain:

$$I_{\text{ionic}(i)} = \frac{I_{\text{Faradaic}(i)} \times K^\circ}{zF} \quad (3)$$

where $K^\circ = K^* \times N$ is the cell calibration constant. In order to quantify the ionic signals, in every new cell assembly, calibration measurements need to be performed to determine the value of the calibration constant (K°) for H₂ and CO, respectively. For the calibration of H₂, measurements were performed under Ar saturated conditions with a blank electrolyte (0.1 M phosphate buffer and 0.4 M NaClO₄), as shown in Fig. S1a of Appendix D, where H₂ was evolved with 100% Faradaic efficiency (scan window of -0.6 V to -1.8 V vs Ag/AgCl at a scan rate of 5 mVs⁻¹). Using eqn. 3, $K_{\text{H}_2}^\circ$ was determined $\left(K_{\text{H}_2}^\circ = \frac{I_{\text{ionic}(\text{H}_2)} \times zF}{I_{\text{Faradaic}(\text{HER})}} \right)$. For the calibration of CO, bulk CO oxidation was performed under CO saturated conditions with a blank electrolyte (0.1

M phosphate buffer and 0.4 M NaClO₄), as shown in Fig. S1b in Appendix D, where CO₂ was evolved with 100% Faradaic efficiency (scan window of -0.6 V to 0.5 V vs Ag/AgCl at a scan rate of 5 mVs⁻¹). Using eqn. 3, K_{CO}° was determined ($K_{CO}^{\circ} = \frac{I_{\text{ionic}}(\text{CO}) \times zF}{I_{\text{Faradaic}}(\text{CO ox.})}$). Next, the ionic signals obtained at mass 2 and mass 28 during CO₂RR measurements could be used to calculate the partial current densities for H₂ and CO formation from eqn. 3. The Faradaic selectivity for CO₂RR and HER could then be calculated as follows:

$$FE_{\text{CO}_2\text{RR}} = \frac{I_{\text{Faradaic}}(\text{CO}) \times 100}{(I_{\text{Faradaic}}(\text{CO}) + I_{\text{Faradaic}}(\text{H}_2))} = \frac{I_{\text{Faradaic}}(\text{CO})}{I_{\text{Measured}}} \times 100 \quad (4)$$

and,

$$FE_{\text{HER}} = \frac{I_{\text{Faradaic}}(\text{H}_2) \times 100}{(I_{\text{Faradaic}}(\text{CO}) + I_{\text{Faradaic}}(\text{H}_2))} = \frac{I_{\text{Faradaic}}(\text{H}_2)}{I_{\text{Measured}}} \times 100 = 100 - FE_{\text{CO}_2\text{RR}} \quad (5)$$

In summary, by determining the calibration constants ($K_{H_2}^{\circ}$ and K_{CO}°), the online DEMS technique can be used for quantitatively studying CO₂RR on NpAu catalysts.

5.3. Results and discussion

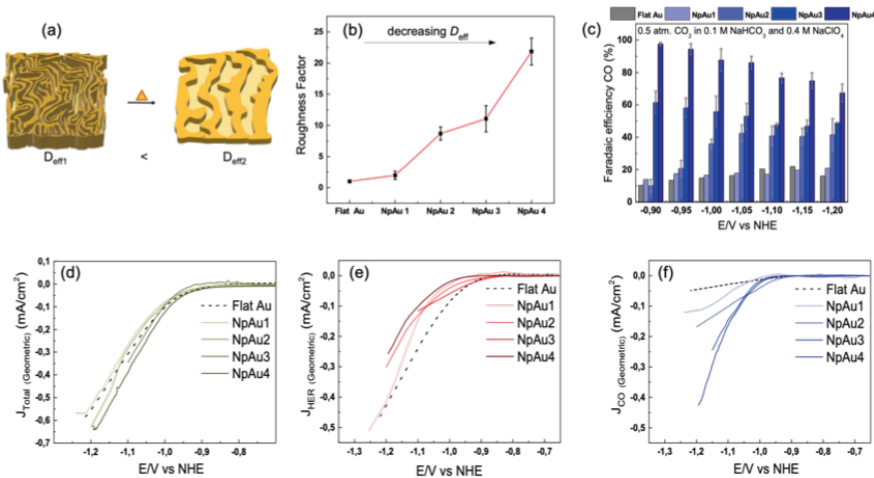


Figure 6 (a) Schematic representation of NpAu catalysts illustrating how thermal coarsening results in the self-similar growth of the NpAu ligaments such that the pore diameter increases and the effective pore length decreases with increasing coarsening. This also results in a decreasing effective diffusive flow (D_{eff}) through the porous channels. (b) Roughness factors of different Au catalysts as determined by the ECSA values obtained from Fig. S2 (Appendix D), where D_{eff} decreases with increasing roughness. (c) Faradaic efficiency for CO formation on the different Au catalysts at different potentials (vs. NHE), as obtained from the DEMS measurements by using eqn. 4. (d) Total geometric current density on different Au catalysts during CO₂RR, (e) Partial geometric current density for HER

on different Au catalysts obtained from the ionic current at m/z 2 by using eqn. 3 and (f) Partial geometric current density for CO formation on different Au catalysts obtained from the ionic current at m/z 28 by using eqn. 3. All the measurements were done in 0.5 atm. CO_2 in 0.1 M NaHCO_3 plus 0.4 M NaClO_4 containing electrolyte with a scan rate of 5 mVs^{-1} and a flow rate of $300 \mu\text{Lmin}^{-1}$.

In this work we studied the role of pore parameters (diameter and length) in tuning the activity/selectivity of electrochemical CO_2 reduction reaction (CO2RR). For this we prepared four different nanoporous Au (NpAu) samples via an electrochemical alloying-dealloying and subsequent thermal coarsening procedure, as outlined in section 2.2. Electrochemical characterization (see Fig. S2 in Appendix D) and scanning electron microscopy (SEM) images (see Fig. S3 in Appendix D) show that the thermal treatment of the NpAu samples results in the systematic decrease of the ligament diameter of the porous network. Moreover, in accordance with the previous studies,^{34-36, 40} we expect that thermal coarsening of the NpAu samples results in a more or less self-similar growth of the porous structures, i.e. an increase in the pore/ligament diameter and a corresponding decrease in pore length (also shown in Fig. 1a). Thus, in going from NpAu1 to NpAu4 the pore diameter decreases and the pore length increases. This in turn leads to decreasing effective diffusion (D_{eff}) through the porous channels due to the generation of additional diffusional gradients along the length of the pores.⁴¹ In Fig. 1b, we show the roughness factor of the different NpAu catalysts with respect to the polycrystalline Au electrode (Flat Au), calculated by using the as-determined ECSA (shown in Fig. S2 in Appendix D) of the different surfaces. As expected, the roughness factor of the catalyst surface increases with decreasing thermal coarsening. We note here that in all the NpAu samples, we detect around 7 atomic-% of residual Ag with EDX spectroscopy (shown in Fig. S3 in Appendix D). Thereafter, we studied CO2RR at these catalysts by using the online DEMS, where the ionic signals at m/z 2 and 28 were used to quantify the amount of H_2 and CO, respectively, evolved during CO2RR on the different catalyst surfaces (for further details see section 2.3). In Fig. 1c, we show the Faradaic efficiency for CO2RR on the different Au catalysts as derived from the DEMS measurements by using eqn. 4. In agreement with the previous studies on nanoporous Au catalysts,^{17, 22, 24} we see that the Faradaic efficiency for CO2RR increases with increasing roughness factor of the catalysts, i.e. with decreasing pore diameter and increasing pore length (Flat Au < NpAu1 < NpAu2 < NpAu3 < NpAu4). Remarkably, in the case of NpAu4, we achieve ~100% Faradaic efficiency for CO2RR even with 0.5 atm. of CO_2 . Here, the sub-optimal reaction conditions for CO2RR (0.5 atm. of CO_2 instead of 1 atm. CO_2) also explain the uncharacteristically low Faradaic efficiency for CO in the case of flat polycrystalline Au (Flat Au) catalyst. We note that in addition to the low partial pressure of CO_2 , the high Na^+ ion concentration in the electrolyte also contributes to a lower Faradaic selectivity towards CO2RR. We have shown previously with our RRDE technique that with increasing cation concentration in the electrolyte (at a fixed bicarbonate concentration) the Faradaic efficiency towards CO2RR decreases on flat Au polycrystalline electrodes.^{8, 33} In that work we achieved Faradaic selectivities close to 60% in 1 atm. CO_2 with 0.5 M Na^+ ion

containing electrolytes.³³ Hence, the Faradaic efficiency of around 20% in the case of flat Au catalysts (as shown in Fig. 1c) can be attributed to the combination of low CO₂ partial pressure (0.5 atm.) and a high cation concentration in the electrolyte (0.5 M) in our measurements.

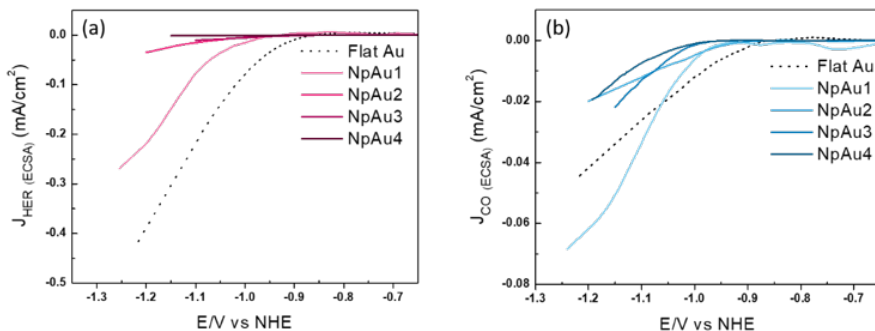


Figure 2 (a) Partial specific current density for HER on different Au catalysts (obtained from the data used in Fig. 1e) and (b) Partial specific current density for CO formation on different Au catalysts (obtained from the data used in Fig. 1f). All the measurements were done in 0.5 atm. CO₂ in 0.1 M NaHCO₃ plus 0.4 M NaClO₄ containing electrolyte with a scan rate of 5 mVs⁻¹ and a flow rate of 300 μLmin⁻¹.

In Fig. 1d, we plot the experimentally measured total geometric current density, and in Figs. 1e and 1f we plot the corresponding partial geometric current densities for HER and CO₂RR calculated from the ionic currents measured at mass 2 and 28, respectively. We see that the geometric current density for HER decreases in going from Flat Au to NpAu4 (as shown in Fig. 1e) and hence, the enhancement in the CO₂RR Faradaic efficiency with the increasing roughness of the NpAu catalysts can, at least in part, be attributed to the suppression of competing HER reaction.^{21-22, 25} We have shown previously with the RRDE technique^{8, 33} that in bicarbonate containing electrolytes, HER can either be mediated by HCO₃⁻ ions (eqn. 6) or by H₂O molecules (eqn. 7):



and that these two branches show a divergent dependence on electrolyte pH. It was observed that while HER due to the discharge of HCO₃⁻ ions decreased with increasing pH, for water reduction reaction the opposite takes place.^{8, 42} Moreover, the branch of HER that competes with CO₂RR is largely dependent on the identity of the electrolyte that is employed in the measurements. In brief, the dominating branch of HER switches from water-mediated to HCO₃⁻-mediated with increasing bicarbonate/cation concentration in the electrolyte.^{8, 33} In accordance with these results, under the experimental conditions of our measurements (0.1 M NaHCO₃ plus 0.4 M NaClO₄) we expect bicarbonate mediated HER to be the main branch of hydrogen evolution that competes with CO₂RR.

Moreover, we expect the partial current due to HER to be sensitive to the local pH which, among other things, is determined by the morphology of the electrode surface. In the case of nanoporous catalysts, with increasing catalyst roughness, the effective diffusion through the porous channels will decrease. As a result, the local pH will increase at the catalyst surface due to the hindered mass transport of locally generated OH^- ions away from the electrode and at the same time, due to the hindered mass transport of HCO_3^- ions and CO_2 (aq.) to the surface. Hence, we attribute the decreasing HER activity with increasing catalyst roughness, as observed in Fig. 1e, to the corresponding increase in local pH in going from Flat Au to NpAu4. This is because the increasing local alkalinity accelerates the homogeneous consumption of bicarbonate near the electrode surface:



which in turn leads to a paucity of HCO_3^- ions for participating in the HER reaction.⁸ We note here that the partial current density for HER decreases both with respect to the geometric surface area (Fig. 1e) and with respect to the ECSA of the catalysts (Fig. 2a).

On the other hand, for CO₂RR, we see that the partial geometric current density increases with increasing pore length and decreasing pore diameter i.e. with increasing catalyst roughness, as shown in Fig. 1f. This is partially counter-intuitive since increasing local pH at the catalyst surface should also lead to a corresponding increase in the homogeneous consumption of CO_2 :



Hence, similar to HER, we would expect that increasing local pH due to increasing catalyst roughness will result in the suppression of CO₂RR. However, we see the opposite trend in Fig. 1f. This can be rationalized by the fact that the rate of homogeneous CO_2 consumption ($k_{\text{q}}^+ = 2.23 \times 10^3 \text{ Kg mol}^{-1} \text{ s}^{-1}$) is six orders of magnitude slower than the rate of homogeneous HCO_3^- consumption ($k_{\text{q}}^+ = 6 \times 10^9 \text{ Kg mol}^{-1} \text{ s}^{-1}$).^{27, 43} Consequently, the mass transport rate of CO_2 (aq.) to the interface can outpace the rate of its homogeneous reaction, especially under the conditions of convection control (e.g. rotation control, flow control).

To validate this further, we performed measurements where the different NpAu catalysts were first exposed to a CO_2 -saturated electrolyte and thereafter, currents due to CO formation were measured under Ar-saturated conditions (shown in Fig. 3). Interestingly, we see that all the NpAu catalysts show appreciable currents due to CO formation even in the absence of a continuous CO_2 supply (Fig. 3a). Moreover, these currents persist after ten subsequent scans (Fig. 3b) even on the catalyst with the highest roughness factor (NpAu4). Together, these results show that despite the increasing mass transport limitations and with this an increasing local alkalinity in the porous channels, NpAu catalysts are able to furnish an appreciable reservoir of CO_2 . Moreover, the local CO_2 reservoir is able to take part in CO₂RR without completely getting homogeneously consumed. In fact, with

increasing catalyst roughness we obtain higher currents for CO formation (Fig. 3a), thus indicating that with increasing pore length we generate a larger CO₂ reservoir at the catalyst surface.

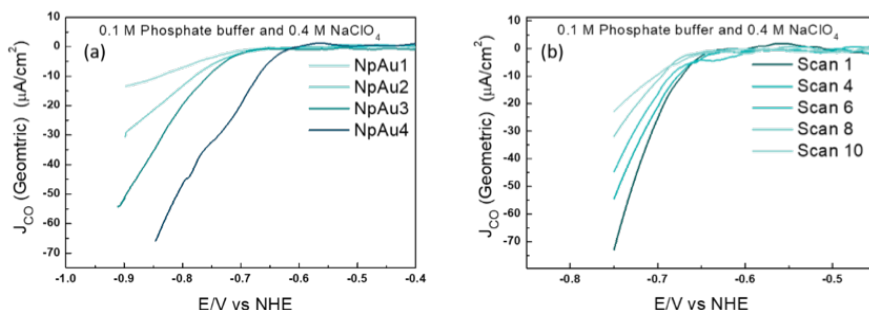


Figure 3 (a) Partial geometric current density for CO formation on different Au catalysts (Flat Au, NpAu1, NpAu2, NpAu3 and NpAu4) where the dual thin layer cell (along with the catalysts) was first flushed with a CO₂ sat. 0.1 M Phosphate buffer plus 0.4 M NaClO₄ containing electrolyte; the measurements were done in Ar sat. conditions (with the same electrolyte) after flushing the cell with Ar sat. electrolyte for 10 min. and in (b) the 10 subsequent scans under the same experimental conditions described above on NpAu4 catalyst. Scan rate: 5 mVs⁻¹ and flow rate: 300 $\mu Lmin^{-1}$.

In Table S1 (Appendix D), we give calculated theoretical currents as limited by mass transport for CO₂RR and they are much larger than the experimentally obtained current densities on any of the catalysts employed in our measurements (see Fig. 1f). This shows that under the flow conditions of our measurements (300 $\mu L min^{-1}$), we are below any mass transport limitations for CO₂RR. Hence, the slow homogenous reaction of CO₂ and the lack of any mass transport limitation for CO₂RR explains why the CO₂RR current density does not decrease in going from Flat Au to NpAu4. On the other hand, the availability of electrochemically active sites at the catalyst surface increases with increasing catalyst roughness, as a higher surface roughness automatically comes with more surface defects which are commonly considered sites of increased reactivity. Together, the increase in the number of active sites and/or increased surface defects explains the observed enhancement in CO₂RR current density with increasing catalyst roughness.

Interestingly, unlike HER, we see diverging trends when the partial geometric current density (current with respect to the geometric surface area) and partial specific current density (current with respect to the ECSA) for CO₂RR are compared. In Fig. 2b we plot the partial specific current density for CO₂RR and we see that while it increases in going from Flat Au to NpAu1, a further increase in the catalyst roughness results in a lower specific current density for CO₂RR, with no clear trend between NpAu2 to NpAu4. Given that the CO₂RR activity is tied to the availability of active sites at the catalyst surface, the fact that it scales with the geometric surface area (Fig. 1f) but does not scale with the ECSA (Fig. 2b) suggests that not the entire surface of the NpAu catalysts participates in electrocatalysis.

This is understandable because the thin porous channels of NpAu catalysts generate an additional electrical resistance which scales with increasing pore length.⁴⁴⁻⁴⁵ As shown in Fig. 4a, at the orifices of the porous sample an

Ohmic drop originates solely due to the electrolyte resistance (R_{sol}) which can be mitigated by positive feedback compensation. However, the distributed capacitance (C) and the charge transfer resistance (R_{ct}) that represent the electrocatalytic reaction at the interface are coupled to additional uncompensated resistance (r_{pore}) along the length of the pores. This means that there is an additional barrier for the current to pass through the pores. Hence, with increasing distance from the orifice it becomes more difficult for the porous channels to participate in the Faradaic reaction. Essentially, these cumulative uncompensated Ohmic drop effects can result in an electrocatalytically inactive zone at the bottom of the porous channels which results in the decoupling of the ECSA and the specific activity at these catalysts. Hence, the observed trend for the partial specific CO₂RR current density as a function of the catalyst roughness (shown in Fig. 2b) can be attributed to the fact that the increasing availability of active sites for CO₂RR from Flat Au to NpAu4 catalysts, is countered by a corresponding increase in the Ohmic drop effects with increasing pore length. As a result, while at relatively low catalyst roughness (NpAu1; Fig. 2b) the increased availability of the active sites overshadows these Ohmic drop effects, as the catalyst roughness (pore length) increases further and Ohmic drop effects dominate the overall activity for CO₂RR at NpAu catalysts.

In order to validate the presence of the Ohmic drop effects at NpAu catalysts, we performed additional CO₂RR measurements (shown in Fig. 4) by increasing the supporting electrolyte concentration in the system. Since increasing supporting electrolyte concentration will increase the conductivity of the electrolyte, it should result in a proportional decrease in the Ohmic drop (r_{pore}) along the porous channels. Hence, we would expect the partial specific current density for CO₂RR to increase with increasing ionic strength of the electrolyte at NpAu catalysts.

The results in Fig. 4 confirm this expectation: on all the NpAu catalysts (Fig. 4d and 4f) the partial specific current density for CO₂RR increases with increasing concentration of the supporting electrolyte, while on flat Au catalysts, the partial current density for CO₂RR slightly decreases with the increasing ionic strength (Fig. 4b). This confirms that Ohmic drop effects along the porous channels play a significant role in determining the obtained specific current densities for CO₂RR on NpAu catalysts.

Notably, the presence of these Ohmic drop effects on NpAu catalysts also implies even though the total amount of CO₂ inside the pores increases with increasing pore size, this CO₂ does not necessarily react everywhere within the pore. Because it takes longer for CO₂ to diffuse out of a more porous electrode, this "unreacted" CO₂ can lead to an enhanced current for CO₂RR under non-steady-state conditions, until the pores are depleted of CO₂ (as is the case in the results shown in Fig. 3b). Hence, it should be kept in mind that this local CO₂ reservoir can affect the observed CO₂RR activities on NpAu catalysts, however it is a non-steady-state effect.

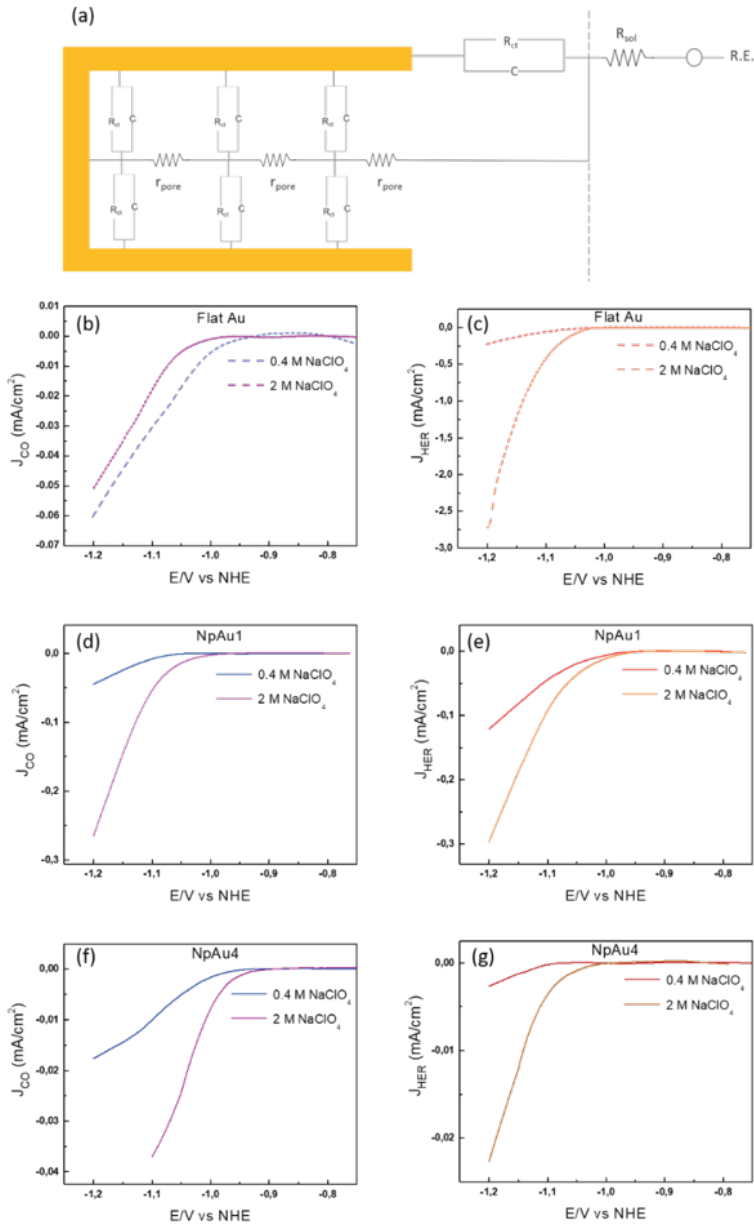


Figure 4 (a) Schematic representation of the circuit at NpAu catalysts where R_{sol} is the solution resistance between the reference electrode and the working electrode, R_{ct} , C are the distributed charge transfer resistance and the distributed capacitance associated with the Faradaic reaction at the catalyst surface and r_{pore} is the distributed resistance of the pore per unit length and per unit surface area of the porous film. Partial specific current density for CO formation as obtained from the ionic current at m/z 28 by using eqn. 3 with 0.5 atm. CO₂ in 0.1 M NaHCO₃ plus 0.4 M NaClO₄ containing electrolyte (blue) and in 0.1 M NaHCO₃ plus 2 M NaClO₄ containing electrolyte (pink) on (b) Flat Au, (d) NpAu1 and (f) NpAu 4. Partial current density for HER as obtained from the ionic current at m/z 2 by using eqn. 3 with 0.5 atm. CO₂ in 0.1 M NaHCO₃ plus 0.4 M NaClO₄ containing electrolyte (red) and in 0.1 M NaHCO₃ plus 2 M NaClO₄ containing electrolyte (orange) on (c) Flat Au, (e) NpAu1 and (g) NpAu 4. Scan rate: 5 mV s⁻¹ and flow rate: 300 μ L min⁻¹.

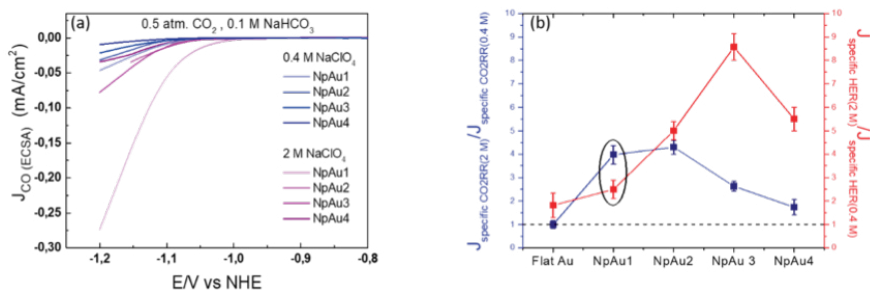


Figure 5 (a) Comparison of the partial specific current density for CO formation on different NpAu catalysts (NpAu1 to NpAu4) as obtained from the ionic current at m/z 28 by using eqn. 3 with 0.5 atm. CO₂ and 0.1 M NaHCO₃ in 0.4 M NaClO₄ (blue) and 2 M NaClO₄ (pink) containing electrolyte at a scan rate of 5 mVs⁻¹ and a flow rate of 300 $\mu\text{L min}^{-1}$. (b) Ratio of the specific current density in 2 M NaClO₄ containing electrolyte and 0.4 M NaClO₄ containing electrolyte at a fixed NaHCO₃ (0.1 M) concentration towards CO₂RR (blue) and HER (red) at -1.2 V vs NHE on different Au catalysts. Here a ratio greater than 1 indicates a higher specific current density in 2 M NaClO₄ containing electrolyte compared to 0.4 M NaClO₄ containing electrolyte.

Moreover, we note that unlike CO₂RR, the HER activity increases with increasing concentration of the supporting electrolyte (Fig. 4c, 4e and 4f) regardless of the catalyst surface. This agrees with our previous studies on flat polycrystalline Au electrodes where we have shown that HER shows a positive reaction order for the cation concentration in the electrolyte. In that work we ascribed this to the changes in the double layer composition with changing cation concentration in the electrolyte.^{33, 42} Moreover, in agreement with the current study, we also observed near-zero reaction order in cation concentration for CO₂RR at flat polycrystalline Au electrodes, which we ascribed to the enhancement of HER at the expense of CO₂RR with the increasing cation concentration in the electrolyte.³³

Additionally, in Fig. 5a we plot the partial specific current density for CO₂RR on the different Au catalysts in 0.4 M and 2 M NaClO₄ containing electrolyte and we see that while in the case of NpAu1, the increasing ionic strength of the electrolyte is able to compensate for the Ohmic drop effects completely, for the other NpAu catalysts, only a slight improvement is observed. This shows that by increasing the total ionic strength of the electrolyte from 0.6 M to 2.1 M we are still not able to completely compensate for the Ohmic drop effects, especially in catalysts with higher roughness factors. Nevertheless, increasing the ionic strength of the electrolyte does improve the obtained specific current density for CO₂RR on all the NpAu catalysts. Importantly, there is a trade-off here between the increase in the CO₂RR activity (specific current density) and CO₂RR selectivity (Faradaic efficiency) with the increasing ionic strength of the electrolyte. As shown in Fig. 5b, the enhancement in the HER activity with increasing ionic strength overshadows the enhancement in the CO₂RR activity on all the catalysts except NpAu1. This is also reflected in the Faradaic selectivity for CO₂RR, as shown in Fig. 6, where we see that except NpAu1, in all the other NpAu catalysts, the Faradaic selectivity towards CO₂RR decreases with increasing ionic strength of the electrolyte. Hence, these results show that we can partially compensate for the Ohmic drop effects occurring inside nanoporous

catalysts by increasing the supporting electrolyte concentration which enables higher CO₂RR activity. However, depending on the roughness/porosity of the catalysts, the concomitant enhancement of the competing HER reaction with increasing cation concentration in the electrolyte can overshadow the enhancement in the CO₂RR activity, which may therefore result in a lower Faradaic selectivity for CO₂RR.

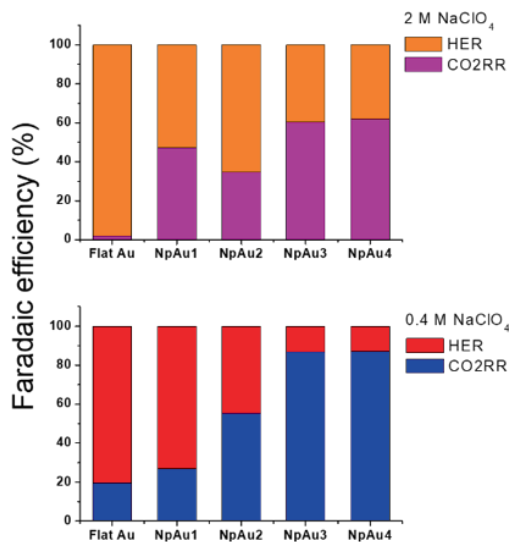


Figure 6 Comparison of the Faradaic efficiency for CO₂RR and HER in 2 M NaClO₄ containing electrolyte (top panel) and 0.4 M NaClO₄ containing electrolyte (bottom panel) at a fixed NaHCO₃ concentration (0.1 M) at -1 V vs NHE in 0.5 atm. CO₂.

5.4. Conclusions

We studied the role of pore parameters (diameter and pore length) in tuning CO₂RR on nanoporous Au (NpAu) catalysts by using the online DEMS technique. We find a higher CO₂RR Faradaic selectivity is achieved with increasingly narrower and longer pores (increasing catalyst roughness), and in the most extreme case (NpAu4) we achieve near 100% efficiency even in an under-saturated CO₂ solution. This enhancement is attributed to two factors, the enhancement of the CO₂RR currents due to the presence of more active sites with increasing catalyst roughness and the suppression of competing HER reaction due to the increasing local pH at the catalyst surface. Interestingly, the partial specific current density for CO₂RR shows a more complicated relationship with catalyst roughness than the partial geometric current density, as it does not scale with increasing catalyst roughness. We show that this is due to the presence of additional Ohmic drop across the length of the thin porous channels which plays an important role in determining the specific activity of nanoporous catalysts.

These results have important implications as they show that with increasing catalyst porosity, there is a trade-off between the number of active sites and the Ohmic drop effects at the catalyst surface. These two effects counter-act each other for tuning the CO₂RR activity. This is relevant as previous studies on nanoporous catalysts have not considered these offsets

and some of the discrepancies in the current literature on the role of pore parameters in tuning CO₂RR activity can be explained by the presence of these counter-acting effects. Additionally, these results also imply that the increase in the local alkalinity due to the generation of OH⁻ ions via CO₂RR and HER, will diminish along the length of the pores due to the increasing Ohmic drop effects. Hence, exclusion of these effects can lead to erroneous estimation/modelling of local pH gradients at the surface of nanoporous catalysts.

In conclusion, this work provides important new insights into the intricate role of local pH gradients and intrinsic geometric effects in tuning the activity/selectivity of CO₂RR at the surface of nonporous Au catalysts and we believe that these insights will be instrumental in the rational optimization of CO₂RR on practical electrode geometries.

Acknowledgements

This work is part of the Advanced Research Center for Chemical Building Blocks (ARC CBBC) consortium, co-financed by the Netherlands Organization for Scientific Research (NWO) and Shell Global Solutions International B.V.

References

1. Nitopi, S.; Bertheussen, E.; Scott, S. B.; Liu, X.; Engstfeld, A. K.; Horch, S.; Seger, B.; Stephens, I. E. L.; Chan, K.; Hahn, C.; Nørskov, J. K.; Jaramillo, T. F.; Chorkendorff, I., Progress and Perspectives of Electrochemical CO₂ Reduction on Copper in Aqueous Electrolyte. *Chemical Reviews* **2019**, *119* (12), 7610-7672.
2. Birdja, Y. Y.; Pérez-Gallent, E.; Figueiredo, M. C.; Göttle, A. J.; Calle-Vallejo, F.; Koper, M. T. M., Advances and challenges in understanding the electrocatalytic conversion of carbon dioxide to fuels. *Nature Energy* **2019**, *4* (9), 732-745.
3. Liu, A.; Gao, M.; Ren, X.; Meng, F.; Yang, Y.; Gao, L.; Yang, Q.; Ma, T., Current progress in electrocatalytic carbon dioxide reduction to fuels on heterogeneous catalysts. *Journal of Materials Chemistry A* **2020**, *8* (7), 3541-3562.
4. Zhao, S.; Jin, R.; Jin, R., Opportunities and Challenges in CO₂ Reduction by Gold- and Silver-Based Electrocatalysts: From Bulk Metals to Nanoparticles and Atomically Precise Nanoclusters. *ACS Energy Letters* **2018**, *3* (2), 452-462.
5. Burdyny, T.; Smith, W. A., CO₂ reduction on gas-diffusion electrodes and why catalytic performance must be assessed at commercially-relevant conditions. *Energy & Environmental Science* **2019**, *12* (5), 1442-1453.
6. Kas, R.; Hummadi, K. K.; Kortlever, R.; de Wit, P.; Milbrat, A.; Luiten-Olieman, M. W. J.; Benes, N. E.; Koper, M. T. M.; Mul, G., Three-dimensional porous hollow fibre copper electrodes for efficient and high-rate electrochemical carbon dioxide reduction. *Nature Communications* **2016**, *7*, 10748.
7. Kas, R.; Kortlever, R.; Yilmaz, H.; Koper, M. T. M.; Mul, G., Manipulating the Hydrocarbon Selectivity of Copper Nanoparticles in CO₂ Electroreduction by Process Conditions. *ChemElectroChem* **2015**, *2* (3), 354-358.
8. Goyal, A.; Marcandalli, G.; Mints, V. A.; Koper, M. T. M., Competition between CO₂ Reduction and Hydrogen Evolution on a Gold Electrode under Well-Defined Mass Transport Conditions. *Journal of the American Chemical Society* **2020**, *142* (9), 4154-4161.
9. Wang, Y.; Liu, J.; Wang, Y.; Al-Enizi, A. M.; Zheng, G., Tuning of CO₂ Reduction Selectivity on Metal Electrocatalysts. *Small* **2017**, *13* (43), 1701809.
10. Zhang, L.; Wang, Z. Y.; Mehio, N. D.; Jin, X. B.; Dai, S., Thickness- and Particle-Size-Dependent Electrochemical Reduction of Carbon Dioxide on Thin-Layer Porous Silver Electrodes. *ChemSusChem* **2016**, *9* (5), 428-432.


11. Lu, Q.; Rosen, J.; Zhou, Y.; Hutchings, G. S.; Kimmel, Y. C.; Chen, J. G.; Jiao, F., A selective and efficient electrocatalyst for carbon dioxide reduction. **2014**, *5*, 3242.
12. Kumar, B.; Atla, V.; Brian, J. P.; Kumari, S.; Nguyen, T. Q.; Sunkara, M.; Spurgeon, J. M., Reduced SnO₂ Porous Nanowires with a High Density of Grain Boundaries as Catalysts for Efficient Electrochemical CO₂-into-HCOOH Conversion. *Angewandte Chemie International Edition* **2017**, *56* (13), 3645-3649.
13. Rosen, J.; Hutchings, G. S.; Lu, Q.; Rivera, S.; Zhou, Y.; Vlachos, D. G.; Jiao, F., Mechanistic Insights into the Electrochemical Reduction of CO₂ to CO on Nanostructured Ag Surfaces. *ACS Catalysis* **2015**, *5* (7), 4293-4299.
14. Jiang, X.; Cai, F.; Gao, D.; Dong, J.; Miao, S.; Wang, G.; Bao, X., Electrocatalytic reduction of carbon dioxide over reduced nanoporous zinc oxide. *Electrochemistry Communications* **2016**, *68* (Supplement C), 67-70.
15. Peng, Y.; Wu, T.; Sun, L.; Nsanzimana, J. M. V.; Fisher, A. C.; Wang, X., Selective Electrochemical Reduction of CO₂ to Ethylene on Nanopores-Modified Copper Electrodes in Aqueous Solution. *ACS Applied Materials & Interfaces* **2017**, *9* (38), 32782-32789.
16. Clark, E. L.; Bell, A. T., Direct Observation of the Local Reaction Environment during the Electrochemical Reduction of CO₂. *Journal of the American Chemical Society* **2018**, *140* (22), 7012-7020.
17. Bondue, C. J.; Graf, M.; Goyal, A.; Koper, M. T. M., Suppression of Hydrogen Evolution in Acidic Electrolytes by Electrochemical CO₂ Reduction. *Journal of the American Chemical Society* **2021**, *143* (1), 279-285.
18. Park, S.; Kim, H. C.; Chung, T. D., Electrochemical analysis based on nanoporous structures. *Analyst* **2012**, *137* (17), 3891-3903.
19. Luc, W.; Jiao, F., Nanoporous Metals as Electrocatalysts: State-of-the-Art, Opportunities, and Challenges. *ACS Catalysis* **2017**, *7* (9), 5856-5861.
20. Galinsky, M.; Chal, U.; Breitung, C., The Impact of Microstructure Geometry on the Mass Transport in Artificial Pores: A Numerical Approach. *Modelling and Simulation in Engineering* **2014**, *2014*, 7.
21. Yoon, Y.; Hall, A. S.; Surendranath, Y., Tuning of Silver Catalyst Mesostructure Promotes Selective Carbon Dioxide Conversion into Fuels. *Angewandte Chemie International Edition* **2016**, *55* (49), 15282-15286.
22. Hall, A. S.; Yoon, Y.; Wuttig, A.; Surendranath, Y., Mesostructure-Induced Selectivity in CO₂ Reduction Catalysis. *Journal of the American Chemical Society* **2015**, *137* (47), 14834-14837.
23. Luo, W.; Zhang, J.; Li, M.; Züttel, A., Boosting CO Production in Electrocatalytic CO₂ Reduction on Highly Porous Zn Catalysts. *ACS Catalysis* **2019**, *9* (5), 3783-3791.
24. Welch, A. J.; DuChene, J. S.; Tagliabue, G.; Davoyan, A.; Cheng, W.-H.; Atwater, H. A., Nanoporous Gold as a Highly Selective and Active Carbon Dioxide Reduction Catalyst. *ACS Applied Energy Materials* **2019**, *2* (1), 164-170.
25. Chen, C.; Zhang, B.; Zhong, J.; Cheng, Z., Selective electrochemical CO₂ reduction over highly porous gold films. *Journal of Materials Chemistry A* **2017**, *5* (41), 21955-21964.
26. Wuttig, A.; Yoon, Y.; Ryu, J.; Surendranath, Y., Bicarbonate Is Not a General Acid in Au-Catalyzed CO₂ Electroreduction. *Journal of the American Chemical Society* **2017**, *139* (47), 17109-17113.
27. Dunwell, M.; Yang, X.; Setzler, B. P.; Anibal, J.; Yan, Y.; Xu, B., Examination of Near-Electrode Concentration Gradients and Kinetic Impacts on the Electrochemical Reduction of CO₂ using Surface-Enhanced Infrared Spectroscopy. *ACS Catalysis* **2018**, *8*, 3999-4008.
28. Dunwell, M.; Lu, Q.; Heyes, J. M.; Rosen, J.; Chen, J. G.; Yan, Y.; Jiao, F.; Xu, B., The Central Role of Bicarbonate in the Electrochemical Reduction of Carbon Dioxide on Gold. *Journal of the American Chemical Society* **2017**, *139* (10), 3774-3783.
29. Wuttig, A.; Yaguchi, M.; Motobayashi, K.; Osawa, M.; Surendranath, Y., Inhibited proton transfer enhances Au-catalyzed CO₂-to-fuels selectivity. *Proceedings of the National Academy of Sciences* **2016**, *113* (32), E4585-E4593.
30. Zhang, B. A.; Ozel, T.; Elias, J. S.; Costentin, C.; Nocera, D. G., Interplay of Homogeneous Reactions, Mass Transport, and Kinetics in Determining Selectivity of the Reduction of CO₂ on Gold Electrodes. *ACS Central Science* **2019**, *5* (6), 1097-1105.

31. Clark, E. L.; Resasco, J.; Landers, A.; Lin, J.; Chung, L.-T.; Walton, A.; Hahn, C.; Jaramillo, T. F.; Bell, A. T., Standards and Protocols for Data Acquisition and Reporting for Studies of the Electrochemical Reduction of Carbon Dioxide. *ACS Catalysis* **2018**, *8* (7), 6560-6570.
32. Bondue, C. J.; Koper, M. T. M., A DEMS approach for the direct detection of CO formed during electrochemical CO₂ reduction. *Journal of Electroanalytical Chemistry* **2020**, 113842.
33. Marcandalli, G.; Goyal, A.; Koper, M. T. M., Electrolyte Effects on the Faradaic Efficiency of CO₂ Reduction to CO on a Gold Electrode. *ACS Catalysis* **2021**, *11* (9), 4936-4945.
34. Graf, M.; Vonbun-Feldbauer, G. B.; Koper, M. T. M., Direct and Broadband Plasmonic Charge Transfer to Enhance Water Oxidation on a Gold Electrode. *ACS Nano* **2021**, *15* (2), 3188-3200.
35. Ji, C.; Searson, P. C., Fabrication of nanoporous gold nanowires. *Applied Physics Letters* **2002**, *81* (23), 4437-4439.
36. Graf, M.; Jalas, D.; Weissmüller, J.; Petrov, A. Y.; Eich, M., Surface-to-Volume Ratio Drives Photoelectron Injection from Nanoscale Gold into Electrolyte. *ACS Catalysis* **2019**, *9* (4), 3366-3374.
37. Łukaszewski, M.; Soszko, M.; Czerwiński, A., Electrochemical Methods of Real Surface Area Determination of Noble Metal Electrodes – an Overview. *International Journal of Electrochemical Science* **2016**, *11*, 4442-4469.
38. Abd-El-Latif, A. A.; Bondue, C. J.; Ernst, S.; Hegemann, M.; Kaul, J. K.; Khodayari, M.; Mostafa, E.; Stefanova, A.; Baltruschat, H., Insights into electrochemical reactions by differential electrochemical mass spectrometry. *TrAC Trends in Analytical Chemistry* **2015**, *70*, 4-13.
39. Baltruschat, H., Differential electrochemical mass spectrometry. *Journal of the American Society for Mass Spectrometry* **2004**, *15* (12), 1693-1706.
40. Ding, Y.; Kim, Y.-J.; Erlebacher, J., Nanoporous Gold Leaf: "Ancient Technology"/Advanced Material. *Advanced Materials* **2004**, *16* (21), 1897-1900.
41. Haensch, M.; Balboa, L.; Graf, M.; Silva Olaya, A. R.; Weissmüller, J.; Wittstock, G., Mass Transport in Porous Electrodes Studied by Scanning Electrochemical Microscopy: Example of Nanoporous Gold. *ChemElectroChem* **2019**, *6* (12), 3160-3166.
42. Goyal, A.; Koper, M. T. M., The Interrelated Effect of Cations and Electrolyte pH on the Hydrogen Evolution Reaction on Gold Electrodes in Alkaline Media. *Angewandte Chemie International Edition* **2021**, *60* (24), 13452-13462.
43. Schulz, K. G.; Riebesell, U.; Rost, B.; Thoms, S.; Zeebe, R. E., Determination of the rate constants for the carbon dioxide to bicarbonate inter-conversion in pH-buffered seawater systems. *Marine Chemistry* **2006**, *100* (1), 53-65.
44. Haverkort, J. W., A theoretical analysis of the optimal electrode thickness and porosity. *Electrochimica Acta* **2019**, *295*, 846-860.
45. Andrieux, C. P.; Costentin, C.; Di Giovanni, C.; Savéant, J.-M.; Tard, C., Conductive Mesoporous Catalytic Films. Current Distortion and Performance Degradation by Dual-Phase Ohmic Drop Effects. Analysis and Remedies. *The Journal of Physical Chemistry C* **2016**, *120* (38), 21263-21271.

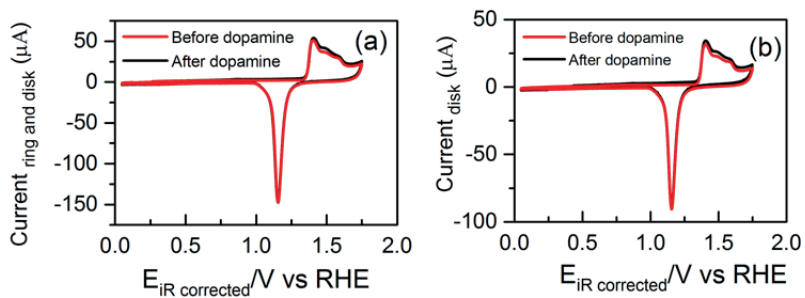


Appendix A

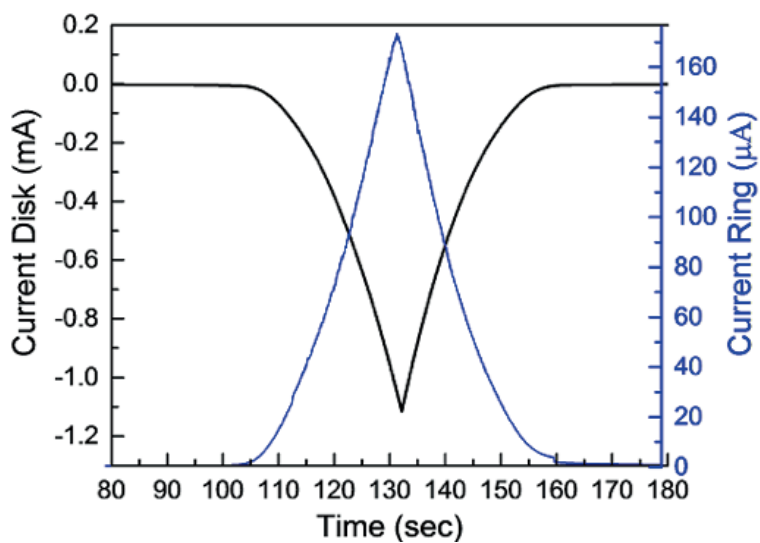
Supporting Information to Chapter 2

The background of the page is a light gray gradient. It features several faint, stylized molecular models scattered across the space. These models consist of small white and gray spheres connected by thin lines, representing atoms and bonds. In the lower right quadrant, there is a prominent white lightning bolt graphic that appears to be striking a cluster of larger, semi-transparent white spheres. The overall aesthetic is clean and scientific.

This is available as the Supporting Information to the article:
Goyal, A.; Marcandalli, G.; Mints, V. A.; Koper, M. T. M., Competition
between CO₂ Reduction and Hydrogen Evolution on a Gold Electrode under
Well-Defined Mass Transport Conditions. *Journal of the American Chemical
Society* **2020**, *142* (9), 4154-416



FigureS1 Characterization CV of (a) Ring and Disk and (b) Disk, in 0.1 M H_2SO_4 , recorded at 50 mVs^{-1} . Red: before dopamine coating. Black: after dopamine coating.



FigureS2 RRDE currents for the Au polycrystalline disk (black) and Au ring (blue) vs time, in CO_2 sat. 0.1 M NaHCO_3 (bulk pH = 6.8), recorded at 25 mVs^{-1} at 800 rpm.

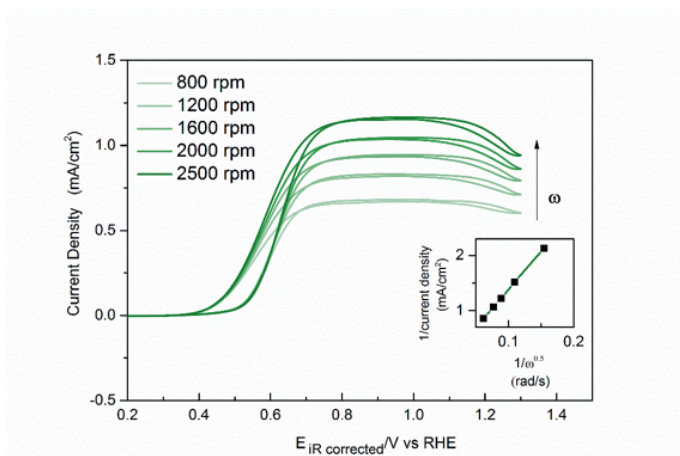


Figure S3 CO oxidation CV on Au polycrystalline surface at different rotation rates in CO sat. 0.1 M NaHCO_3 (bulk pH = 9), recorded at 25 mVs^{-1} from 0.2 V to 1.3 V vs RHE. The direction of the arrow indicates increasing rotation rate. Inset shows the Koutecky-Levich analysis for the CO oxidation currents at 1 V (vs RHE), where the calculated intercept of the line is 0.006.

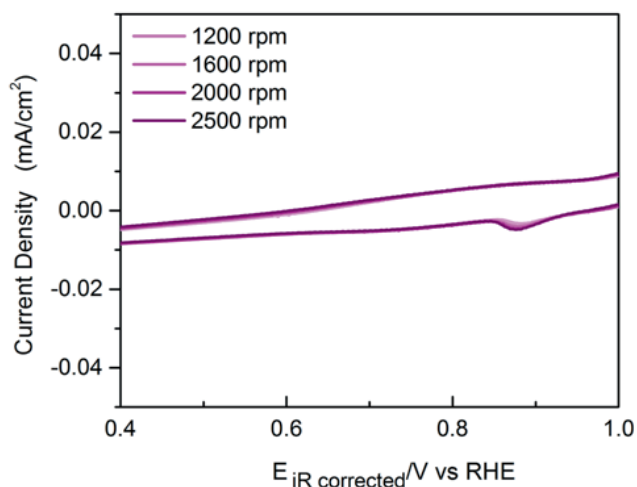


Figure S4 CV for Au polycrystalline surface in H_2 sat. 0.1 M NaHCO_3 (bulk pH = 9) in the potential window of CO oxidation recorded at 25 mVs^{-1} , at different rotation speeds.

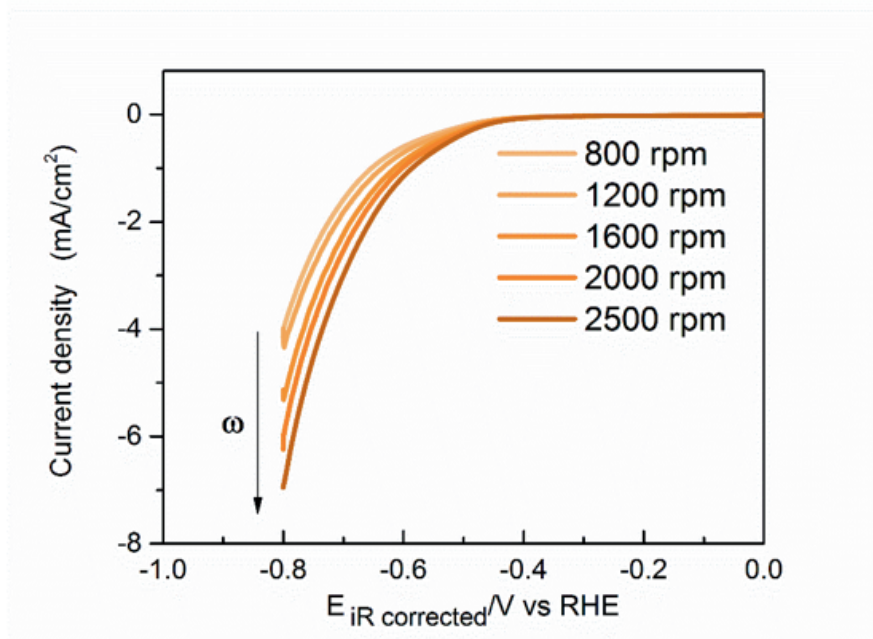


Figure S5 CVs obtained for HER at different rotation rates using the RDE on Au polycrystalline surface in Ar sat. 0.5 M NaHCO₃ at 25 mVs⁻¹. The direction of the arrow indicates increasing rotation rate.

Table S3 Theoretically calculated diffusion limited currents for the two electron CO₂ reduction in the RDE set-up at different rotation rates, by using the Levich equation and Fick's first law of diffusion. Where diffusion coefficient of CO₂ is taken to be 1.6 X 10⁻⁵ cm²/s, the kinematic viscosity of water is taken to be 8.9 X 10⁻³ cm²/s, the Faraday's constant is taken to be 96500 C/mol, the number of electrons involved is taken to be 2 and the concentration of CO₂ in the bulk is taken to be 33 mM.¹⁻²

Rotation speed (rpm)	Diffusion layer thickness (μm)	J limiting theoretical (mA/cm ²)
400	2.7	-36.6
800	1.9	-51.8
1200	1.6	-63.4
1600	1.4	-73.2
2000	1.3	-81.9
2500	1.1	-91.5

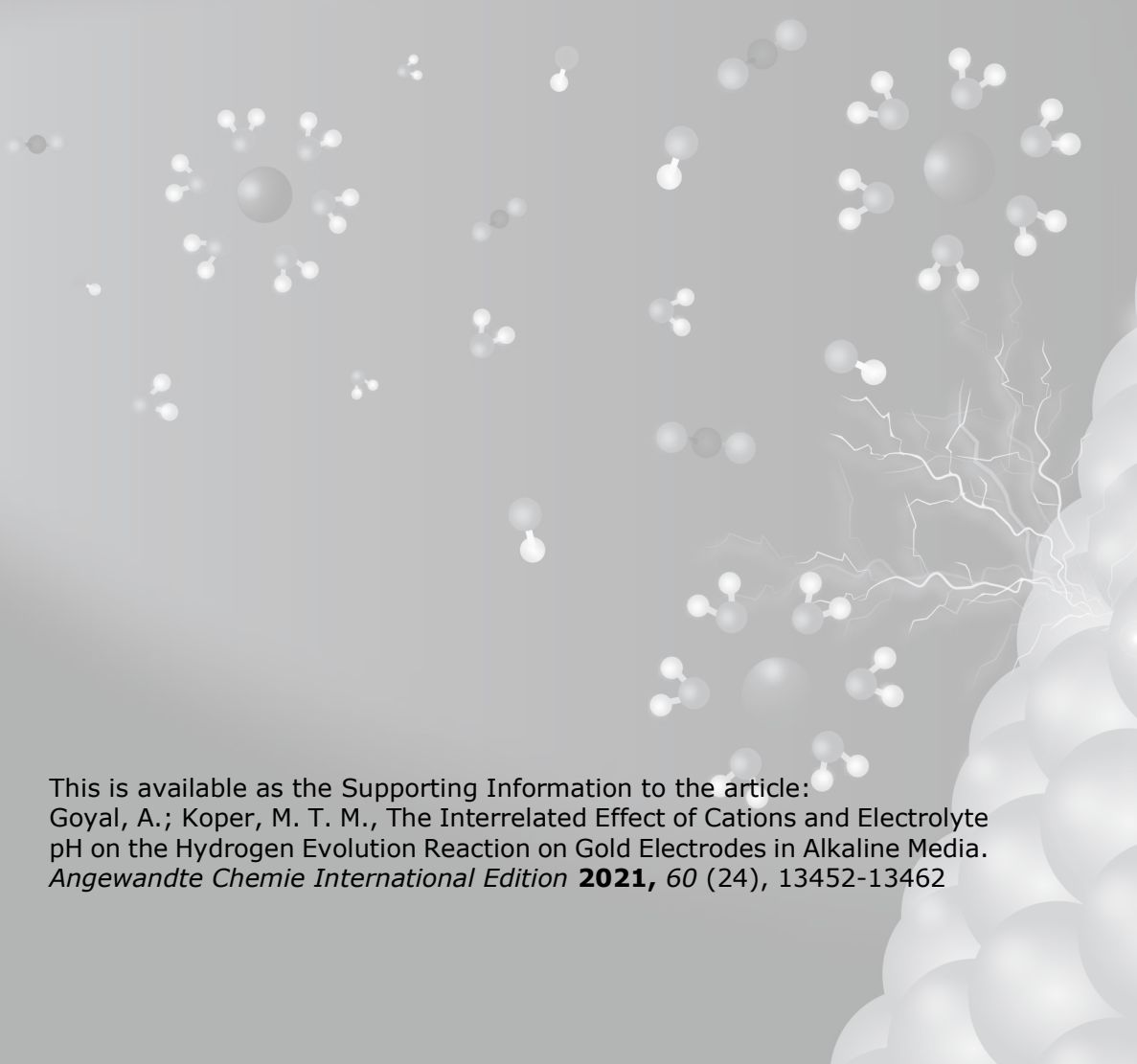
References

- Bard, A. J.; Faulkner, L. R., *Electrochemical methods : fundamentals and applications* Wiley: New York, **1980**.
- Ooka, H.; Figueiredo, M. C.; Koper, M. T. M., Competition between Hydrogen Evolution and Carbon Dioxide Reduction on Copper Electrodes in Mildly Acidic Media. *Langmuir* **2017**, 33 (37), 9307-9313.



Appendix B

Supporting Information to Chapter 3

The background of the page is a light gray gradient. It features several molecular models of water (H2O) and other small molecules scattered across the space. On the right side, there is a stylized white lightning bolt striking a cluster of large, semi-transparent white spheres that resemble a molecular surface or a cluster of atoms.

This is available as the Supporting Information to the article:
Goyal, A.; Koper, M. T. M., The Interrelated Effect of Cations and Electrolyte
pH on the Hydrogen Evolution Reaction on Gold Electrodes in Alkaline Media.
Angewandte Chemie International Edition **2021**, 60 (24), 13452-13462

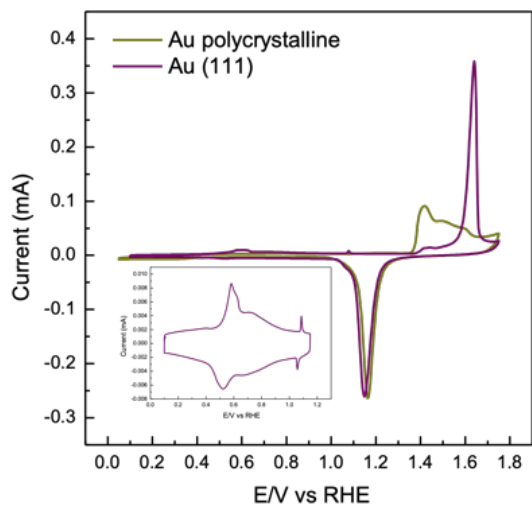


Figure S1 Characteristic cyclic voltammograms for Au polycrystalline surface (golden) and Au(111) surface (purple) obtained in 0.1 M H_2SO_4 in Ar sat. environment at 50 mVs^{-1} . The inset shows the characteristic double-layer features of the Au(111) surface in the potential window of 0.1 V to 1.15 V (vs RHE).

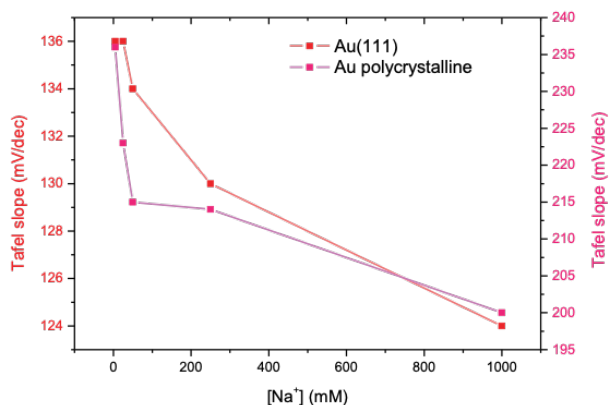


Figure S2 Tafel slopes obtained for Au polycrystalline surface (pink; right hand side on the y-axis) and Au(111) surface (red; left hand side on the y-axis) at pH 11 for different Na^+ cation concentration in the electrolyte (plotted on the x-axis). The data is obtained from the steady-state currents obtained at 50 mV potential steps in the HER region.

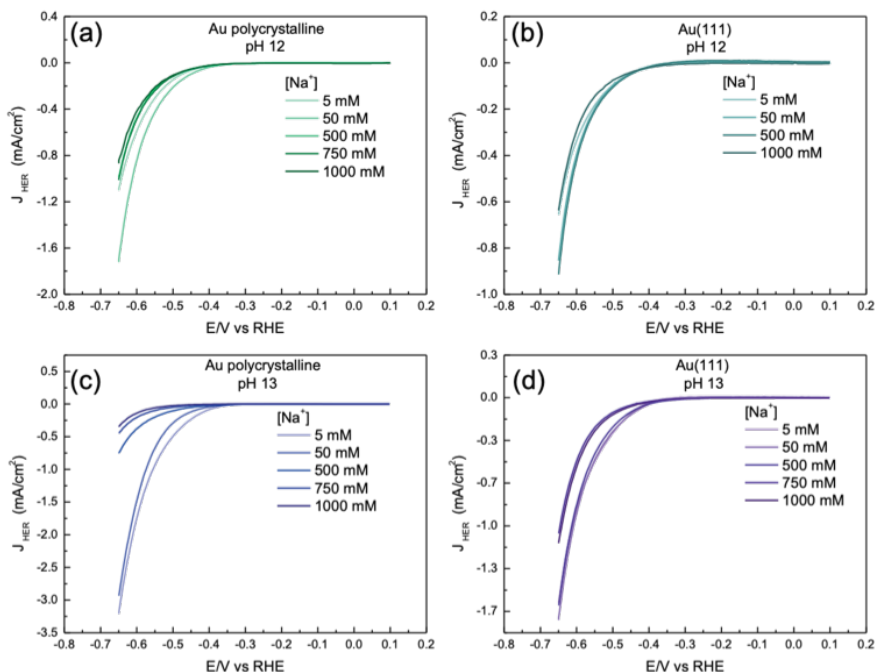


Figure S3 Cyclic voltammograms obtained for HER at pH 12 on (a) Au polycrystalline surface and (b) Au(111) surface and at pH 13 on (c) Au polycrystalline surface and (d) Au(111) surface at 2500 rpm for different concentrations of NaClO₄ (5 mM, 50 mM, 500 mM, 750 mM and 1000 mM) in Ar sat. environment at 25 mVs⁻¹.

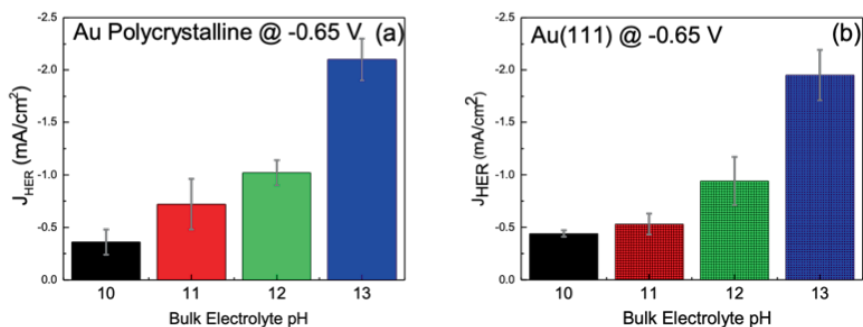


Figure S4 Characteristic current densities obtained for (a) Au polycrystalline surface and (b) Au(111) surface in 0.1 M electrolytes at different bulk pH (pH 10 to pH 13) in Ar sat. environment at - 0.65 V (vs RHE) at 2500 rpm.

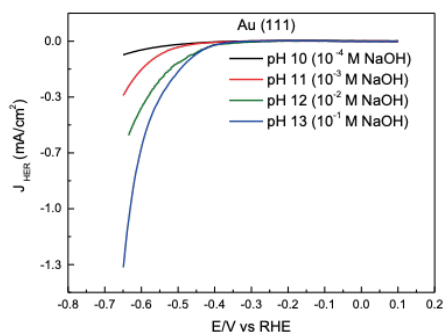


Figure S5 Cyclic voltammograms obtained for HER on Au(111) surface in 0.1 M NaOH (pH 13), 0.01 M NaOH (pH 12), 0.001 M NaOH (pH 11) and 0.0001 M NaOH (pH 10), in Ar sat. environment at 25 mVs^{-1} under stationary hanging meniscus configuration. In these experiments the ionic strength of the electrolyte is not fixed.

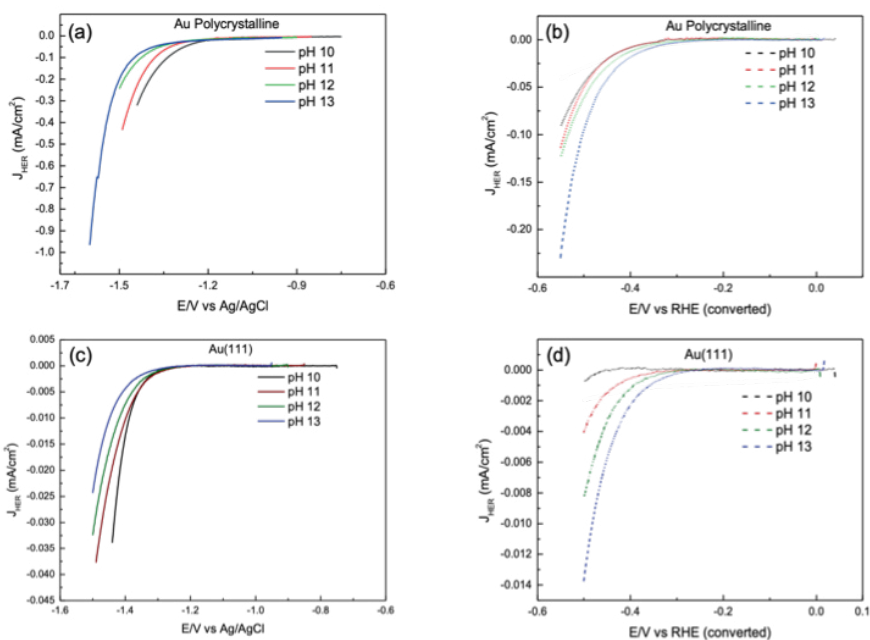


Figure S6 Cyclic voltammograms obtained for HER on (a) Au polycrystalline surface and (c) (d) Au(111) surface at 2500 rpm in 0.1 M NaOH (pH 13), 0.01 M NaOH + 0.09 M NaClO₄ (pH 12), 0.001 M NaOH + 0.099 M NaClO₄ (pH 11) and 0.0001 M NaOH + 0.0999 M NaClO₄ (pH 10), in Ar sat. environment at 25 mVs^{-1} with a Ag/AgCl reference and in (b), (d) the data is plotted on the RHE scale where the potentials are converted post experiment from (a) and (c) respectively.

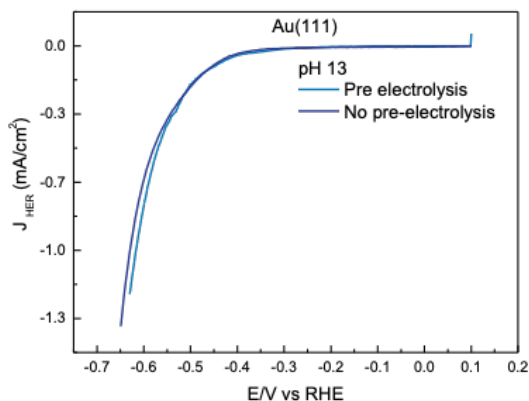


Figure S7 Comparison of the cyclic voltammograms obtained for HER on Au(111) surface in the pre-electrolyzed electrolyte (light blue) and non-pre-electrolyzed electrolyte (dark blue) at pH 13 in Ar sat. environment at 25 mVs^{-1} .

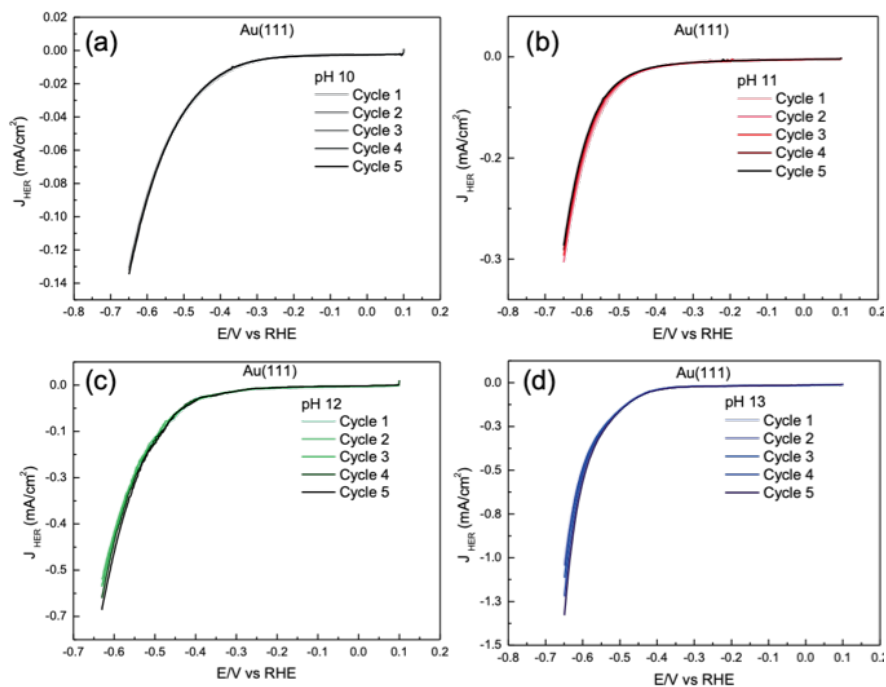


Figure S8 First five cycles of the cyclic voltammograms obtained for HER on Au(111) surface at (a) pH 10, (b) pH 11, (c) pH 12 and (d) pH 13 in Ar sat. environment at 25 mVs^{-1} .

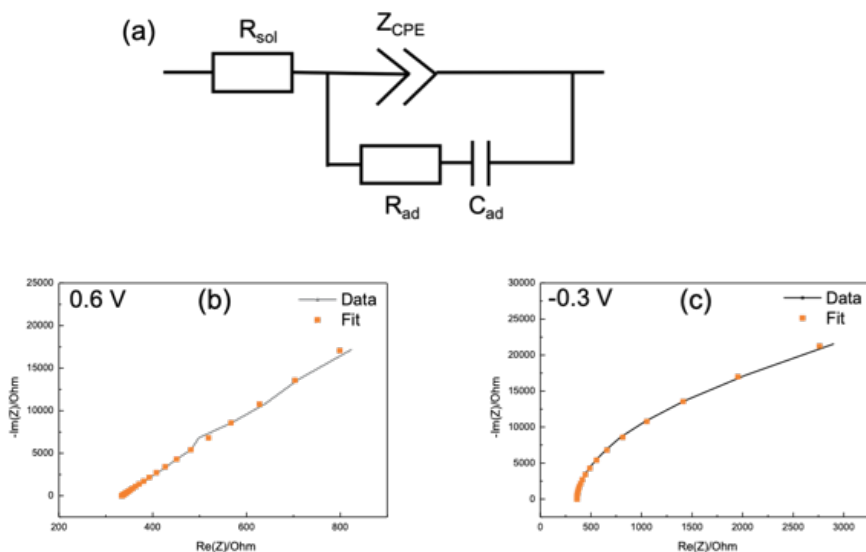


Figure S9 Typical EIS data plotted in the Nyquist impedance representation where the fits are obtained with the equivalent electric circuit (EEC) shown in (a) and the plots obtained at pH 10 in the (b) double layer region (0.6 V) and (c) near HER region (-0.3 V) are shown for comparison. In general, it was observed that in the double layer, where no Faradaic processes happen, R_{ad} and C_{ad} terms could be neglected as the main contribution in the overall capacitance came from the Z_{CPE} ($Z_{CPE} = C_{dl}^{-1}(j\omega)^{-n}$) term whereas near the onset of HER the constant phase (n) for Z_{CPE} became quite low (around 0.5), thereby losing any real physical meaning and the main contribution in the overall capacitance came from the C_{ad} term.

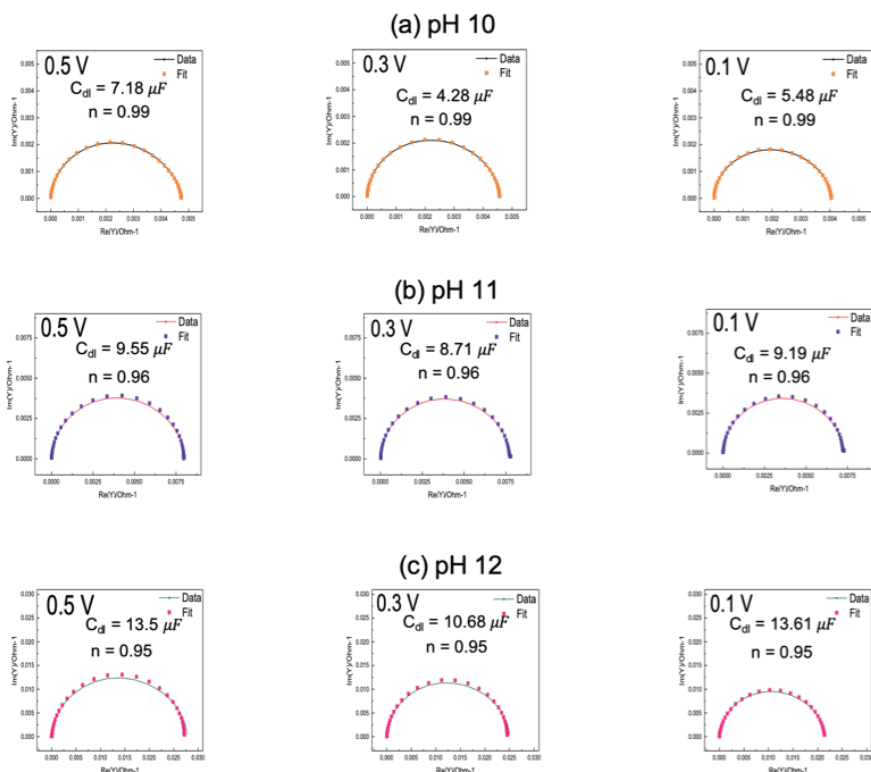


Figure S10 Typical Nyquist admittance plots and the fits obtained from the EIS data in the double layer region (0.5 V, 0.3 V and 0.1 V; left to right) at (a) pH 10, (b) pH 11 and (c) pH 12 where the EEC used to fit the data is the same as shown in Figure S10a. The value of the double layer capacitance (C_{dl}) and the CPE exponent term (n) as obtained from the Z_{CPE} ($Z_{CPE} = C_{dl}^{-1}(j\omega)^{-n}$); it is assumed that C_{dl} represents the true double layer capacitance (C_{dl}) in the limit of $n \geq 0.95$ term are indicated in the graph where it is observed that the value of C_{dl} increases from pH 10 to pH 12 and the value of n decreases from pH 10 to pH 12. At pH 13 (data not shown) the EEC showed a significant contribution from the C_{ad} term in the double layer such that the exponent term of the double layer capacitance became quite low ($n < 0.9$), thus making it difficult to derive any real physical meaning from the Z_{CPE} term in the double layer.

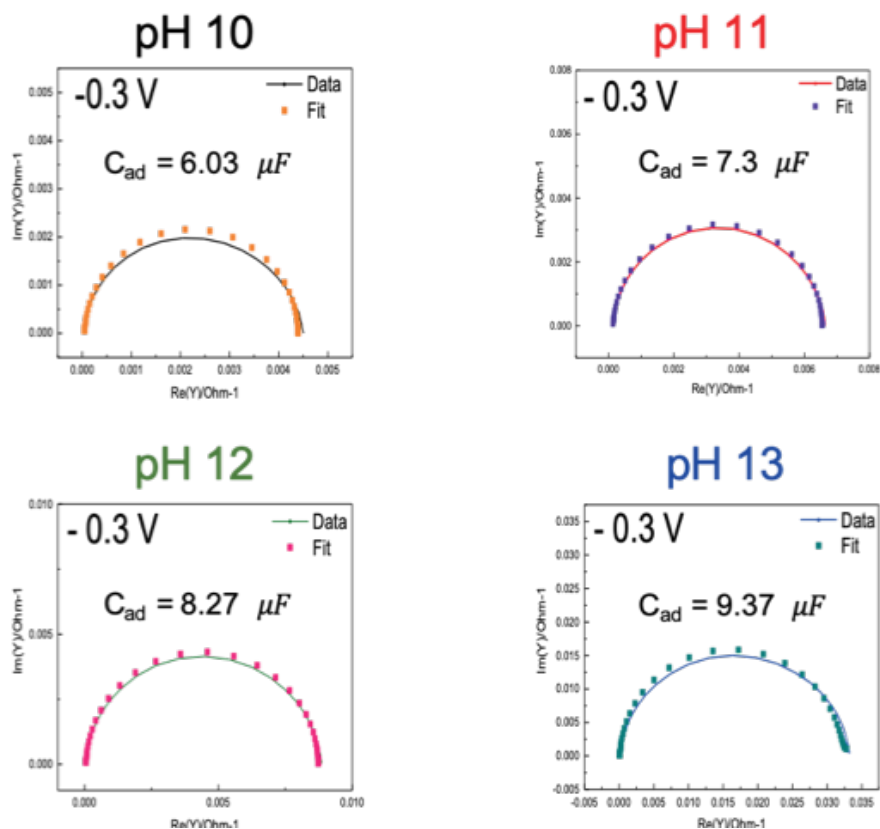


Figure S11 Typical Nyquist admittance plots and the fits obtained from the EIS data in the near HER region (-0.3 V) at pH 10, pH 11, pH 12 and pH 13 where the EEC used to fit the EIS data is same as Figure S11 (a). In the near HER region, the CPE term (Z_{CPE}) representing the double layer capacitance shows very low values for the exponent term (around 0.5) and hence cannot be used to derive any physical meaning. In this region contribution from the C_{ad} (adsorption capacitance) term becomes significant such that the value of C_{ad} increases from pH 10 to pH 13. The value for the C_{ad} obtained through the fits is indicated in the admittance plots.

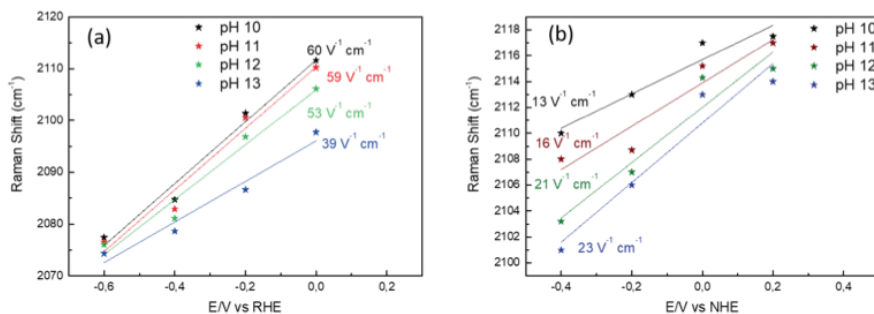


Figure S12 Stark tuning rates ($V^{-1} cm^{-1}$) obtained from the *in situ* Surface Raman spectra of hydrogen adsorption on roughened Au polycrystalline electrode on the (a) RHE scale and (b) NHE scale in 0.1 M NaOH (pH 13), 0.01 M NaOH + 0.09 M NaClO₄ (pH 12), 0.001 M NaOH + 0.099 M NaClO₄ (pH 11) and 0.0001 M NaOH + 0.0999 M NaClO₄ (pH 10), in *Ar* sat. environment.

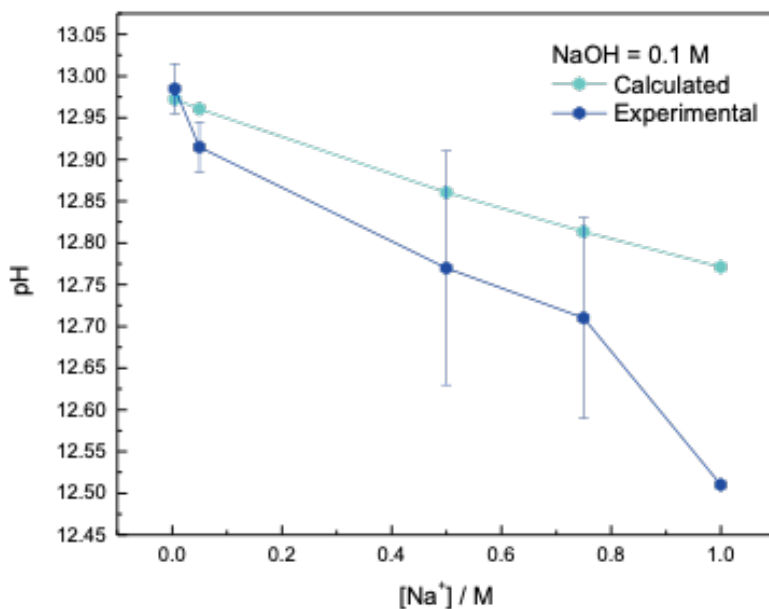


Figure S13 Experimentally measured (blue) and theoretically calculated (cyan) variation in the bulk pH in a 0.1 M NaOH electrolyte with the changing Na⁺ cation concentration in the electrolyte (5mM, 50 mM, 500 mM, 750 mM and 1000 mM). For calculating the bulk pH, $pK_{hydrolysis}$ of the Na⁺ cation was taken to be 14.2. The discrepancy between the experimentally observed pH and the theoretically calculated pH most likely arises from the changes in the local pH of the electrolyte which are not taken into account in the theoretical calculation of the pH.¹


References

- Singh, M. R.; Kwon, Y.; Lum, Y.; Ager, J. W.; Bell, A. T., Hydrolysis of Electrolyte Cations Enhances the Electrochemical Reduction of CO₂ over Ag and Cu. *Journal of the American Chemical Society* **2016**, *138* (39), 13006-13012.



Appendix C

Supporting Information to Chapter 4

The background of the page is a light gray gradient. It features several stylized molecular models scattered across the space. These models consist of small white and gray spheres connected by thin lines, representing atoms and bonds. In the lower right quadrant, there is a prominent white lightning bolt graphic that appears to be striking a cluster of larger, semi-transparent white spheres. The overall aesthetic is clean and scientific.

This is available as the Supporting Information to the article:
Goyal, A.; Koper, M. T. M., Understanding the role of mass transport in
tuning the hydrogen evolution kinetics on gold in alkaline media. *The Journal
of Chemical Physics* **2021**, *155* (13), 134705.

S1. Analytical model for the HER kinetics on Au electrodes

Here, we will present a simple model for the rate of hydrogen evolution reaction that can semi-quantitatively explain the experimental data presented in the main manuscript. The model is based on the idea that the rate of HER depends on the local (interfacial) concentration of cations, in the sense that the cations near the surface, essentially in the (outer-)Helmholtz plane, promote the hydrogen evolution.

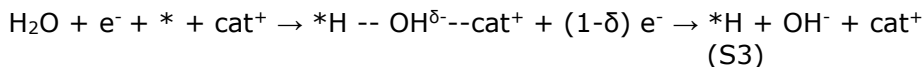
We assume that the rate of the water reduction reaction:



is determined by the first step, as suggested by the experimental Tafel slope:



where $*$ is a free site on the surface and $*\text{H}$ is a hydrogen atom adsorbed on that site. First, we will assume that all sites on the surface are equivalent and that there are no lateral interactions between the adsorbed hydrogens (Langmuir model). We will also assume that the rate of this reaction depends on the local concentration of cations because the cation can favorably interact with the transition state of the reaction. In a formal equation, this promoting action of the cation can be written as:



The idea is that the cation interacts favorably with the transition state because a (partially) negatively hydroxide is being split off from the reacting water molecule. This model is very similar to a model suggested recently by our group in which the hydroxide is (transiently) stabilized by an oxophillic adatom on the platinum electrode.¹ The key assumptions of the suggested rate equation are that it depends only on the concentration of cations near the surface, not directly on the electrolyte pH, and that this dependence follows a power law:

$$v_1 = k_1^{eff0} \exp\left(-\frac{\alpha FE}{RT}\right) [\text{Cat}^+]_s^\gamma \quad (\text{S4})$$

where, k_1^{eff0} is the standard rate constant, α is the transfer coefficient ($\alpha = 0.5$), F is Faraday's constant (96485 C mol^{-1}), E is the applied potential with respect to the standard potential of the reaction, R is the universal gas constant ($8.314 \text{ J K}^{-1} \text{ mol}^{-1}$), T is the temperature (K), $[\text{Cat}^+]_s$ is the surface concentration of cations (in mol cm^{-3}) and γ is the (empirical) reaction order in the cation concentration.

Moreover, under the steady-state conditions, the OH^- generation rate (i.e. HER rate) must be equal to its diffusion rate:

$$k_1^{eff0} \exp\left(-\frac{\alpha FE}{RT}\right) [Cat^+]_s^\gamma = \frac{D_{OH^-}}{\delta_{OH^-}} ([OH^-]_s - [OH^-]_b) \quad (S5)$$

where δ_{OH^-} is the diffusion layer thickness ($\delta_{OH^-} = 1.61 \times D_{OH^-}^{\frac{1}{3}} \times \nu^{\frac{1}{6}} \times \omega^{-\frac{1}{2}}$), D_{OH^-} is the diffusion coefficient of OH^- (5.273×10^{-5} cm²/s), ν is the kinematic viscosity of water (8.9×10^{-3} cm²/s) and ω is the angular frequency of rotation (in rad/s), $[OH^-]_s$ is the surface concentration of hydroxyl ions (in mol cm⁻³) and $[OH^-]_b$ is the bulk concentration of hydroxyl ions (in mol cm⁻³).

The conservation of electro-neutrality within the diffusion layer (which is a reasonable assumption except for the double-layer region very close to the surface ≤ 10 Å) requires that:

$$[OH^-]_s + [ClO_4^-]_s = [Cat^+]_s \quad (S6)$$

Therefore, the increase in the concentration of OH^- at the surface must be accompanied by a corresponding increase in the concentration of cations, which we assume to be linear, i.e.

$$[Cat^+]_s = [Cat^+]_b + \beta([OH^-]_s - [OH^-]_b) \quad (S7)$$

where β is a kind of local transference number:

$$\beta = \frac{u_{Cat^+}[Cat^+]_b}{u_{Cat^+}[Cat^+]_b + u_{ClO_4^-}[ClO_4^-]_b} = \frac{D_{Cat^+}[Cat^+]_b}{D_{Cat^+}[Cat^+]_b + D_{ClO_4^-}[ClO_4^-]_b} \quad (S8)$$

(where $u = \frac{|z|FD}{RT}$ as derived from Nernst – Einstein relationship)

Hence, eqn. S5 can be re-written by substituting the expression for $[Cat^+]_s$ from eqn. S7 as follows:

$$k_1^{eff0} \exp\left(-\frac{\alpha FE}{RT}\right) ([Cat^+]_b + \beta([OH^-]_s - [OH^-]_b))^\gamma = \frac{D_{OH^-}}{\delta_{OH^-}} ([OH^-]_s - [OH^-]_b) \quad (S9)$$

There is no general analytical solution for this equation, but we can use a first-order Taylor expansion to re-write the term $([Cat^+]_b + \beta([OH^-]_s - [OH^-]_b))^\gamma$ as follows:

$$([Cat^+]_b + \beta([OH^-]_s - [OH^-]_b))^\gamma \approx [Cat^+]_b^{\gamma-1} ([Cat^+]_b + \gamma\beta([OH^-]_s - [OH^-]_b)) \quad (S10)$$

where we have assumed that $[Cat^+]_b \gg \beta([OH^-]_s - [OH^-]_b)$. Then by using eqn. S10 we can solve eqn. S9 for $[OH^-]_s$ as follows:

$$[OH^-]_s = [OH^-]_b + \frac{k_1^{eff0} \exp\left(-\frac{\alpha FE}{RT}\right) [Cat^+]_b^\gamma}{\left(\frac{D_{OH^-}}{\delta_{OH^-}} - \gamma\beta k_1^{eff0} \exp\left(-\frac{\alpha FE}{RT}\right) ([Cat^+]_b)^{\gamma-1}\right)} \quad (S11)$$

As a result, the final current for HER can be calculated as follows:

$$i_{HER} = -2Fk_1^{eff0} \exp\left(-\frac{\alpha FE}{RT}\right) \left([Cat^+]_b + \beta \left(\frac{k_1^{eff0} \exp\left(-\frac{\alpha FE}{RT}\right) [Cat^+]_b^\gamma}{\left(\frac{D_{OH^-}}{\delta_{OH^-}} - \gamma \beta k_1^{eff0} \exp\left(-\frac{\alpha FE}{RT}\right) [Cat^+]_b^{\gamma-1}\right)} \right) \right)^\gamma \quad (S12)$$

Here, the eqns. have been written by assuming that the central parameter that affects the kinetics of HER on Au electrodes is only the near surface cation concentration ($[Cat^+]_s$) and the rotation dependence of HER kinetics is a byproduct of the associated changes in the near-surface cation concentration with the changing surface pH. In the simulations we take the standard rate constant for the reaction, i.e. k_1^{eff0} to be 10^{-9} cms^{-1} , since Au is a bad catalyst for HER.² However, we note, that the values of the intrinsic rate constant can depend on the identity of the cation in the electrolyte, but for the sake of simplicity we neglect these effects in our simulations. Moreover, we take γ to be 0.5 in the simulations since the model is meant to represent the promotional regime of cations for HER and based on our experimental results (Figure 3) we expect the reaction order in cation concentration to be a positive fractional value. Additionally, based on the theoretically calculated values of β for the different alkali metal cations (Table S1) we take β to be 0.5 in the simulations.

S2. Supplementary figures

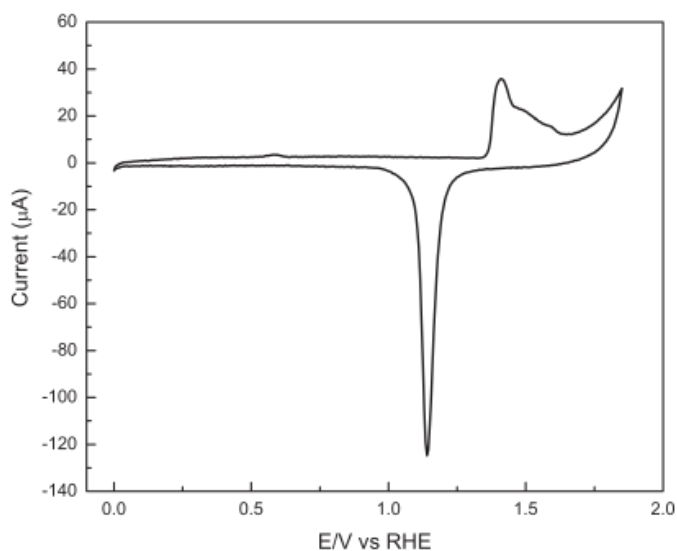


Figure S1 Characteristic cyclic voltammogram for Au polycrystalline surface (black) obtained in 0.1 M H_2SO_4 in Ar sat. environment at 50 mVs^{-1} where the electrochemically active surface area (ECSA) was calculated by integrating the area of the Au_xO_y reduction peak in the scan.

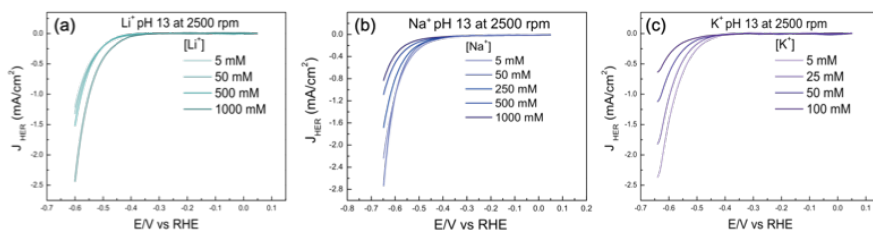


Figure S2 Experimentally obtained negative going scan of the cyclic voltammogram at polycrystalline Au electrodes at pH 13 and 2500 rpm for (a) Li^+ , (b) Na^+ and (c) K^+ at different bulk cation concentrations. The experimentally obtained reaction orders from these measurements are shown in Fig. 3d, e and f in the main manuscript.

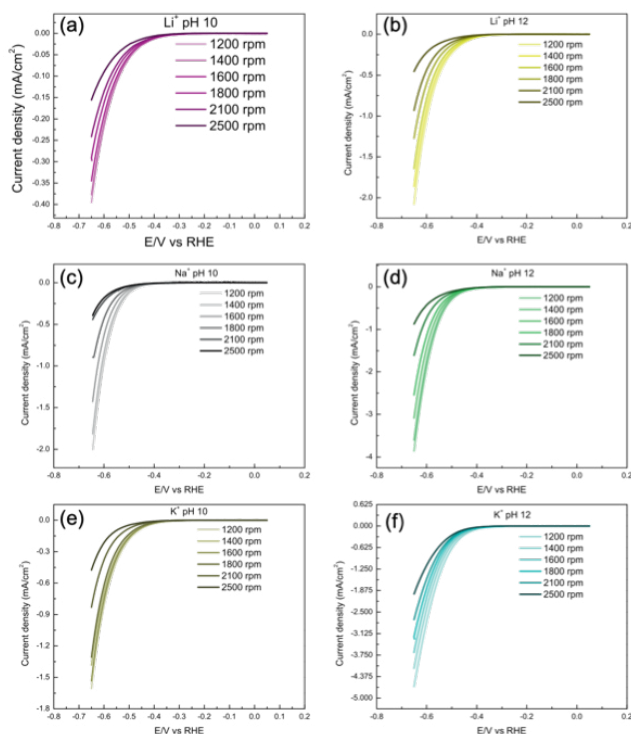


Figure S3 Negative going scan of the cyclic voltammograms obtained for HER on Au polycrystalline surface in Li^+ ion containing electrolytes at (a) pH 10 and (b) pH 12, in Na^+ ion containing electrolytes at (c) pH 10 and (d) pH 12, and in K^+ ion containing electrolytes at (e) pH 10 and (f) pH 12 at a fixed cation concentration in the bulk (0.1 M) at different rotation rates (2500 rpm, 2100 rpm, 1800 rpm, 1600 rpm, 1400 rpm and 1200 rpm) at a scan rate of 25 mVs^{-1} .

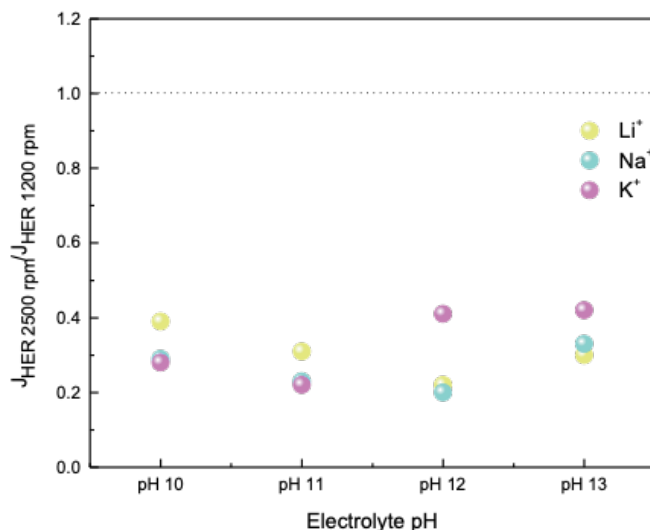


Figure S4 Ratio of the HER current density at 2500 rpm/ 1200 rpm at -0.65 V (vs RHE) as a function of the electrolyte pH for Li⁺, Na⁺ and K⁺ ion containing electrolytes. A ratio lower than one indicates that the HER current density is higher at 1200 rpm than 2500 rpm. Lower values of the ratio indicate that the difference between the current density at 1200 rpm and 2500 rpm is larger.

Table S4 The local transference number (β) as derived from eqn. S8.

Cation	$\beta = \frac{D_{\text{Cat}^+}[\text{Cat}^+]_b}{D_{\text{Cat}^+}[\text{Cat}^+]_b + D_{\text{ClO}_4^-}[\text{ClO}_4^-]_b}$
Li ⁺	0.37
Na ⁺	0.45
K ⁺	0.52


References

1. McCrum, I. T.; Koper, M. T. M., The role of adsorbed hydroxide in hydrogen evolution reaction kinetics on modified platinum. *Nature Energy* **2020**, *5* (11), 891-899.
2. Bard, A. J.; Faulkner, L. R., *Electrochemical methods : fundamentals and applications* Wiley: New York, **1980**.



Appendix D

Supporting Information to Chapter 5

The background of the page is a light gray gradient. It features several molecular models scattered across the space, including water molecules (H2O) and carbon dioxide molecules (CO2). On the right side, there is a large, stylized lightning bolt graphic that appears to be striking a cluster of large, overlapping spheres, possibly representing a catalyst or a porous material. The overall aesthetic is scientific and modern.

This is based on the Supporting Information for the submitted manuscript:
Goyal, A.; Bondü, C. J.; Graf, M.; Koper, M. T. M., Effect of pore diameter
and length on electrochemical CO₂ reduction reaction at nanoporous gold
catalysts. *Chemical Science* (Submitted)

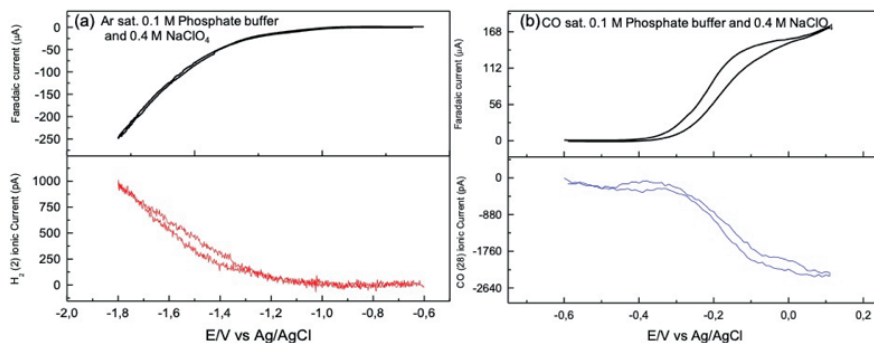


Figure S2 DEMS calibration experiment for (a) H_2 and (b) CO , performed in 0.1 phosphate buffer and 0.4 M $NaClO_4$ at 5 mVs^{-1} and a flow rate of $300\ \mu\text{Lmin}^{-1}$ in Ar sat. and CO sat. conditions respectively. For determining $K_{H_2}^{z=2}$ the Faradaic current for HER and the ionic current at m/z 2 as shown in S1a in the top panel and the bottom panel, respectively, were plugged into eqn. 3 (see Section 2.4 in the Main Manuscript) where z was taken to be 2. For determining $K_{CO}^{z=2}$ the Faradaic current for CO oxidation and the ionic current at m/z 28 as shown in S1b in the top panel and the bottom panel, respectively, were plugged into eqn. 3 (see Section 2.4 in the Main Manuscript) where z was taken to be 2.

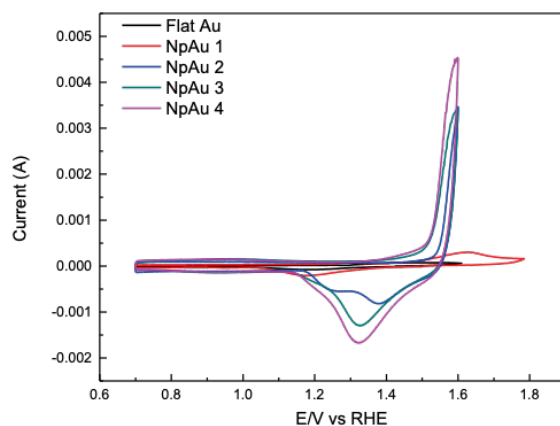


Figure S3 Characterization cyclic voltammograms for different Au catalysts in 0.1 M H_2SO_4 in Ar sat. environment at 50 mVs^{-1} where the charge of the Au_xO_y reduction peak was used to calculate the electrochemically active surface area (ECSA) of the different samples

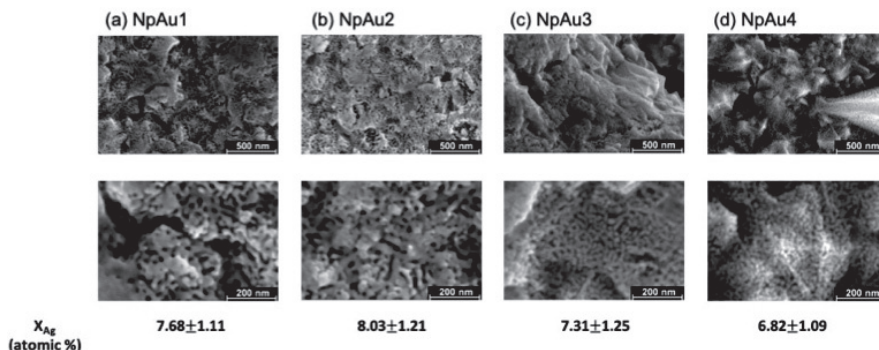


Figure S4 SEM characterization of different nano-porous Au (NpAu) samples, left to right: (a) NpAu1, (b) NpAu2, (c) NpAu3 and (d) NpAu4 where the upper row shows the low magnification SEM images and the lower row shows the high magnification SEM images for the different samples. At the bottom, the residual Ag content (X_{Ag}) as determined by the EDX measurements at low magnification is given for every NpAu sample along with the internal quantification error.

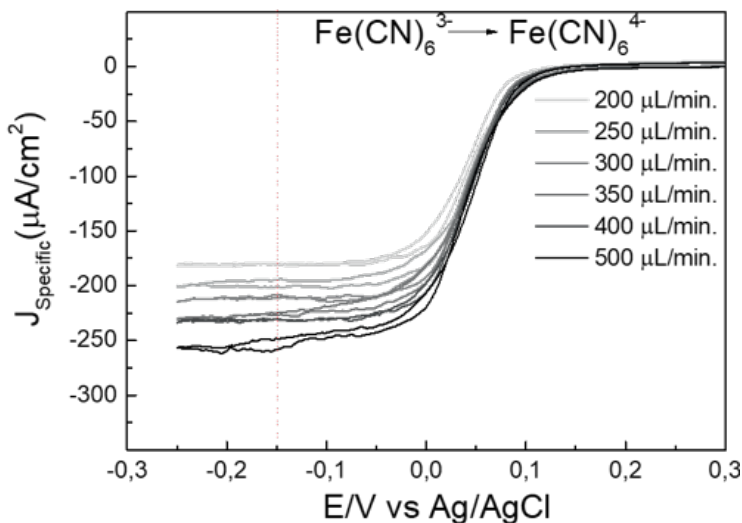


Figure S5 Determination of the diffusion layer thickness in the dual thin layer cell: cyclic voltammograms obtained in 0.1 M $NaHCO_3$ and 0.4 M $NaClO_4$ with 10 mM $K_3Fe(CN)_6$ at a scan rate of $5 mVs^{-1}$, at different flow rates, where the diffusion limited currents for ferricyanide reduction at $-0.15 V$ vs Ag/AgCl (indicated by the dotted line) were used to calculate the diffusion layer thickness by using Fick's law.

Table S1 Diffusion layer thickness (middle column) at different flow rates as calculated from the data shown in Figure S4 by using Fick's first law of diffusion, where no. of electrons involved were taken to be 1, concentration of $K_3Fe(CN)_6$ was taken to be 10 mM, diffusion coefficient of $Fe(CN)_6^{3-}$ was taken to be $7 \times 10^{-6} \text{ cm}^2\text{s}^{-1}$ and Faraday's constant was taken to be 96485 Cmol^{-1} . Thereafter, the theoretical diffusion limited current for CO₂RR under the condition of our studies was calculated (right most column) by again using Fick's law where no. of electrons involved in the reaction were taken to be 2 and the concentration of CO_2 (aq.) was taken to be 16.5 mM (0.5 atm. CO_2) and the values for the diffusion layer thickness were taken from the middle column of the table.

Flow rate ($\mu\text{L}/\text{min}$)	Diffusion layer thickness (μm)	$J_{\text{Limiting (theoretical)}}$ (mA/cm^2) at 0.5 atm. CO_2
200	374.80719	-1.40061
250	336.0546	-1.56213
300	323.70757	-1.62171
350	297.23011	-1.76617
400	293.23413	-1.79024
500	261.41034	-2.00818

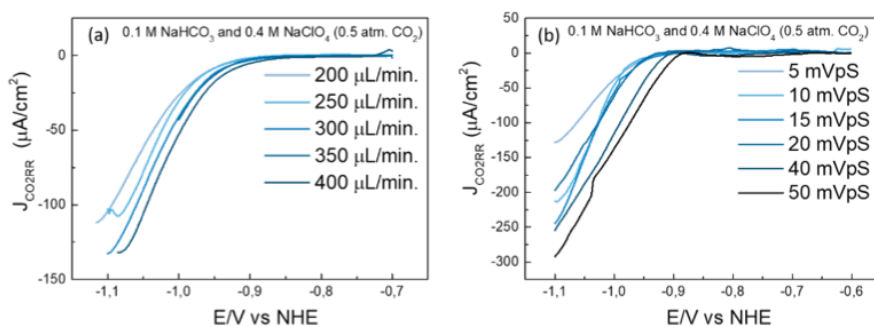


Figure S6 Partial current density for CO formation on Flat Au as obtained from the ionic current at m/z 28 by using eqn. 3 (in the main manuscript) with 0.5 atm. of CO_2 in 0.1 M NaHCO_3 and 0.4 M NaClO_4 containing electrolyte at (a) different flow rates and (b) different scan rates

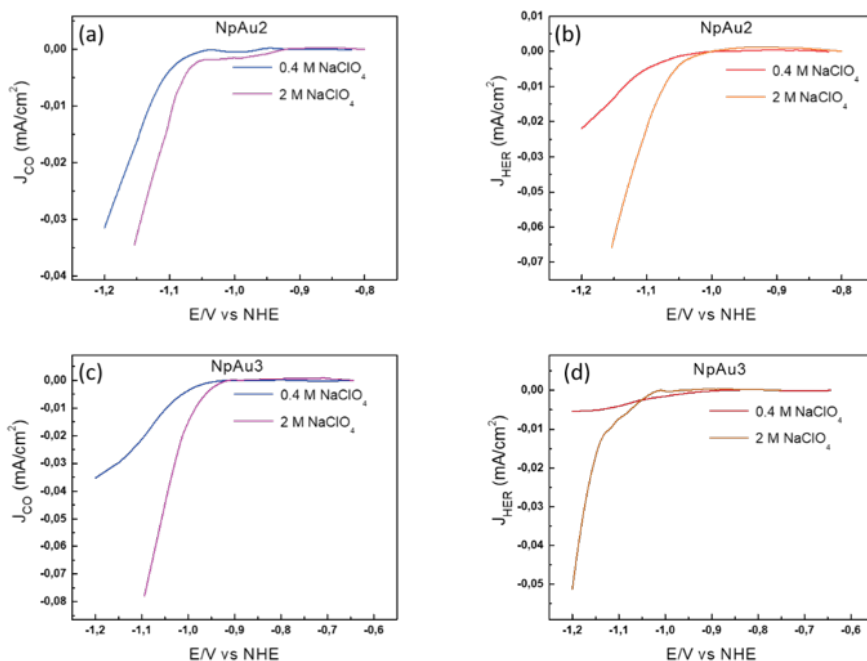


Figure S7 Partial specific current density for CO formation as obtained from the ionic current at m/z 28 by using eqn. 3 (Main Manuscript) with 0.5 atm. CO₂ in 0.1 M NaHCO₃ and 0.4 M NaClO₄ containing electrolyte (blue) and in 0.1 M NaHCO₃ and 2 M NaClO₄ containing electrolyte (purple) at a scan rate of 5 mVs⁻¹ and a flow rate of 300 μ Lmin⁻¹ on (a) NpAu2 and (c) NpAu3 and Partial current density for HER as obtained from the ionic current at m/z 2 by using eqn. 3 (Main Manuscript) with 0.5 atm. CO₂ in 0.1 M NaHCO₃ and 0.4 M NaClO₄ containing electrolyte (red) and in 0.1 M NaHCO₃ and 2 M NaClO₄ containing electrolyte (orange) at a scan rate of 5 mVs⁻¹ and a flow rate of 300 μ Lmin⁻¹ on (b) NpAu2 and (d) NpAu 3.

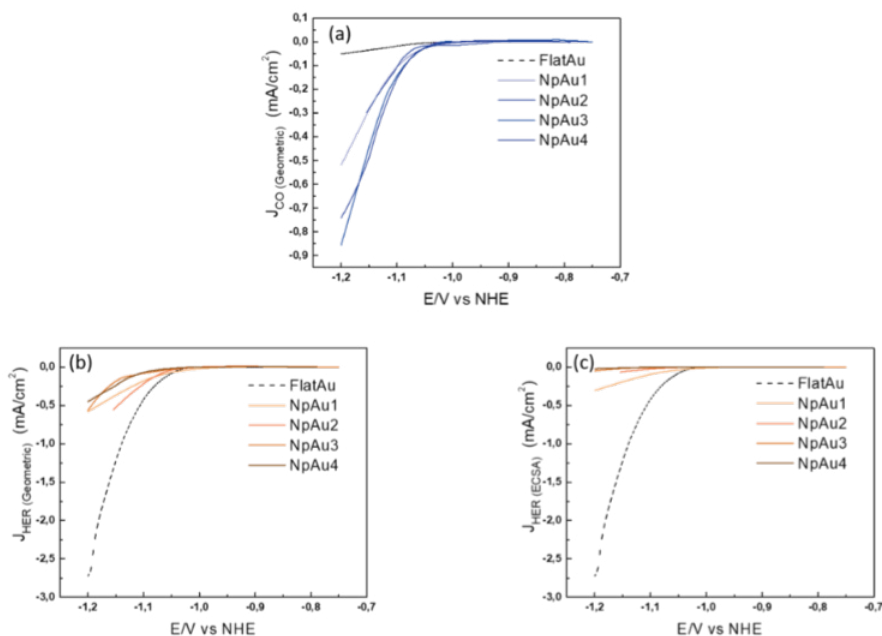


Figure S8 (a) Partial geometric current density for CO formation on different Au catalysts as obtained from the ionic current at m/z 28 by using eqn. 3 (Main Manuscript) with 0.5 atm. CO₂ in 0.1 M NaHCO₃ and 2 M NaClO₄ containing electrolyte at a scan rate of 5 mVs⁻¹ and a flow rate of 300 μLmin⁻¹. (b) Partial geometric current density for HER and (c) Partial specific current density for HER, as obtained from the ionic current at m/z 2 by using eqn. 3 (Main Manuscript) with 0.5 atm. CO₂ in 0.1 M NaHCO₃ and 2 M NaClO₄ containing electrolyte at a scan rate of 5 mVs⁻¹ and a flow rate of 300 μLmin⁻¹.

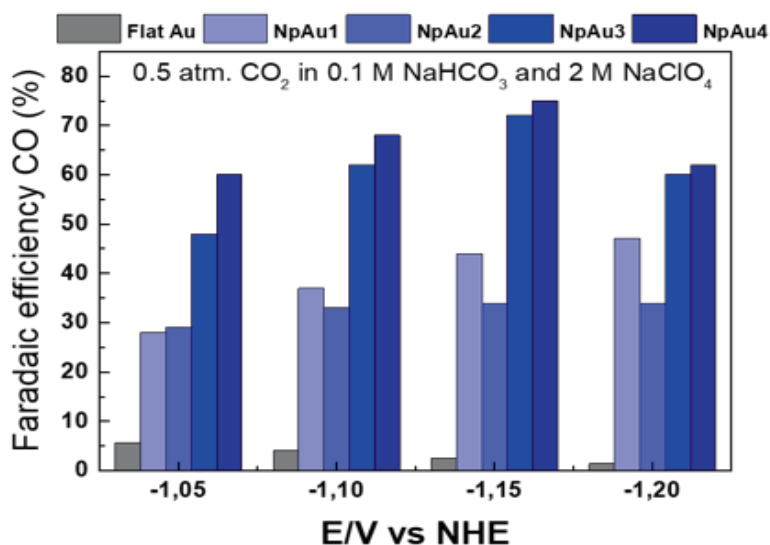


Figure S9 Faradaic efficiency for CO formation of the different Au catalysts in 0.5 atm. CO₂ and 0.1 M NaHCO₃, 2 M NaClO₄ containing electrolyte at different potentials (vs. NHE) as obtained from the DEMS measurements by using eqn. 4 (Main Manuscript).



Summary

This thesis has shed light on some of the ways in which the local electrolyte composition can differ from the bulk and how these changes in the local reaction environment can determine the activity and/or selectivity of two electrocatalytic reactions, namely, electrochemical CO₂ reduction reaction (CO₂RR) and hydrogen evolution reaction (HER).

In **chapter 2** of this thesis we adapted the well-known rotating ring disk electrode (RRDE) technique to study the role of mass transport in tuning the competition between CO₂RR and HER on Au catalysts. The idea was to systematically tune the local concentration gradients at the catalyst surface by the means of hydrodynamic convection control and to quantify the formed amounts of CO and H₂ during the reactions in an online fashion. This was important to avoid any convolutions due to time-based concentration polarization effects. We found that the rate of CO₂RR increased slightly with the increasing rotation rate (i.e. mass transport) of the electrode. We attributed this enhancement to the suppression of local consumption of CO₂ via its homogeneous acid-base equilibria. Interestingly, in contrast with CO₂RR, the increasing rotation rate of the electrode led to the suppression of the competing HER reaction (in 0.1 M bicarbonate containing electrolytes). We showed that this suppression stems from the pH dependence of HER, since on Au catalysts, the HER activity increases with increasing pH of the electrolyte. Thus, with increasing rotation rate of the electrode, as the locally generated hydroxyl ions are transported away from the electrode surface, and the HER activity decreases. As a result, the Faradaic selectivity for CO₂RR enhances significantly with increasing rotation rate of the electrode, in part due to the slight enhancement of CO formation rate but mostly due to the suppression of competing HER reaction.

In **chapter 3** we further investigated the pH dependence of HER in alkaline media on Au catalysts. We found that the pH dependence of HER is in-fact inter-linked with the cation concentration dependence of this reaction. We showed that the cations near the surface enhance the rate of HER by stabilizing the transition state for the rate determining Volmer step (water dissociation step) of this reaction. Interestingly, since the changing electrolyte pH leads to changes in the interfacial electric field, this in-turn results in changing near-surface cation concentration. In particular, with increasing electrolyte pH, the interfacial electric field becomes more negative and this results in a corresponding increase in the local concentration of cations. Hence, the enhancement in HER activity with increasing electrolyte pH is in-fact due to the increase in the near-surface cation concentration. Moreover, we showed that if we keep increasing the near-surface cation concentration, either by increasing the bulk cation concentration or by increasing the electrolyte pH, at some point the promotional effect of cations on HER saturates and even becomes inhibitive. This shows that beyond a threshold concentration, the cations near the surface can lead to blocking of the active sites for HER, either due to direct adsorption at the catalyst surface or due to the crowding of the double layer.

In **Chapter 4** of this thesis, we reconciled the findings of Chapter 2 and Chapter 3 by further investigating the rotation rate dependence as well as the cation identity dependence of HER on Au electrodes. We pointed out in this work that though the bulk pH and the local pH affect the HER activity by tuning the near-surface cation concentration, they do it in two distinct ways. In the case of bulk pH changes, near-surface cation concentration responds to the changes in the interfacial electric field strength (as described in Chapter 3). However, local pH changes (via rotation rate control) tune the local cation concentration, simply because of the need to satisfy local electroneutrality. Moreover, we also show in this work that depending on the hydration energy of cations, the strength of the cation-metal interactions can be tuned, which can also result in varying HER activity trends.

Lastly, in **Chapter 5** we implemented the understanding gained in the previous chapters to study the role of pore parameters (diameter and length) in tuning the local reaction environment and hence the activity/selectivity of CO₂RR and HER on nanoporous Au catalysts. To do so, we employed our home-built differential electrochemical mass spectrometry (DEMS) technique which allows for the online, quantitative detection of CO and H₂ over the course of CO₂RR and HER. We found that similar to the flat Au catalysts (Chapter 2), the changes in the local concentration gradients in nanoporous catalysts mainly affect the HER activity. Notably, we could show that due to the presence of additional ohmic drop effects in the nanoporous channels, the entirety of the nanoporous catalysts do not actually participate in electrocatalysis and these ohmic drop effects scale with the length of the pores.

Samenvatting

In dit proefschrift onderzoeken we hoe de lokale samenstelling van een elektrolyt kan verschillen van de gemiddelde samenstelling, en hoe verschillen in de lokale reactieomgeving de activiteit en/of selectiviteit van twee elektrokatalytische reacties, te weten de elektrochemische koolstofdioxide reductie reactie (CO₂RR) en de waterstofevolutie reactie (HER), kunnen sturen.

In **hoofdstuk 2** van dit proefschrift hebben we gebruik gemaakt van de draaiende ring-schrijf elektrode (RRDE) methodiek om de rol van massatransport in de competitie tussen de CO₂RR en HER te bestuderen op goud katalysatoren. De achterliggende gedachte was om systematisch verschillende lokale gradiënten in de buurt van het katalysatoroppervlak aan te leggen door de hydrodynamische convectie te reguleren, en de gevormde hoeveelheden CO en H₂ te kwantificeren tijdens de reactie. We hebben voor deze uitvoering gekozen om mogelijke problemen gerelateerd aan de opbouw van tijdsafhankelijke spanningsgedreven concentratiegradiënten te verhelpen. We zagen dat de snelheid van de CO₂RR iets omhoog ging wanneer we de hoeksnelheid (en daarmee het massatransport) van de elektrode verhoogden. Deze verhoging in snelheid schreven we toe aan het onderdrukken van de lokale verbruik aan CO₂ via het zuur-base evenwicht. In tegenstelling tot de CO₂RR, zagen we dat het verhogen van de hoeksnelheid juist leidde tot afname van de snelheid van de concurrerende HER (in 0.1 M bicarbonaat-bevattende elektrolyten). We toonden aan dat deze onderdrukking het resultaat is van de pH afhankelijkheid van de HER, aangezien bij goud katalysatoren de activiteit voor de HER omhoog gaat als de pH verhoogd wordt. Daarom gaat de activiteit voor de HER omlaag als de hoeksnelheid omhoog gaat, aangezien dit leidt tot een toename in de snelheid waarmee hydroxylionen zich verder weg van het oppervlak verplaatsen. Het resultaat is dat de Faraday efficiëntie voor de CO₂RR significant omhoog gaat als de hoeksnelheid van de elektrode verhoogd wordt, deels vanwege een toename in de vormingssnelheid van CO, maar voornamelijk door de onderdrukking van de HER.

In **hoofdstuk 3** voerden we diepgaander onderzoek uit naar de pH afhankelijkheid van de waterstofevolutie reactie aan goud katalysatoren. We ontdekten dat de pH afhankelijkheid en de kation afhankelijkheid van de HER aan elkaar gerelateerd zijn, en toonden aan dat de kationen in de buurt van het oppervlak de reactiesnelheid van de HER verhogen door de overgangstoestand voor de snelheidsbepalende Volmer-stap (de dissociatie van water) te stabiliseren. Echter, ze zijn ook nog op een andere manier met elkaar verbonden. Namelijk, veranderingen in de pH hebben als gevolg dat de potentiaal aan het grensvlak verandert, en deze verandering in potentiaal beïnvloedt op zijn beurt de kation-concentratie nabij het oppervlak. Specifiek, als de pH wordt verhoogd dan resulteert dit in een negatievere potentiaal aan het grensvlak, wat dan weer leidt tot een verhoging van de kation concentratie in de buurt van het oppervlak. Daarom is de pH afhankelijkheid van de reactiesnelheid van de HER uiteindelijk een gevolg van veranderingen in de lokale kation concentratie dichtbij het

oppervlak. Verder laten we zien dat als we deze lokale concentratie aan kationen blijven verhogen, door meer zout op te lossen in het elektrolyt óf door de pH te verhogen, dat het positieve effect dat het verhogen van de kation-concentratie heeft op de op de reactiesnelheid van de HER verdwijnt, of zelfs een negatief effect wordt. Dit resultaat toont aan dat, na een bepaald punt, hoge lokale kation concentraties kunnen leiden tot vermindering van de activiteit van de katalysator. Dit effect van het resultaat zijn van adsorptie van kationen aan het katalysatoroppervlak, of door de overmaat aan ionen in de buurt van het oppervlak die elkaar in de weg zitten.

In **hoofdstuk 4** verzoenen we de kennis die we hebben opgedaan in hoofdstukken 2 en 3, door de rotatiesnelheidsafhankelijkheid en kation-identiteitsafhankelijkheid van de HER aan goud elektrodes in meer detail te onderzoeken. Hierin laten we zien dat, alhoewel zowel de gemiddelde elektrolyt pH en de lokale pH de reactiesnelheid van de HER beïnvloeden door de oppervlakconcentratie aan kationen te veranderen, ze dit op verschillende manieren faciliteren. In het geval van veranderingen in de gemiddelde elektrolyt pH zijn veranderingen in de oppervlakconcentratie van kationen het gevolg van veranderingen in de grensoppervlaktespanning, zoals besproken in hoofdstuk 3. Echter, in het geval van de lokale pH (welke we controlleren door de rotatiesnelheid aan te passen), zijn veranderingen in de lokale kation-concentratie gedreven door het naleven van het elektroneutraliteitsprincipe in de directe omgeving. Verder tonen we aan dat de mate van interactie tussen de kationen en het metaaloppervlak afhankelijk is van de hydratatie energie van het kation, wat leidt tot verschillen in welke mate de HER beïnvloed wordt door verschillende kationen.

Uiteindelijk hebben we in **hoofdstuk 5** alle ervaringen die we hebben opgedaan in de vorige hoofdstukken gebruikt om de rol van verschillende parameters van poriën in het katalysatoroppervlak (specifiek, hun diameter en lengte) in het reguleren van de lokale reactieomgeving te bepalen voor goud katalysatoren, waar deze lokale omstandigheden op hun beurt de activiteit en selectiviteit van de CO₂RR en HER beïnvloeden. Om dit onderzoek te kunnen verrichten, hebben we gebruik gemaakt van een differentieel-gepompte electrochemische massaspectrometrie (DEMS) opstelling waarmee we online de hoeveelheden gevormde CO en H₂ konden kwantificeren tijdens de CO₂RR en de HER. In overeenstemming met de platte (goud) katalysatoroppervlakken gebruikt in hoofdstuk 2, vonden we dat veranderingen in de lokale concentratiegradieënten voornamelijk de HER beïnvloeden voor een nanoporeuze katalysator. Een verdere belangrijke ontdekking is dat door de aanwezigheid van additionele weerstand in de poriën, deze poriën niet deelnemen in het katalyseren van de reactie; waarbij deze weerstand-gerelateerde inhibitie schaal met de lengte van de poriën.

List of Publications

Chapter 2

Goyal, A.; Marcandalli, G.; Mints, V. A.; Koper, M. T. M., Competition between CO₂ Reduction and Hydrogen Evolution on a Gold Electrode under Well-Defined Mass Transport Conditions. *Journal of the American Chemical Society* **2020**, *142* (9), 4154-4161

Chapter 3

Goyal, A.; Koper, M. T. M., The Interrelated Effect of Cations and Electrolyte pH on the Hydrogen Evolution Reaction on Gold Electrodes in Alkaline Media. *Angewandte Chemie International Edition* **2021**, *60* (24), 13452-13462

Chapter 4

Goyal, A.; Koper, M. T. M., Understanding the role of mass transport in tuning the hydrogen evolution kinetics on gold in alkaline media. *The Journal of Chemical Physics* **2021**, *155* (13), 134705.

Chapter 5

Goyal, A.; Bondü, C. J.; Graf, M.; Koper, M. T. M., Effect of pore diameter and length on electrochemical CO₂ reduction reaction at nanoporous gold catalysts. *Chemical Science* (Submitted)

Other Publications

Marcandalli, G.; Goyal, A.; Koper, M. T. M., Electrolyte Effects on the Faradaic Efficiency of CO₂ Reduction to CO on a Gold Electrode. *ACS Catalysis* **2021**, *11* (9), 4936-4945.

Bondue, C. J.; Graf, M.; Goyal, A.; Koper, M. T. M., Suppression of Hydrogen Evolution in Acidic Electrolytes by Electrochemical CO₂ Reduction. *Journal of the American Chemical Society* **2021**, *143* (1), 279-285.

Monteiro, M. C. O.; Goyal, A.; Moerland, P.; Koper, M. T. M., Understanding Cation Trends for Hydrogen Evolution on Platinum and Gold Electrodes in Alkaline Media. *ACS Catalysis* **2021**, *11* (23), 14328-14335.

Acknowledgements

These past four years have been a time of tremendous growth and fulfilment for me. I have learned so much, from so many people and in so many different ways. Here, I would like to express my gratitude to them and if I miss some of you, please forgive the imperfections of my memory.

First and foremost, I want to thank my supervisor, **Prof. Dr. Marc Koper**. I started working at CASC with no prior experience in electrocatalysis and I am sure that in our first few interactions, I was fairly out of my depth. So, I want to thank you Marc, for your continued patience and kindness, they were very important in keeping me motivated, especially in the early days of my PhD. Often times, when I have reached my wit's end, a gentle nudge from you (during our meetings) has always steered me in the right direction. It is also not lost on me that I have had many privileges in the last four years, be it the access to world-class research facilities or the option of attending various international conferences and summer schools. So, I want to sincerely thank you, for making all this possible.

Then I would like to thank **José** for being so nice and helpful, not only to me, but to all the new incoming students in the group. CASC will not be the same without you José! I also want to take this opportunity to thank the glass blowers and the FMD department at Leiden university, especially **Thijs Hoogenboom**, for fixing bits and bobs and saving the day many a times, by being so quick and accessible. I also want to thank **Wen Tian** for all the times he answered my queries regarding the ordering system and for all the interesting discussions we had over the years, about science (and its applications) and politics.

I would also like to take this opportunity to thank all the **CASC group members**, present and past, for sharing their wisdom with me when I needed help and for sharing a laugh with me when I needed cheering up! Science can be a harsh place at times and it's in these moments that one comes to appreciate the value of nice colleagues. Thank you all for being there and for all the coffee/lunch breaks, they were much appreciated and so was the company!

A special thanks to **Giulia Marcandalli**, **Ian Mccrum**, **Matthias Graf** and all my students. **Giulia**, you always had much more faith than me in the RRDE set-up, hehe, I sincerely thank you for that collaboration and for your friendship. **Ian**, I learned a lot about HER from you and chapter 3 and 4 owe a great deal to that. So, I want to thank you for that. **Matthias** in your brief stay here, you imparted so much wisdom to me about the preparation and the properties of nanoporous catalysts. Thanks for this brief yet fruitful collaboration. Also, I want to thank all my students, especially **Vlad** and **Pricilla**, for being so hard-working and diligent. I was very happy to be your supervisor.

A special shout out to **Stefan**, for being a constant source of joy, both inside and outside the lab! And to my friend **Shafali** in India. Our long-distance calls have played a huge role in keeping me sane, so, thank you for that and for a lifetime of happy memories.

And where do I begin to thank you **Christoph**! This thesis and my mental state at the end of this PhD would have looked much different, if not for you. I have learned so much from you, sometimes, just by listening you talk so passionately about your own work, hehe. I also specifically want to thank you for all the help with the DEMS. I am so happy that we officially collaborated on something which is a part of my thesis. But more than anything else, I want to thank you for patiently listening to me, as I endlessly rambled on about work-related things. I know it was not always easy. For the last three years, you have been my mast through the storms of life. I hope I am likewise to you my love.

A last thanks goes out to my family in India. **Mumma, Papa** and **Ayush** you guys have made it all possible! **Mumma**, I am eternally grateful for all the hard work that you put into our studies, when we were children. The work ethic that you instilled in us back then is something that I still carry with me today. **Papa**, this PhD is the culmination of your unwavering faith in me. Against all odds you made it happen. Thank you. **Ayush**, you have always been the bright bulb of the family and my interest in all things academic can be traced back to my desire to outperform you, hehe. But after a lifetime of trying and failing, I want to thank you for your graciousness through it all and for being my big brother and best teacher.

Curriculum Vitae

Akansha Goyal was born on 9th of July 1994 in Delhi, India, where she lived for the first 20 years of her life. She did her schooling at Guru Harkishan Public School where she chose science as her direction of study upon entering the secondary phase of her education. She was awarded the excellence award during this time for getting the highest score in Chemistry and Physics in the All India Senior Secondary Examination.

After graduating from school, Akansha enrolled in B.Sc. Chemistry (hons.) programme at Delhi University which she graduated from in 2014. During this time, she also did an internship at the Indian Institute of Technology (IIT), in Gandhinagar, India, where she studied the photochemical properties of cholesterol conjugated diphenylpolyenes in the group of Dr. Sriram Kanvah Gundimeda.

After her Bachelor studies, Akansha moved to Leiden, Netherlands, to pursue an M.Sc. in Chemistry. During her masters, she was the recipient of Leiden University excellence scholarship (LExS) which covered the tuition fee (minus the statutory fee) of her studies. During this time, she did two different research internships. The first internship was carried out on the synthesis of lanthanoid doped upconverting nanoparticles in the group of Prof. Sylvestre Bonnet at Leiden University. The second internship was carried out on the synthesis of transition metal-oxide based cathode materials for Li ion batteries in the group of Prof. Serena Corr at Glasgow University. For the latter, she also received the Erasmus+ grant for traineeships from EU. It was during this time that her interest in electrochemistry and sustainable energy research was sparked. Upon returning from Glasgow, she did a brief literature survey on electrochemical CO₂ reduction reaction at nanostructured catalysts, under the supervision of Prof. Marc Koper at Leiden University.

This eventually turned into a longer association, both with electrochemistry and with the Koper group. As in 2017, Akansha started her Ph.D. at Leiden University under the supervision of Prof. Marc Koper. This project was supported by Advanced Research Center for Chemical Building Blocks (ARC CBBC) consortium, co-financed by the Netherlands Organization for Scientific Research (NWO) and Shell Global Solutions B.V. The main focus of her Ph.D. was to understand the role of local reaction environment in tuning the activity/selectivity of electrochemical CO₂ reduction reaction and H₂ evolution reaction.

This Ph.D. project led to many interesting results as well as publications, which are presented in this thesis. It also led to many fruitful collaborations, which enriched Akansha, both academically and personally.

During this time, Akansha assisted in teaching the B.Sc. practical courses at Leiden Institute of Chemistry, as well as in the research internships of various B.Sc. level students. She also presented her work at various international conferences, including oral presentations at 72nd Annual ISE meeting, 29th Topical ISE meeting and EcoCat international conference. During this time, she also had the opportunity of attending the SurfCat

summer school in Denmark and the Heraeus seminar conference in Germany.
Following the obtainment of her Ph.D., Akansha will continue her stay in the Koper lab as a post-doctoral researcher.